Development of Conducting Polymer Based Biomimetic Muscles and Fabrication Techniques for an Artificial Pectoral Fish Fin

by

S. Naomi Davidson

B.S. Mechanical Engineering (2002)
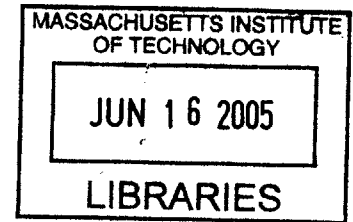
University of California at Berkeley

Submitted to the Department of Mechanical Engineering
in Partial Fulfillment of the Requirements for the Degree of
Master of Science in Mechanical Engineering

at the

Massachusetts Institute of Technology

May 2005

© 2005 Massachusetts Institute of Technology
All rights reserved

Signature of Author __

.... vreuiamical Engineering
May 19 2005

Certified by _____

Ian Hunter

Professe

Accepted by _____

Professor Mechanical Engineering
Chariman, Department Committee on Graduate Students

BARKER

Development of Conducting Polymer Based Biomimetic Muscles and Fabrication
Techniques for an Artificial Pectoral Fish Fin

by
S. Naomi Davidson

Abstract

Fish possess a greater degree of agility, maneuverability, and energy efficiency over current underwater vehicles constructed by engineers. Kinematics studies show that a high degree of three-dimensional control of multiple active surfaces distributed around an undersea vehicle's center of mass is critical to achieve fish-like superior performance. However, current technology has yet to exploit the use of actively controlled surfaces for underwater locomotion. Major obstacles limiting effectively achieving designs capable of active deformations in multiple degrees of freedom lie in the complexity associated with traditional actuators and their associated manufacturing techniques. Conducting polymers possess numerous desirable physical and active properties which make it possible to grow rather than build artificial muscles for an articulated device. Their potential for co-fabrication make it possible to implement simpler more integrated designs as they have been shown to provide all the basic elements required for a Biomimetic robot including: force sensors (analogous to the Golgi organs in tendons), strain sensors (like muscle spindles), structural elements (such as bones, joints, and webbing), and actuators (akin to muscle). Rapid prototyping and molding techniques were used to begin the development of a co-fabrication process for a pectoral fin which will be made from and actuated by conducting polymers. Conducting polymer actuators provide the necessary structural flexibility while exceeding the 800 kN/m^2 force requirements typical of fish muscle by 40 fold. Maximum speed requirements of 2.1 Hz for swimming speeds up to 1.1 TLs^{-1} (total body length/s) are attainable at the strains required for metrics of the current artificial fin design.

Acknowledgments

Though my family didn't teach me how to do engineering, they did teach me how to be the best engineer I can be. I can't begin to measure the contribution of my father, Howard; my mother, Susan; and my brother, Josh. Josh is one of the people I admire most in the world, his strength and courage are beyond imagining. I am immensely fortunate to have all of their support, wisdom, and love.

Contents

1.0 Introduction

When we compare the current state of AUV (Autonomous Underwater Vehicle) technology with the stealth, efficiency, maneuverability and agility of fish we find the performance of man-made vehicles summarily lacking (Fish, 2003). In cases where an animal's functional performance far exceeds our own, careful observance and modeling of the driving forces for their superior capabilities can lead to significant gains. Analysis of the high performance maneuvers employed by fish versus those common to AUVs reveals fundamental limitations to the performance that can be expected from propeller designs (Fish, 2003; Kemp 2003). Paired pectoral fins are the primary thrust generators for low speed maneuvers in unsteady flow environments for many fish (Lauder, 2000). In kinematic analyses performed on pectoral fin swimming, data suggests that the source of the high performance of fish fins is due to active control of the fin's conformation. Engineers previously used rigid body dynamics to inform design parameters for underwater locomotion (Gibb, 1994). This assumption now appears to be insufficient as we discover more about controlled flexible foil swimming.

Investigation of the hydrodynamics and kinematics of fish fins during specialized maneuvering revealed four basic lessons indicating sources of their performance abilities. The first of these lessons involves the incorporation of multiple control surfaces (fins), which are widely distributed about the center of mass. A fish's fins vary in size and shape, and because of their positioning relative to the center of mass, allow refined control of large moments with relatively little force output. Second, these control surfaces must have a high degree of three-dimensional motion with flexible articulation relative to the body. The ability to rapidly reorient the fin surface allows the fish to generate and control a widely dynamic range of force vectors. This is the key to accomplishing the wide range of locomotor requirements for a single fin; for example, braking, turning, and hovering. Third, active conformational control of the fin surface enables fine tuning of body positioning for low-speed maneuvers. Again, small force outputs yield high performance results for precise movement control. Finally, fish simultaneously employ

these numerous control surfaces for maximum hydrodynamic efficiency. Analysis of wake interactions have shown that the dorsal fins are used in a variety of swimming routines to generate vorticity patterns which the caudal fin then capitalizes on for increased force generation, greater swimming efficiency, and improved maneuverability (Lauder 2003).

Achieving active control of in multiple degrees of freedom of flexible surfaces with motors and gears is extremely cumbersome. Traditional actuator technology is limited by rigidity, functionality, and physical footprint. Using motors, for example, to build an articulated fin accomplishing two of the four design goals outlined above becomes a significant challenge possibly even prohibitive. Artificial muscles, in particular conducting polymers as active smart materials, possess the characteristics necessary to create flexible yet active surfaces in almost any geometric construction (Bowers, 2004; Madden , et al., 2003). Integration of active materials into the structure of an underwater robotic device greatly simplifies the task of achieving active surface control. The potential for significant simplification exist not only in the manufacture and assembly of fins, but also in operational control of the mechanical device, and the effective achievement of the appropriate kinematics required for refined hydrodynamic control.

1.1 Conducting Polymer Materials in a Biorobotic Fish

Conducting polymers are a unique class of organic materials that, depending on the conditions of their synthesis, exhibit electrical conductivities ranging on the order of a semiconductive material to a highly conductive material as shown in Figure 1-1 (Madden, 2000). One of the many compelling functional uses of these polymers is their ability to convert electrical energy into mechanical energy through an electrochemical doping process. Volumetric changes in a synthesized film lead to active strains as ions are incorporated into or expelled from the material when a voltage potential is applied (Baughman, 1996). Conducting polymer actuators have been measured to exhibit stresses up to 40 MPa and strains as high as 26 % although typical strains are closer to 1

to 2 % (Kaneto, 2004; Madden, Madden, and Hunter, 2002; Madden, 2003). This force capacity exceeds that of skeletal muscle by as much as 100 fold or greater.

Conductivity Scale [S m⁻¹]

	Conductivity	
Superconductors	10^{20}	
	10^{15}	
	10^{10}	Theory:Polyacetylene $2e^9$
Cu $(6e^7)$		Polyacetylene
Graphite Hg	10^5	Polypyrrole Polyaniline
Ge	1	Range for Conducting Polymers
Si		DNA
AgBr	10^{-5}	
Glass	10^{-10}	
Diamond		PVC
$(SiO_2)_n$	10^{-15}	PE
	10^{-20}	PTFE
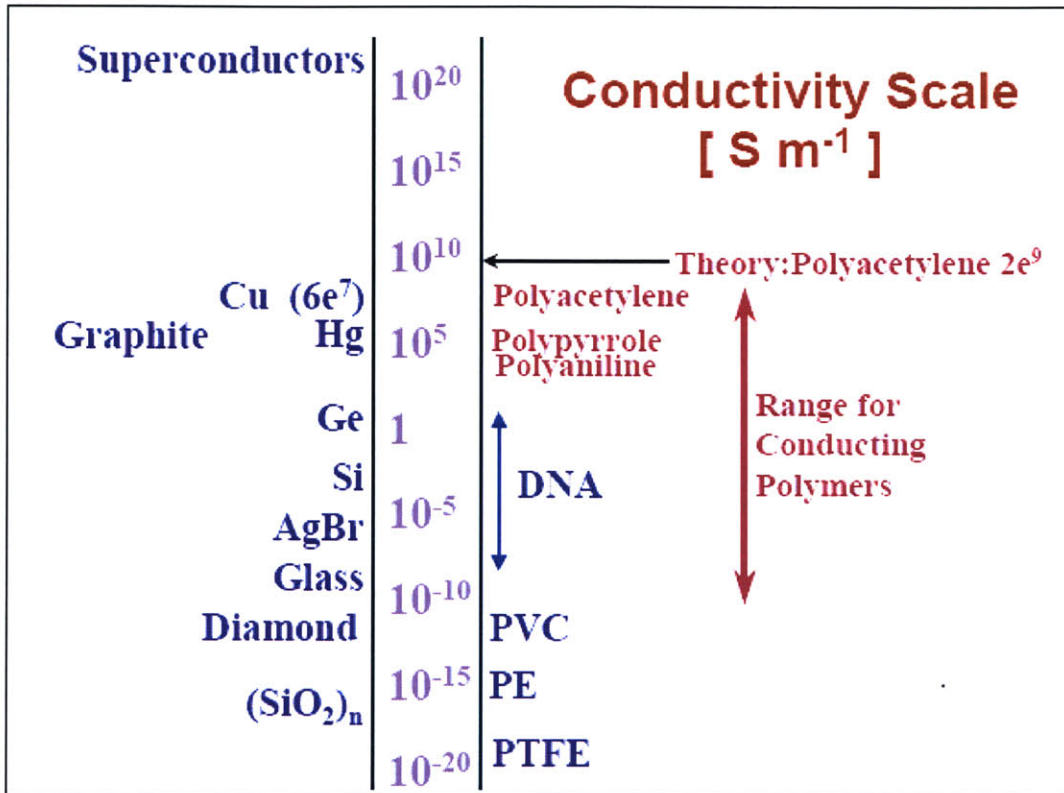
Figure 1-1. A comparison of conductivities of common materials with conducting polymers (PE is polyethylene, PVC is polyvinylchloride and PTFE is polytetrafluoroethylene or Teflon©). (Source: Madden, 2000)

The active properties of these materials along with the inexpensive nature of their synthesis and manufacture places these materials in the operational range of many commercially used actuation technologies (Hunter, 1992, Bar-Cohen, 2001). In Table 1 a comparison of polypyrrole, a commonly used and well characterized conducting polymer, is made against many currently available and commercially successful actuators.

Table 1-1. Comparison between conducting polymers, natural muscle and other commercially available actuation technologies (Source: adapted from Kornbluh 2002).

Actuator Technology	Maximum Strain (%)	Maximum Pressure (MPa)	Relative Speed
Natural Muscle (Human Skeletal)	100	0.8	Slow
Electromagnetic (Voice Coil)	50	0.1	Fast
Conducting Polymer (Polypyrrole)	26	34	Slow
Shape Memory Alloy (TiNi)	>5	>200	Slow
Piezoelectric (Ceramic - PZT)	0.2	110	Fast

Muscle is a distinctively advantageous actuation material because it has multiple integrated functions. Due to its material properties, it can be used effectively to provide breaking force, restoring energy as a spring, and structural integrity much like a strut. Work-loop experiments have shown, as expected, that muscles produce positive power as motors (Full, 2002). However, careful examination of the kinematics and kinetics of a variety of animals during locomotion also revealed muscular activity providing braking force for enhanced stability, tunable spring stiffness for energy efficiency and passive stability control, and structural integrity as struts. The multifunctional characteristic of muscle allows for greater integration, which in turn drives greater simplification in the architecture of specialized locomotory behavior. It has been shown in animals ranging from cockroaches to fish that capitalizing on the unique properties of muscle allows them to achieve highly specialized maneuverability in unpredictable terrains with relatively simple nervous systems, high energy efficiency, and robust operation even with broken or damaged appendages (Dickinson, 2000; Full, 2001).

Conducting polymers, such as polypyrrole, belong to a class of actuators known as artificial muscle because they also possess this multifunctional nature. This unique class of materials not only possess active properties like muscle they also exhibit a variety of passive mechanical and electrical properties (Bowers 2004, Spinks 2003, Madden, et al., 2001). Exploiting the active capacities of these materials in order to do mechanical work is not their only functional use. Researchers have demonstrated the successful fabrication of transistors, strain gages, chemical sensors, batteries, super capacitors, and photodiodes

as well. It is therefore conceivable that an entire electromechanical device could be constructed from conducting polymers alone (Madden, 2003).

There are many potential benefits for utilizing materials possessing such versatile functionality. A potential benefit explored in the scope of this work is the construction of an active co-fabricated device. The co-fabrication of a biorobotic mechanism, or "growth" of an electromechanical machine as it is intended here, is attractive because it greatly enables the simplification of manufacturing processes while enhancing control over geometric and structural design constraints. In this thesis rapid prototyping and mold making techniques were used to build a working model of the pectoral fin for an artificial fish basing the design on parameters governed by the Bluegill Sunfish. The goal within the scope of this work was not to mimic the biological fin exactly as it is far too complex to effectively recreate (Dickinson, 2000; Full, 1999; Full, 2001). However, basic design parameters were extracted in a simplified functional model using kinematic and kinetic analysis from biological study. Means of integrating the conducting polymer actuators into the design were explored on the level of actuator development and co-fabrication techniques.

1.2 References

1. Ahn A. H., Full R. J. A Motor and a Brake: Two Leg Extensor Muscles Acting at Same Joint Manage Energy Differently in a Running Insect. The Journal of Experimental Biology. 2002; 205:379–389.

2. Bandyopadhyay, P. R. Maneuvering Hydrodynamics of Fish and Small Underwater Vehicles. Integrative and Comparative Biology. 2002; 42:102–117.

3. Baughman, R. H. Conducting Polymer Artificial Muscles. Synthetic Metals. 1996; 78: 339-353.

4. Bar-Cohen, Y. Electroactive Polymer (EAP) Actuators as Artificial Muscles: Reality, Potential, and Challenges. SPIE-International Society for Optical Engineering. 2001.

5. Bowers T. A. Modeling, Simulation, and Control of a Polypyrrole-Based Conducting Polymer Actuator, Masters Thesis. Cambridge, MA: Massachusetts Institute of Technology; 2004.

6. Dickinson, M., Farley, C., Full, R., Koehl M., Kram, R., Lehman, S. How Animals Move: An Integrative View. Science. 2000; 288: 100-106.

7. Gibb, A. C., Jayne, B. C., Lauder, G. V. Kinematics of Pectoral Fin Locomotion in the Bluegill Sunfish Lepomis Macrochirus. Journal of Experimental Biology. 1994; 189: 133-161.

8. Hunter, I., Lafontaine, S. A Comparison of Muscle with Artificial Actuators. Technical Digest IEEE Solid State Sensors and Actuators Workshop IEEE. 1992; 178-175.

9. Kornbluh R., Pelrine R., Pei Q., Stanford R., Oh S., and Eckerle J. Industrial and Commercial Applications Structures Technologies. 2002: Smart Structures and Materials Proc. SPIE, Vol. 4698.

10. Fish, F. E., Lauder, G. V., Mittal, R., Techet, A. H., Triantafyllou, M. S. Conceptual Design for the Construction of a Biorobotic AUV Based on Biological Hydrodynamics. Proceedings 13th International Symposium on Unmanned Untethered Submersible Technology. August 24-27 2003.

11. Full, R.J. and Koditschek, D. Templates and Anchors: Neuromechanical Hypotheses of Legged Locomotion on Land. Journal of Experimental Biology, 1999, 202, 3325-3332.

12. Full, R.J. and Meijer, K. Metrics of Natural Muscle Function. In Y. Bar-Cohen (ed.) Electro Active Polymers (EAP) as Artificial Muscles, Reality Potential and Challenges. SPIE and William Andrew/Noyes Publications. 2001: pp. 67-83.

13. Kemp, M., Hobson, B., Pell, C. Energetics of the Oscillating Fin Thruster. Proceedings 13th International Symposium on Unmanned Untethered Submersible Technology. 2003 August: 24-27.

14. Lauder G. V., Drucker, E. G. Morphology and Experimental Hydrodynamics of Fish Fin Control Surfaces. Proceedings 13th International Symposium on Unmanned Untethered Submersible Technology. 2003 August: 24-27.

15. Lauder, G.V. Function of the Caudal Fin During Locomotion in Fishes: Kinematics, Flow Visualization, and Evolutionary Patterns. American Zoologist. 2000; 40: 101-122.

16. Madden, J. D. Conducting Polymer Actuators, Ph. D. Thesis. Cambridge, MA: Massachusetts Institute of Technology: 2000.

17. Madden, J. D., Madden, P. G., Hunter, I. Conducting Polymer Actuators as Engineering Materials. Smart Structures and Materials 2002: Electroactive

Polymer Actuators and Devices (EAPAD), Yoseph Bar-Cohen, Ed., Proceedings of SPIE. 2002; 4695: 176-190.

18. Madden J., Schmid B., Botha R., Hechinger M., Lafontaine S., Madden P., Hover F., McLetchie K., Hunter I. Polymer Actuated Variable Camber Foils. Proceedings 13th International Symposium on Unmanned Untethered Submersible Technology. 2003 August: 24-27.

19. Madden P., Madden J., Anquetil P., Yu H., Swager T., Hunter Il Conducting Polymers as Building Blocks for Biomimetic Systems. 2001 Bio-Robotics Symposium, The University of New Hampshire. 2001 August 27 - 29.

20. Madden, P. G. Development and Modeling of Conducting Polymer Actuators and the Fabrication of a Conducting Polymer Based Feedback Loop, Ph. D. Thesis. Cambridge, MA: Massachusetts Institute of Technology: 2003.

2.0 Background Theory

2.1 Pectoral Fish Fin

The relative performance of fish far exceed current underwater vehicle technology and is particularly impressive in the unsteady flow environments of wake zones. Fish are able to easily and stealthily negotiate high performance maneuvers such as turning on a dime, rapid reorientation and acceleration, and hovering regardless of rapid changes in the flow around them. Biologists and engineers are keenly interested in the source of this difference in performance (Bandyopadhyay, 2002; Lauder and Drucker 2004)

In a survey of the underwater kingdom there are many varieties of control surfaces that have evolved between different fishes (as well as on a given fish) in the form of multiple fins located about their center of mass. Using these control surfaces animals capitalize on three types of force generation: pressure drag, acceleration reaction, and lift. These forces are either actively or passively controlled through refined manipulation of flow over the surface of the fin (Fish, 2003). The complex interaction between multiple control surfaces on a fish's body has yet to be fully quantified. Until recently there was very little data illuminating the thrust partitioning between fins during swimming maneuvers as each fin was studied individually. Although in its infancy, the study of thrust partitioning for a Bluegill Sunfish has been performed at a speed of 1.1 TL·s^{-1} (total body lengths per second). Figure 2-4 below summarizes the results of this study with a breakdown of the relative thrust contribution from each fin group during two basic swimming maneuvers; steady swimming and the initiation of a turn. At this speed the pectoral fins account for 50 % - 65 % of thrust generation (Lauder and Drucker, 2004). Research shows that at low speeds paired pectoral fins are the primary control surfaces used for executing maneuvers, they are also essential for enhancing stability during propulsion (Wilga and Lauder, 1999, 2000, 2001).

A

Soft dorsal:
9.1 ± 1.5 mN
(12.1%)

Pectoral:
37.6 ± 13.6 mN
(50.0%)

Caudal:
28.5 ± 1.9 mN
(37.9%)

B

Soft dorsal:
11.2 ± 2.0 mN
(34.9%)
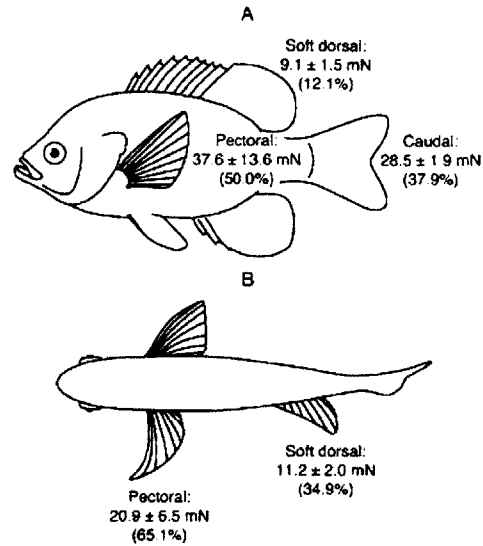
Pectoral:
20.9 ± 6.5 mN
(65.1%)

Figure 2-4. The components of wake force contributed by different fins of bluegill sunfish during a swimming were averaged over a stroke. The percent contribution of the force from each fin is reported in parentheses. The thrust generated from the soft dorsal, caudal, and pectoral fins during steady swimming maneuver at 1.1 TL·s^{-1} (A). A single pectoral fin produces a large amount of force in a turning maneuver. (Copied from: Lauder and Drucker 2004)

As we endeavor to match the agility and performance of nature's swimmers it is clear that there is much to be learned from using multiple control surfaces to achieve maneuverability and propulsion. Research shows that fish capitalize on these flexible foils for a variety of purposes (Kemp, 2003). By distributing multiple fins about their center of mass they are able to rapidly change the direction of the applied force on the flow over the body.

Studies have demonstrated that fish are able to actively control the conformation of the fin's surface and at lower speeds pectoral fins in particular are the primary source of thrust generation. This is enabled by a complex bone structure and multiple muscle and tendon attachments on each fin ray. Figure 2-5 shows a dissected image of the muscular and tendon attachments on the fin rays. Several layers of muscle are revealed (Figure 2-5 (B)). Each fin ray is controlled by a minimum of four muscles with its own tendon attachment at the base of the fin ray (Figure 2-5 (C)). This allows the fish to exert refined control over the direction and movement of each fin ray. The result of which is the cupping and curling the fin surface in the water for the active adjustment of stiffness,

surface area, and force generation. The control fish exert on the conformation of their fin translates to an ability to rapidly and efficiently exploit the hydrodynamics of their environment. Because classic approaches to underwater vehicle design have focused on rigid body dynamics, the focus of this project was to explore the effects of employing an actively controlled flexible foil.
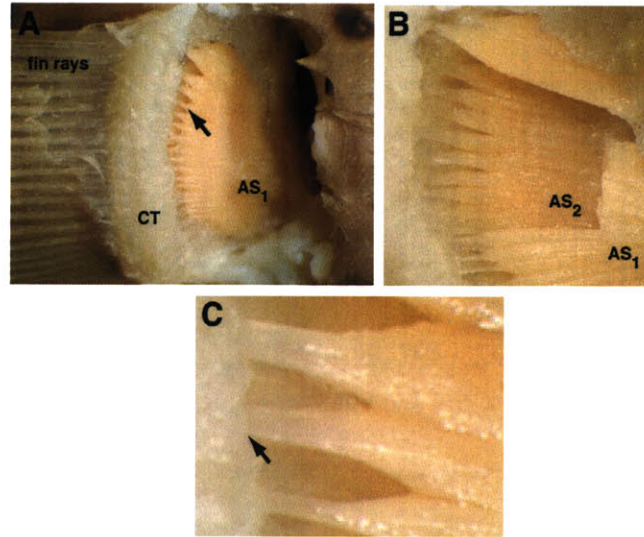
Figure 2-5. A dissected image of the pectoral fin of a Bluegill Sunfish reveals the complex muscular arrangement (A) at the base of the fin rays and the large connective tissue pad (CT) that attaches via tendons to the adductor superficialis (AS) muscles. As the upper layer of muscle tissue is cut (B) another set of muscles are revealed. The adductor superficialis has two distinct layers -- superficial (AS_1) and deep (AS_2) is also composed of discrete bundles of fibers. Each fin ray is controlled by a minimum of four muscles each with a specific tendon attachment allowing the fish to exert refined control over the direction of movement of each fin ray (Copied from: Lauder and Drucker, 2004).

The Bluegill Sunfish was chosen as a base model for informing the kinematics of swimming with active conformational control over the fin surface. It is a classic pectoral fin swimmer at swimming speeds below approximately 1.1 TL·s^{-1} (Gibb, 1994). Pectoral fin swimming is characterized by highly agile and finely controlled positioning in an unsteady flow environment. Fish are able to hover looking for food and rapidly react to the presence of predators and prey. The pectoral fin is powerful enough to perform the steady swimming requirement while enabling breaking, turning on a dime, hovering, and rapid reorientation and accelerations. The Bluegill Sunfish was chosen for this project

because it possesses a representative fin morphology, is locally prolific, and exhibits the desired swimming abilities.

2.2 Modeling and Description of Actuator Characteristics

While conducting polymers are a compelling technology there is still room for discovery and characterization in their development as an engineering material. This is the aim of the work covered in Chapter 3 of this thesis. Polypyrrole can generate active stresses as high as 40 MPa (two orders of magnitude greater than natural muscle) (Madden, 2002; Madden, 2001); exhibit maximum strains on the order of 10 to 26 % (Anquetil, 2004; Bay, 2003; Madden, 2002; Madden, 2002; Kaneto, 2004) although typical values for actuators are generally 1-2 % strain; and possess an elastic deformation range of up to 16 MPa (although at these stresses creep is an issue if forces are applied for more than a few minutes). Notable limitations in the use of these actuators is their relatively slow speed response, low electrical to mechanical efficiencies (~1 %), and the requirement of an ion bath. In order to better understand these limitations and possible sources for enhanced performance, this section includes a discussion of the current understanding of the process by which electrical energy is converted to mechanical in these actuators and the model currently used to predict this behavior.

Polypyrrole is the conducting polymer actuator used for the focus of this thesis. It was chosen because it is one of the more robust of the electrochemically synthesized polymers, it is well studied, and models predicting its mechanical response have been developed. The source of conductivity in the polymer is a conjugated backbone of double bonds as shown in Figure 2-1. The conjugated molecular structure allows the delocalization of electrons along the backbone when a voltage is applied (Madden , 2000; Madden, et al., 2-001; Roth, 1995). This localized charge initiates the flow of ions into and out of the material as the charge is balanced. Conductivity is therefore sensitive to the structure of the polymer and the orientation of polymer chains within the material matrix. Synthesis conditions therefore greatly affect conductivity by impacting this mechanism for charge flow.
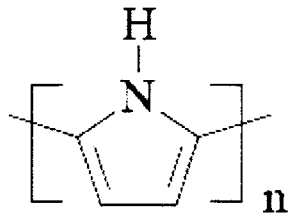
Polypyrrole (PPy)

Figure 2-1. An illustration of the molecular structure shows the conjugated backbone of polypyrrole. (Source: Madden, 2002)

Electrochemical synthesis leads to the highest conductivity and the best mechanical properties recorded, for polypyrrole a typical conductivity is approximately 10^4 S·m^{-1} (Madden, 2000). The mechanism for expansion or contraction of the polymer is driven by the migration of ions into or out of the material matrix. The result of this flow of ions is a change in volume (V) and subsequent strain (ϵ). Equation 2-1 describes the following linear relationship between strain and injected to injected charge (Q):

$$\varepsilon = \alpha \frac{Q}{V},$$
2-1

where charge density ratio (α) for polypyrrole is typically on the order of 10^{-10} C^{-1}·m^3. The charge density ratio is governed by synthesis conditions as it is determined by the polymer structure discussed earlier (Madden, 2002; Madden, 2000; Madden, et al., 2003). Figure 2-2 shows a currently accepted circuit model of the impedance characteristics driving flow of charge for these electrochemical actuators. The impedance relationship between voltage source V, the double layer capacitance at the interface between the polymer and the electrolyte C, the electrical impedance due to the electrolyte and contact resistance R, and the diffusion impedance for mass transport into the polymer Z_D are shown.

19
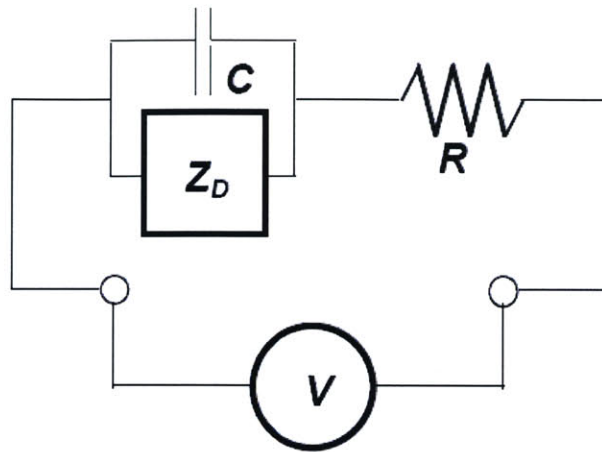
Figure 2-2. Circuit diagram describes actuator impedance for electrochemical actuators. (Source: Madden, et. al., 2002)

Geometry is a critical factor in modeling the behavior of electrochemical actuators. For the sake of simplicity, the parallel plate geometry shown in Figure 2-3 is assumed for all instances discussed here.
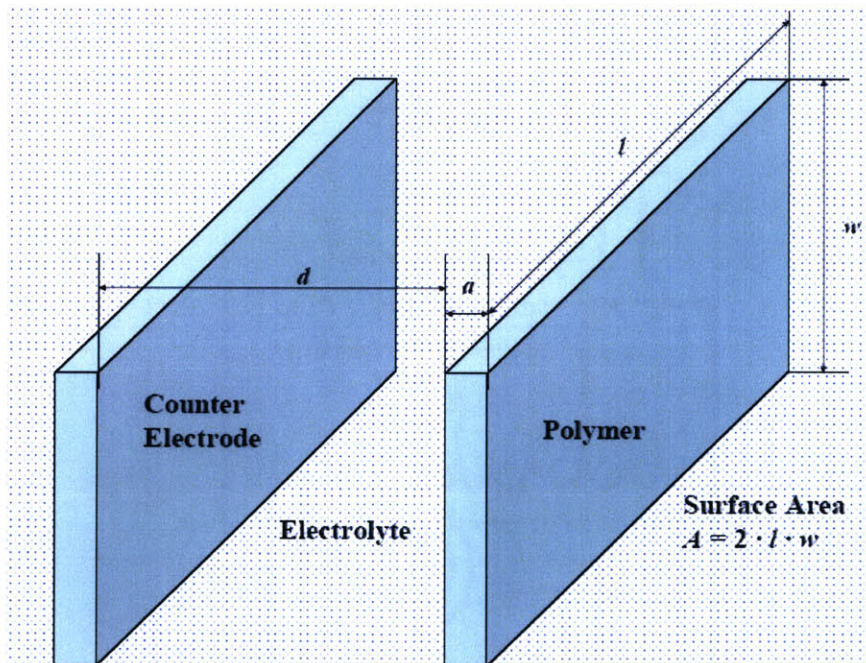

Figure 2-3. Parallel plate geometry used for modeling actuator behavior. Copied from: Madden, et al., 2002)

To begin, the diffusion impedance is given in the Laplace domain between the polymer and counter electrode at frequencies in the range of 100 μHz – 100 kHz:

$$Z_D = \frac{\delta}{a \cdot C \cdot s} = \frac{1}{C_V \cdot Vol},$$

2-2

where the a is the polymer thickness, δ is the double layer thickness, C is the double layer capacitance, C_V is the double layer capacitance per unit volume, and Vol is the volume of the polymer. There are three time constants governing the speed of reaction/contraction: double layer charging time, volumetric charging through the polymer and mass transport of ions balancing charge in the film.

Since the charge in the double layer initiates flow of ions into the polymer, no charge transfer can take place until it has reached a sufficient level. The time constant for the double layer is:

$$\tau_{RC} = R \cdot C = \frac{d}{\sigma_e \cdot A} = \frac{d}{\sigma_e} \cdot \frac{\partial C}{\partial A},$$

2-3

where A is the surface are of the polymer film, d is the separation between the film and the counter electrode, and σ_e is the conductivity of the liquid electrolyte. Typical values for conductivities of the electrolyte are 1 to 10 S·m^{-1} while the double layer capacitance is commonly 0.1 to 0.4 F·m^{-2} (Madden, 2000; Madden, et. al., 2002). Given these typical values, for a response time of 1 ms, the separation between the polymer and the counter electrode should be from 10 to 100 mm or less.

Volumetric charging has a greater effect on reaction time as charge density must be transmitted through an internal resistance. Polypyrrole exhibits capacitor-like behavior for which the volumetric charging has two important situations governing the speed of actuation. In the first case, the electrolyte resistance is large relative to the polymer resistance, and is given by:

$$\tau_{RCV} = R \cdot C_V \cdot Vol = \frac{d \cdot a}{2 \cdot \sigma_e} \cdot C_V,$$

2-4

where the reaction time is governed by the film thickness and the distance between the actuator and the counter electrode proportionally to the double layer charging time. In the second case, the polymer resistance is significant relative to the electrolyte resistance. Here the volumetric charging time constant is:

$$\tau_{RCVP} = R_P \cdot C_V = \frac{l^2}{4 \cdot \sigma_e} \cdot C_V ,$$ 2-5

where the volumetric charging time is increased by the square of the distance between electrode attachment points and is only mitigated by the factor of four when the actuator is connected at both ends.

Finally, the strongest factor dominating response time is the mass transport phenomenon.

$$\tau_D = \frac{a^2}{4 \cdot D}$$ 2-6

The diffusion coefficient, D, in hexafluorophosphate-doped polypyrrole ranges between 0.7 to 7×10^{-12} $m^2 \cdot s^{-1}$ (Madden, 2000; Madden, et al., 2002) and the reduction in time by a factor of four is only relevant if the film is exposed to ionic flow from both the front and back face.

One other factor governing reaction speed should be discussed. It would seem that since the capacitance is linear with voltage, doubling the maximum potential applied to the polymer would double the concentration and hence the charging rate. This is true to an extent but unfortunately, a limit exists on the maximum potential that can be applied to a film. Exceeding this limit causes film degradation and ultimately will result in destruction of the actuator. Because films have a limit on their actuation potential there is a corresponding limit to the current which can be driven through the film by raising the applied voltage. One method employed to mitigate this effect is to use a strategy of actuation known as resistance compensation. Essentially, an applied voltage, V, is determined assuming a maximum voltage, V_{dl}^{max}, at the double layer of the polymer which is to be reached but not exceeded including a compensation factor for the resistance drop, $I \cdot R$, through the electrolyte.

$$V = V_{dl}^{max} - I \cdot R$$ 2-7

Using this resistance compensation method increases the speed of actuation by maintaining the maximum potential gradient in the double layer (Madden, 2000; Madden, et al., 2002)

Given the above conditions, there are several considerations which may be addressed either in actuator development or implementation in a design:

- The distance between electrodes, d, and electrical attachment points, l, should be minimized,
- Film thickness should also be minimized within appropriate force constraints,
- The degradation potential should be maximized.

Methods of increasing the performance of actuators based on the constraints discussed here are explored in further detail in Chapter three.

2.3 Design of an Artificial Fish Fin

While the inspiration to mimic the performance of fish in terms of their ability to maneuver efficiently, stealthily, and with tremendous agility is obviously enticing the process for doing so can be tricky. Replicating the complex physiology of the biological system is prohibitive, particularly with classic engineering technology. It is imperative in this sense to endeavor to identify systemic level simplifications in the design rather than trying to copy nature. This obviously entails achieving a detailed understanding of the physiology and kinematics of biological locomotor systems (Full, 2002). Through this understanding it is possible to overcome limitations in achieving equally performing mechanisms. Primary issues stem from the limitations on classic mechatronic technology, which is generally far too cumbersome and inefficient. Parts in the system are only able to perform singular functions forcing the incorporation of multiple devices to accomplish what nature might with a single element. Furthermore, each connection carries with it its own hardware, friction, stiction, backlash, and vulnerability to wear. Conducting polymer actuators are a suitable actuator and possibly disruptive technology for this application in that they are flexible and easily integrated into any geometric configuration, can be synthesized directly into the mechatronic device, are silently

operated, and can provide a multitude of other functional abilities such as sensing (Lauder and Drucker, 2004; Madden, et. al., 2003; Madden, 2002; Madden, et al., 2001).

The speed and force capabilities of these actuators are within the measured outputs of the Bluegill Sunfish with maximum required frequencies of 1.2 to 2.1 Hz and forces of 100 to 200 mN. The peak power requirement measured for the Sunfish pectoral fin muscle was 27 W/kg. Polypyrrole outstrips this peak power requirement by as much as 44 %; typically delivering as much as 39 W/kg (Gibb, 1994). The possibility of matching the performance of fish-like swimming becomes a reality as conducting polymers can potentially reduce the complexity of the mechanical design while delivering the necessary actuation requirements for high maneuverability swimming.

2.4 Chapter References

1. Anquetil P. Large Contraction Conducting Polymer Actuators, Ph D. Thesis. Cambridge, Ma: Massachusetts Institute of Technology: 2005.

2. Bay L., West K., Sommer-Larsen P., Skaarup S., Benslimane M. A Conducting Polymer Artificial Muscle with 12 % Linear Strain. Advanced Materials. 2003 Feb 17; v 15, n 4: p 310-313.

3. Bandyopadhyay, P. R. Maneuvering Hydrodynamics of Fish and Small Underwater Vehicles. Integrative and Comparative Biology. 2002; 42:102–117.

4. Gibb, A. C., Jayne, B. C., Lauder, G. V. Kinematics of Pectoral Fin Locomotion in the Bluegill Sunfish Lepomis Macrochirus. Journal of Experimental Biology. 1994; 189: 133-161.

5. Full, R.J. and Meijer, K. Metrics of Natural Muscle Function. In Y. Bar-Cohen (ed.) Electro Active Polymers (EAP) as Artificial Muscles, Reality Potential and Challenges. SPIE and William Andrew/Noyes Publications. 2001: pp. 67-83.

6. Kemp, M., Hobson, B., Pell, C. Energetics of the Oscillating Fin Thruster. Proceedings 13th International Symposium on Unmanned Untethered Submersible Technology. 2003 August: 24-27.

7. Lauder G. V., Drucker E. G., Morphology and Exerimental Hydrodynamics of Fish Fin Control Surfaces, IEEE Journal of Oceanic Engineering, v 29, n3, Jul 2004, pp. 556-571.

8. Madden, J. D. Conducting Polymer Actuators, Ph. D. Thesis. Cambridge, MA: Massachusetts Institute of Technology: 2000.

9. Madden, J. D., Madden, P. G., Hunter, I. Conducting Polymer Actuators as Engineering Materials. Smart Structures and Materials 2002: Electroactive Polymer Actuators and Devices (EAPAD), Yoseph Bar-Cohen, Ed., Proceedings of SPIE. 2002; 4695: 176-190.

10. Madden J., Schmid B., Botha R., Hechinger M., Lafontaine S., Madden P., Hover F., McLetchie K., Hunter I. Polymer Actuated Variable Camber Foils. Proceedings 13th International Symposium on Unmanned Untethered Submersible Technology. 2003 August: 24-27.

11. Madden, P. G. Development and Modeling of Conducting Polymer Actuators and the Fabrication of a Conducting Polymer Based Feedback Loop, Ph. D. Thesis. Cambridge, MA: Massachusetts Institute of Technology: 2003.

12. Madden P., Madden J., Anquetil P., Yu H., Swager T., Hunter Il Conducting Polymers as Building Blocks for Biomimetic Systems. 2001 Bio-Robotics Symposium, The University of New Hampshire. 2001 August 27 – 29.

13. Wilga C., Lauder G. Locomotion in Sturgeon: Function of the Pectoral Fins. Journal of Experimental Biology. 1999; 202: 2413-2432.

14. Wilga C., Lauder G. Three-dimensional Kinematics and Wake Structure of the Pectoral Fins During Locomotion in Leopard Sharks Triakis semisfasciata. Journal of Experimental Biology. 2000; 203:2261-2278.

15. Wilga C., Lauder G. Functional Morphology of the Pectoral Fins in Bamboo Sharks, Chiloscyllium plagiosum: Benthic vs. Pelagic Staion Holding, Journal of Morpology. 2001; 249:195-209.

3.0 Actuator Development

Conducting polymers are attractive as a disruptive actuator technology over classical actuation systems because they are:

- lightweight,
- have high power-to-mass density,
- inexpensive to produce,
- silently operated,
- operated at low voltages,
- multifunctional such that single elements of a typical mechatronic device can be built without the incorporation of multiple parts,
- flexible (like muscle) which allows them to be wrapped around corners or incorporated into many different environments.

Current actuator technologies are limited in their ability to deliver all of these characteristics simultaneously. Table 3-1 summarizes many features of the conducting polymers as artificial muscles as they compare with mammalian skeletal muscle. As is evident in this list of properties, one of the major drawbacks to the polymers is the slow speed of actuation. Response times of skeletal muscle are over an order of magnitude faster than polypyrrole. Polymer contraction rates are their most rapid close to 3 %/s in contrast to the 100 %/s associated with muscle. Conducting polymers are also limited in strain output, where the average reliable strain is close to 2 % while muscle is typically capable of 20 to 40 % total relative contraction (Hunter, 1992; Madden, et al., 2002; Spinks, 2003). However, polypyrrole is over 100× stronger than muscle supporting maximum stresses as high as 40 MPa and at a significantly higher power-to-mass ratio. Coupled with the features listed above these actuators show commercial and industrial promise despite the limitations just mentioned. In order make these artificial muscles a truly versatile actuator technology; improvements in speed and/or strain are definitely required.

Table 3-1. The properties of polypyrrole as they compare to mammalian skeletal muscle show some of the strengths and limitations as an actuator technology (Source: Hunter, 1992; Anquetil, 2004).

Property	Mammalian Skeletal Muscle	Polypyrrole in 0.1 M TEAP in PC
Displacement (Strain)	20 to 40 %	2 % (at 10 MPa)
Max Active Stress (Load)	0.35 MPa	40 MPa
Max Velocity (Strain Rate)	100 %/s	3 %/s (at 5 MPa)
Power to mass	50 to 100 W/kg	150 W/kg (at 5 MPa)
Efficiency	30 to 35 %	0.6 % (at 4 MPa) 3 % (at 30 MPa)
Stiffness (wet)	0.3 to 80 MPa (contracted)	0.8 GPa
Tensile Strength (wet)	0.3 MPa	20 to 85 MPa
Conductivity	-	4.5×10^4 S/m
Lifetime	10^7	10^5 (at 0.3 %)

In this chapter several fabrication methods were investigated with the hope of increasing the performance of polypyrrole. The driving force in conversion of electrical to mechanical energy in these actuators is the diffusion of ions into the material; this is also the major limiting factor in the speed of operation. Improving the strain rates involves manipulation of any one of the following factors (Madden, 2002):

- increasing the charging rate of the polymer such that ion flow into the material, occurs at a faster rate without sacrificing the strain-to-charge ratio,
- increasing the strain-to-charge ratio without losing efficiency of the charging rate,
- charging the double layer as quickly as possible.

The underlying strategy behind the methods employed in the scope of this work focused on increasing the charging rate in some manner. There are several ways to achieve this some of which have potential drawbacks as well as gains. For instance, increasing the charging rate of the polymer could potentially be achieved by changing the surface of the

film such that ions flow more freely through the membrane. However, this can lead to negative consequences. In the most efficient scenario only one ion, the relatively small anion, is the only mobile species balancing charge. Changes in the polymer that might enable or increase motion of the cation into the polymer during actuation would decrease the speed of reaction (Spinks, 2003; Madden, 2003). In the same vein, smaller dopant molecules with their increased mobility diffuse into the polymer more rapidly also increasing charging rate. However, this can decrease the strain-to-charge ratio as the film's volumetric expansion is dependent on the incorporation of ions into its matrix. The following discussion explores several different methods of increasing the performance of conducting polymer actuators.

Maximum Voltage Application

Another means of increasing the rate of reaction is to apply higher voltages. This increases the gradient at the double layer interface with the film which leads to an improved rate of charge flow (Otero, 1999, Madden, 2000; Madden, 2003; Spinks, 2003). For diffusion based reactions, the strain rates will depend on the difference between the polymer ion concentration and the double layer concentration as the ions move to balance charge between material and electrolyte. The greater the concentration gradient at this interface the faster the flow of ions will occur thereby increasing the strain rate (Madden, 2003). Increasing the applied voltage raises the concentration gradient. Unfortunately, there is a limit on the maximum potential (degradation potential) which can be applied to the polymer. Exceeding this limit leads to degradation and even destruction of the actuator. Methods for pushing this ceiling involve changes in chemical structure of either the polymer or the electrolyte (Madden, 2003).

Electrolyte Resistance

Because of the resistance between the polymer and the electrolyte there can be a potential drop at the interface. A method of charging the double layer as quickly as possible by compensating for the interfacial resistance was developed by Madden et. al. and involves applying rapid pulses of voltages exceeding the degradation potential. This brief application of a high voltage across the film brings it to the desired voltage as rapidly as

possible without degradation affects (Madden, 2000). This strategy, known as resistance compensation, involves applying a shaped potential which initiates a large potential pulse that diminishes as the ohmic drop decreases. The resistance between the polymer and the electrolyte is estimated from measurements of the current draw upon application of the initial voltage pulse. The potential is adjusted as the difference between the applied potential and the estimated solution potential drop is less than or equal to the desired potential across the polymer (Madden, et al., 2000). In active tests performed in this chapter this resistance compensation technique was used.

Actuator Resistance

Another method of increasing the performance of these actuators is to decrease the resistance generated in the course of achieving electrical connection with the polymer. As the resistance compensation method seeks to mitigate this effect by applying an adjusted voltage, decreasing the effect at the design level is also important. Achieving minimum cell resistance can be accomplished by reducing the resistance of the polymer itself or by incorporating conductive materials into the matrix of the polymer. Several different strategies involving embedding gold which is highly conductive ($\sigma = 4.5 \times 10^7$ $S\cdot m^{-1}$) with polypyrrole ($\sigma = 10^4$ $S\cdot m^{-1}$). The aim of incorporating the conductive material was to diminish either the cell resistance at the working electrode or along the length of the polymer. While the incorporation of materials into the polymer can decrease the contact resistance, or the overall resistance of the polymer, they can also lead to earlier mechanical failure and increased mechanical impedance within the actuator. As fabrication methods following this model were explored, these potentially negative effects were also examined.

Actuator Length

Because of the relatively small strains for polypyrrole, long polymer strips are often necessary. Unfortunately, long actuators reduce the speed of response as they increase the overall resistance of the film. Increasing the speed of actuation by decreasing the thickness of the film has a positive effect in that it proportionally reduces the time constant due to volumetric charging of the film (see Equation 2-4). However, the thin

film creates greater resistance to current flow. The relationship between voltage drop, V, along the length, x, of a polymer film is given by:

$$V = \int \frac{I(x)}{(A \cdot \sigma)} dx,$$ 3-1

where I is the current density, σ is the conductivity, and A is the cross-sectional area of the film (Madden, 2003). The voltage drop has a negative effect on the speed of actuation because it lowers the potential at the double layer thereby decreasing the rate of flow of ions into the polymer. For many actuator applications then, these two parameters seem to be at odds. Long actuators are needed for increased strain, and thin actuators increase speed but also reduce the efficiency of the flow of ions. In a study conducted by Peter Madden two films were synthesized; both of which were 120 mm in length but had different cross-sectional areas. The thin film had a relatively low conductivity of 496 $S \cdot m^{-1}$ and a cross-sectional surface area of 6.4×10^{-8} m^2 while the thick film was 6920 $S \cdot m^{-1}$ with a cross-sectional surface area of 3.0×10^{-7} m^2. In measurements of the potential along the length of these two films, under the application of an equivalent signal, Madden measured a total drop of approximately 70 % in the case of the high resistance strip versus a 30 % drop in voltage over the length of the low resistance strip. There are two ways to mitigate the negative effects of increasing the resistance of the polymer actuator when long or thin films are required. The first is to decrease the distance between the electrical connections and the second is to reduce the resistance of the polymer.

Strain to Charge Ratio

Increasing the strain-to-charge ratio is another means of enhancing the strain rates of these actuators. In one study it was reported that increasing the size of the mobile ion into the polymer had such an effect (Kaneto, 2004). Another effect that can occur within the electrolyte bath during actuation is the incorporation of solvent molecules as ions flow through the polymer. In this way, the added volume of the solvent leads to a greater strain-to-charge ratio (Madden, 2002; Otero, 1998). Although much work can be done with the choice of solvent in terms of developing the speed and strain rates of conducting polymer actuators, this was not explored within this thesis.

Elastic Modulus

Another material property which should be mentioned is the elastic modulus of the synthesized films. Decreasing the stiffness of the film will allow larger displacements for a given load. Increasing the modulus, E, has the effect of increasing the stress, σ, that that can be applied to the actuator:

$$\sigma = E\varepsilon + \alpha E\rho .\qquad\qquad\qquad 3\text{-}2$$

where ϵ is the strain, α is the strain/charge ratio, and ρ is the charge density. A greater Young's modulus is therefore a desirable effect as it increases the stress that can be generated per unit charge (Madden, 2003).

Actuator Testing

Several methods for increasing the performance of polypyrrole actuators were explored in this chapter. Some techniques involved the incorporation of materials into the matrix of the actuator either for the purpose of increasing the overall conductivity, decreasing the distance between electrodes, or reducing the resistance at the electrical connection sights. Changes in the material properties of the films were also explored at the synthesis level. The fabrication methods are detailed and the results of these growth techniques were quantified through measurements of their active properties. Active testing was performed on the actuators in a dynamic mechanical analysis (DMA) device that was designed and built to measure conducting polymer films under isotonic actuation conditions (Madden, and Rinderknecht, 2002; Rinderknecht, 2002). The specifications for the DMA are:

- 1 mN minimum resolvable force (25 kPa minimum stress for typical films),
- 1 mm minimum displacement (0.017 % minimum strain for typical films),
- 100 Hz closed-loop bandwidth in isotonic mode,
- 1 N maximum force (25 MPa maximum stress for typical films),
- 3 mm maximum displacement (50% maximum strain for typical films).

Samples were actuated in an electrolyte solution of 0.1 M tetraethylammonium hexafluorophosphate in propylene carbonate with 1 % distilled water.

3.1 Effects of Deposition Electrode Materials on Polypyrrole Films

In this section the effects generated by changing the material at the deposition electrode during synthesis were studied. The material properties of the films fabricated underwent notable changes in conductivity, porosity and texture, mechanical strength, and maximum degradation potential. As discussed previously these all have significant influence on the strain rates and stresses achievable by the actuator. In some cases, the increase in strain amplitude was as high as 93%. Polypyrrole films were synthesized on the following electrode materials: glassy carbon, gold, nickel, platinum, and stainless steel. The resulting actuators were then characterized for mechanical and electrical properties.

3.1.1 Fabrication Methods

Films were grown in a solution of 0.05 M distilled pyrrole monomer and 0.05 M tetraethylammonium hexafluorophosphate in propylene carbonate with 1% distilled water. The film was synthesized galvanostatically at -20 °C at current densities of 1.25 $A \cdot m^{-2}$.

Deposition chambers were constructed for performing film synthesis of several materials simultaneously. Depositions of flat films were made on gold, nickel, and platinum thin metal foils except for the glassy carbon films which were grown on a small section of a plate. Table 3-2 summarizes the material specifications of the metals used for flat films.

Table 3-2. The list of specifications for the metals used for flat films; selection was based on purity.

Sample	Gold	Nickel	Platinum
Thickness (mm)	0.0254	0.0254	0.0254
Purity (%)	99.95	99.99	99.9

A square chamber was constructed in Delrin ® to hold four sample materials at a time and act as a vessel for the deposition solution. Figure 3-1 shows the configuration of the plates that provided evenly spaced windows between the deposition materials and electrodes. These window plates were used to position the foils as well as to provide a compressive electrical contact with the working electrode. A sheet of stainless steel was used as the counter electrode and mounted using Kapton © tape on the surface 28 mm from the working electrode materials. The samples were all cut and taped into the windows such that a 25 mm^2 surface area was exposed. There is a separate window covering for the glassy carbon plate because of its greater thickness.
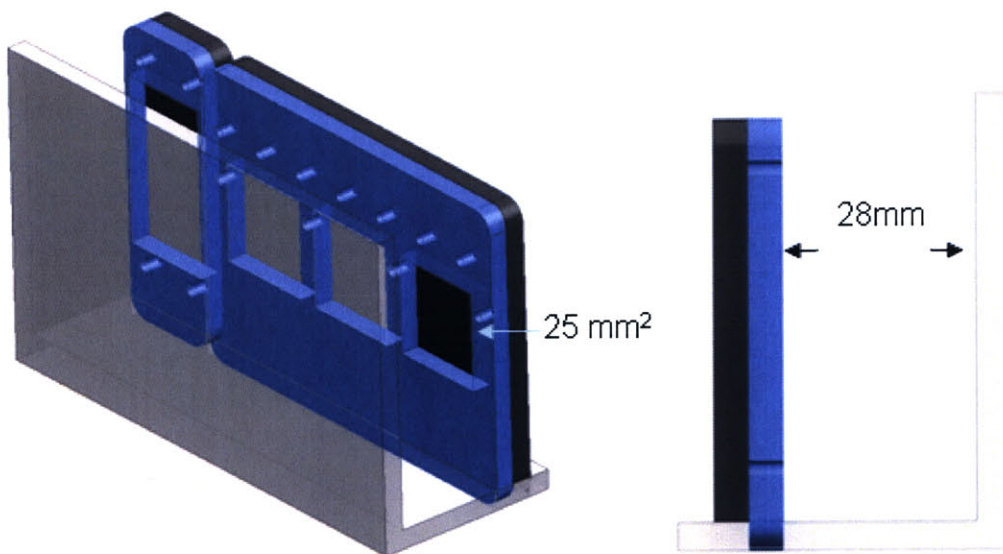

Figure 3-1. A deposition chamber was constructed to provide a constant distance of 28 mm between the working and counter electrode materials during flat film syntheses.

Working electrode materials were polished with 1500 grit (60 particles/mm) sandpaper in between depositions in order to remove any small particles of polypyrrole. They were then cleaned with acetone. Table 3-3 provides a list of dimensions of the samples that were used for the active property testing performed in this chapter. Films were taken from two separate deposition batches. Each batch is denoted by the sample name.

Table 3-3. The following is a summary of the flat film dimensions for the samples that were used for testing. Films were taken from two separate each of which is denoted by name.

Material	Sample name	Film Length (mm)	Film Width (mm)	Film Thickness (μm)
Gold	AuN3	10	5	50
Glassy Carbon	GCM10	10	7	40
	GCN3	10.25	5	52
Platinum	PtN3	8.75	5	65
Nickel	NiN3	10	7	40

The deposition electrode materials used differed slightly for the tubular films. Glassy carbon, nickel, and platinum were still used but the gold material was substituted for stainless steel. Films deposited on gold have a tendency to be difficult to remove from the deposition electrode as the polymer seems to almost bond with the metal, while the opposite is true for stainless steel. Because stainless steel does not bond as well to the polymer during synthesis it was a better choice for this process. Removal of films without damaging them was an issue when synthesizing tubular films unlike during the fabrication of the flat films. This is because peeling the polymer from a flat foil.introduces far less friction than inching a tube off of a 200 mm long, 1 mm diameter rod. Table 3-4 lists the purity and dimensions of the materials that were used for tubular film synthesis.

Table 3-4. A list of materials and properties used for tubular film synthesis; selection was based on purity.

Sample	Nickel	Platinum	Stainless Steel
Diameter (mm)	1	1	1
Purity (%)	99.98	99.95	Fe:Cr:Ni;70:19:11

The deposition chamber for tubular films was simply a 500 mL graduated cylinder with a columnal insert which held samples upright in the container in the configuration shown in Figure 3-2. Samples were generally grown three at a time (Figure 3-2 (a and b)) with a stainless steel counter electrode which hugged the walls of the cylinder. Depositions were formed on the metal rod core and then slid or inched off once synthesis was completed (Figure 3-2 (c)). Because of the length of the column, and the different material properties of the metals, the deposition electrode rods would sometimes have a tendency to bow creating an uneven electric field between the working electrode and counter electrode in the rim of the cylinder. There were no visible differences generated from this error, but it should be mentioned that the spatial control in this set up was not as effective as it was for the flat films.
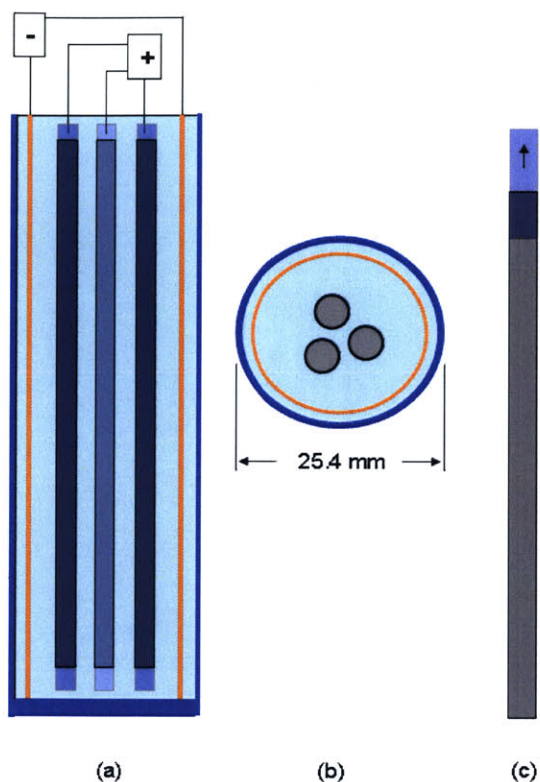
(a)   (b)   (c)

Figure 3-2. The deposition chamber used for tubular film synthesis; three samples were loaded at a time (a) with a steel counter electrode that fit snugly against the perimeter of the column, the rods were packed at evenly spaced intervals in the center of the cylinder (b), once deposition was complete the core material was removed (c).

Table 3-5 provides a list of the materials that were used for testing. Samples were taken from three different depositions. As with the flat films, the working electrode materials were polished with 1500 grit sandpaper in between syntheses. They were then wiped clean with acetone.

Table 3-5. The materials used for testing of tubular films were taken from three separate deposition batches. Each batch is denoted by the sample name.

Material	Sample name	Film Length (mm)	Film Cross-sectional area $(10^{-6}\,m^2)$	Film Thickness (μm)
Glassy carbon	GCM18	8.1	0.157	55
Platinum	PtM31	11.55	0.126	40
	Pt1	14.1	0.142	45
Nickel	NiM31	11	0.113	36
	Ni1	9.5	0.026	8.3
Stainless steel	SSM31	8.5	0.141	45
	SS1	9.95	0.173	55

3.1.2 Testing

Films were tested for differences in their active and passive properties. The dynamic tests were performed on the DMA using the resistance compensation waveform developed by Madden et al., where a 4 V amplitude signal was pulsed through the film for 1 ms. Active strains, charge injection, and maximum voltages were measured for the samples at various frequencies and stresses. Figure 3-3 shows the results of a typical test. Strain and charge amplitudes reported were averaged over the 10 cycles of each isotonic test. The following passive properties were measured directly: 1) Conductivity, 2) Density, and 3) Young's modulus. A scanning electron microscope was used to view surface characteristics under magnification. Features of interest generally included porosity and surface roughness or texture.
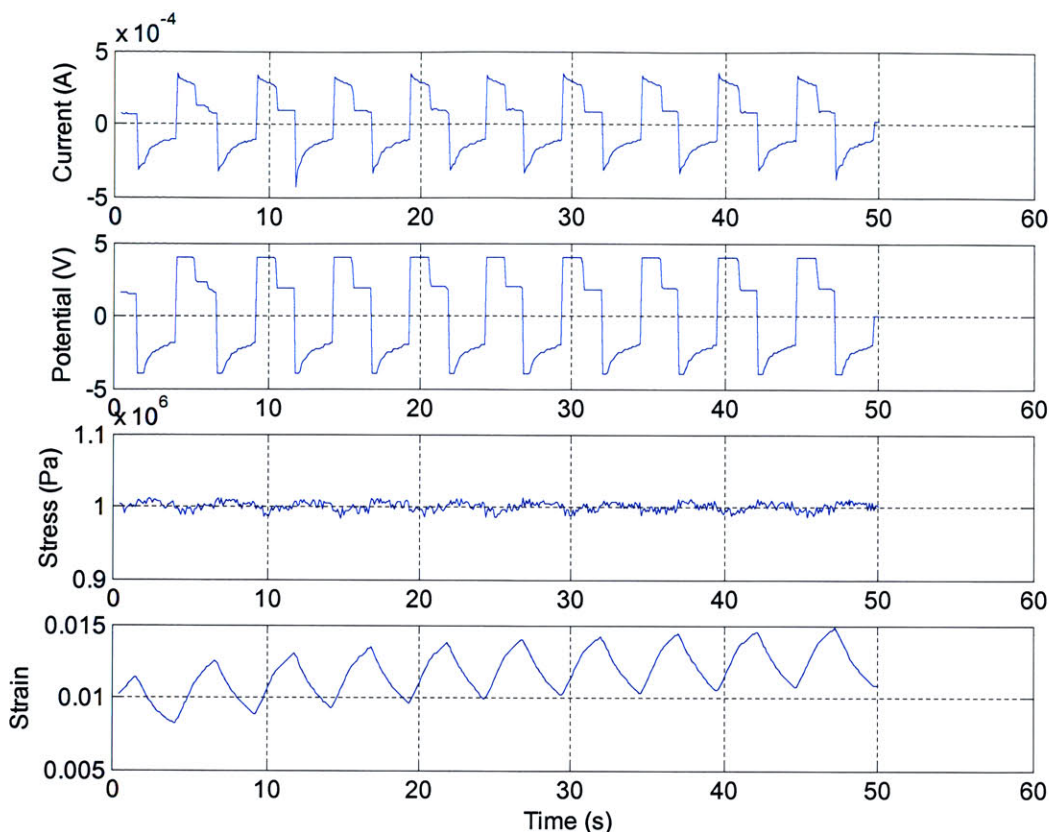
Figure 3-3. Typical test results shown for a sample synthesized on nickel driven with a ±0.8 V versus Ag/AgClO₄ at 0.25 Hz signal isotonically at 1 MPa for 10 cycles.

3.1.3 Results

3.1.3.1 Active Properties

The results of active testing of the flat films grown on gold, glassy carbon, nickel, and platinum were difficult to assess at the lower excitation voltages. In Figure 3-4 the four actuators' average strain results are shown under an applied potential of ±0.8 V versus Ag/AgClO₄ and a frequency of 0.25 Hz. The only consistent correlation between deposition material and performance is the lower strains exhibited by the actuator grown on a nickel working electrode. This trend continues in Figure 3-5 while another seems to become apparent; the actuators begin to differentiate in their performance characteristics at the increased voltage applied of ±1.2 V versus Ag/AgClO₄. The actuators synthesized on platinum foil generated consistently higher strains at each isotonic test. The

performance of platinum films is followed by gold and nickel in that order. The film grown on the platinum foil showed an average increase in performance of 0.17 % strain or a 15 % increase overall over the next best actuator. The results for glassy carbon are not shown in Figure 3-5 as the sample failed in the first trial of the ±1.2 V testing cycle. The four samples used for the tests shown in Figure 3-4 and Figure 3-5 were: 1) AuN3, 2) GCN3, 3) NiN3, and 4) PtN3
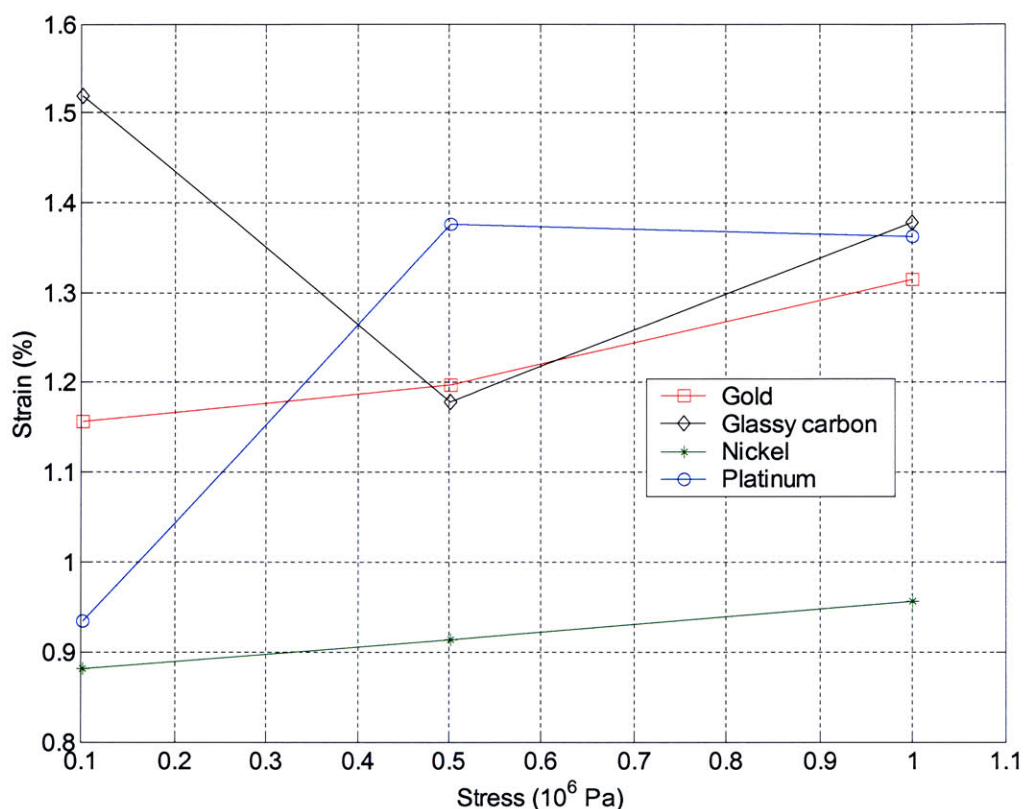

Figure 3-4. Strain versus stress characteristics for flat films tested isotonically at an excitation voltage of ±0.8 V versus Ag/AgClO$_4$ and a frequency of 0.25 Hz show erratic responses between samples at different stresses.
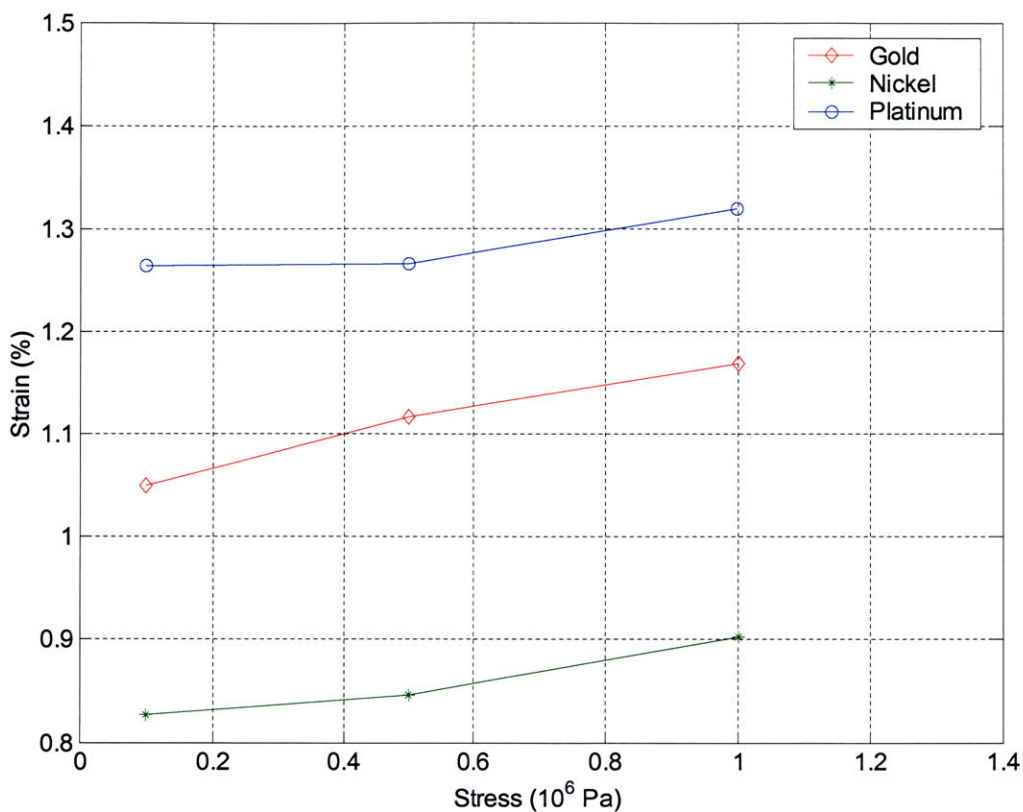
Figure 3-5. Strain versus stress characteristics for flat films tested isotonically at an excitation voltage of ±1.2 V versus Ag/AgClO$_4$ and a frequency of 0.25 Hz consistently show the platinum film as producing the highest strains.

Although a consistent trend is more evident in the films grown with a tubular geometry, it is not exactly the same trend seen with the flat films. The following four samples used for the tests shown in the next three figures (Figure 3-6, Figure 3-7, and Figure 3-8): 1) GCM18, 2) NiM31, 3) PtM31, and 4) SSM31. Almost immediately evident in Figure 3-6 for films being tested with ± 0.8 V versus Ag/AgClO$_4$ and a frequency of 0.25 is the equal, if not greater, strains demonstrated by the films grown on the nickel deposition electrode over all the others in the group. While the increased performance is not striking amongst the top three films (nickel, platinum, and stainless steel) it is a far more uniform result than that seen in Figure 3-4 with flat films at the same excitation potential.
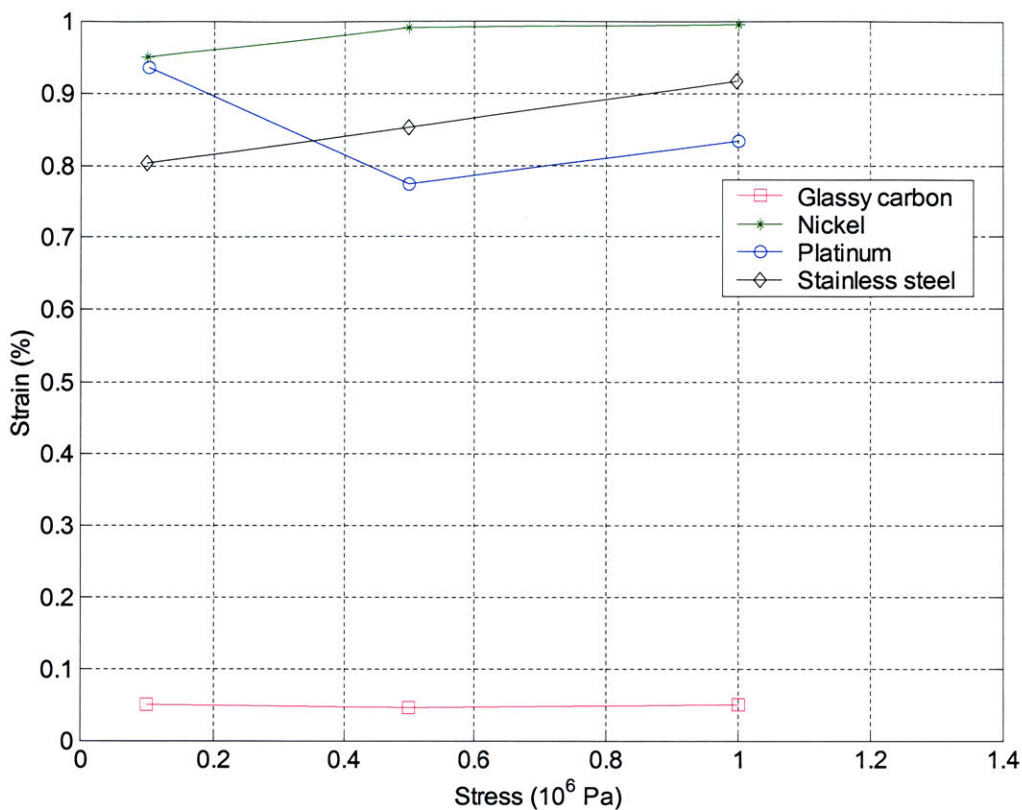
Figure 3-6. Strain versus stress characteristics for tubular films tested isotonically at an excitation voltage of ±0.8 V versus Ag/AgClO₄ and a frequency of 0.25 Hz exhibit large strains for the nickel, platinum, and stainless steel actuators.

In the results shown for an excitation voltage of ±1.2 V versus Ag/AgClO₄ and a frequency of 0.25 Hz, the increase in differentiation between the nickel deposited film continues. The actuator shown an increase in strain amplitudes produced by as much as 53% over the next best films. The stainless steel and platinum films continue to produce similar results in this set of tests. One more increase in actuation properties is exhibited in Figure 3-8. While the nickel film continued to show a 67% increase in strain output over the next best group of actuators it also demonstrated higher load capacity. This increase in load bearing capacity was also seen in the actuator synthesized on platinum.
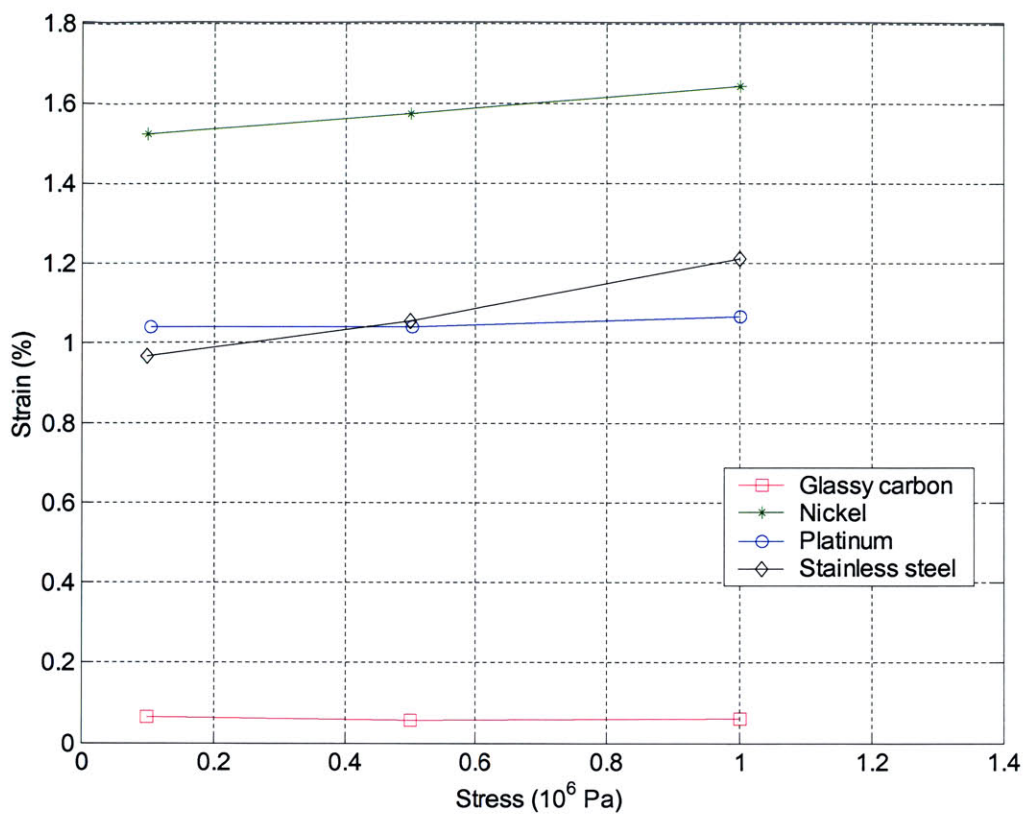
Figure 3-7. Strain versus stress characteristics for tubular films tested isotonically at an excitation voltage of ±1.2 V versus Ag/AgClO$_4$ and a frequency of 0.25 Hz exhibit noticeably larger strains for the nickel than the platinum and stainless steel actuators.
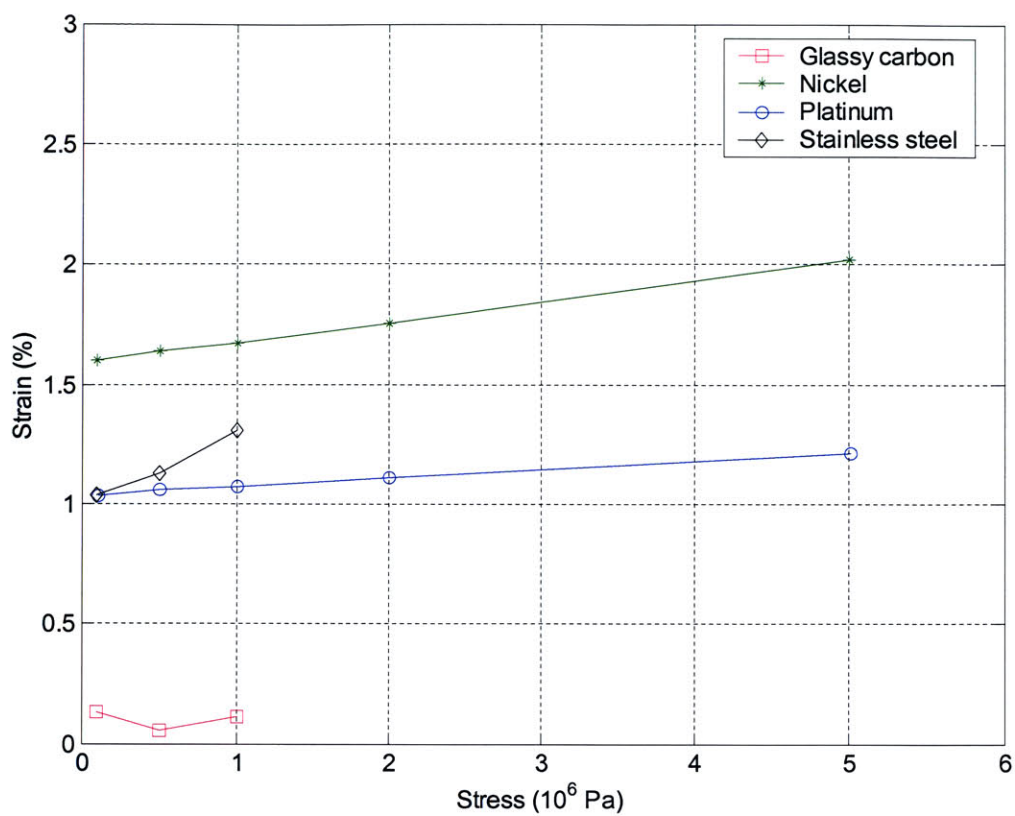
Figure 3-8. Strain versus stress characteristics for tubular films tested isotonically at an excitation voltage of ±2.5 V versus Ag/AgClO$_4$ and a frequency of 0.25 Hz continue to exhibit larger strains for nickel than the platinum and stainless steel actuators.

Another batch of samples were tested independently to check if the films synthesized on the different metal rods continued to show the same differences in strain amplitude. The following three samples were used for a test performed at ±0.8 V versus Ag/AgClO$_4$ and a frequency of 0.1 Hz: 1) Ni1, 2) Pt1, and 3) SS1. The film grown on the nickel rod still outperforms the platinum grown actuator by 90 to 126 % and the stainless steel actuator by 195 to 300 %.
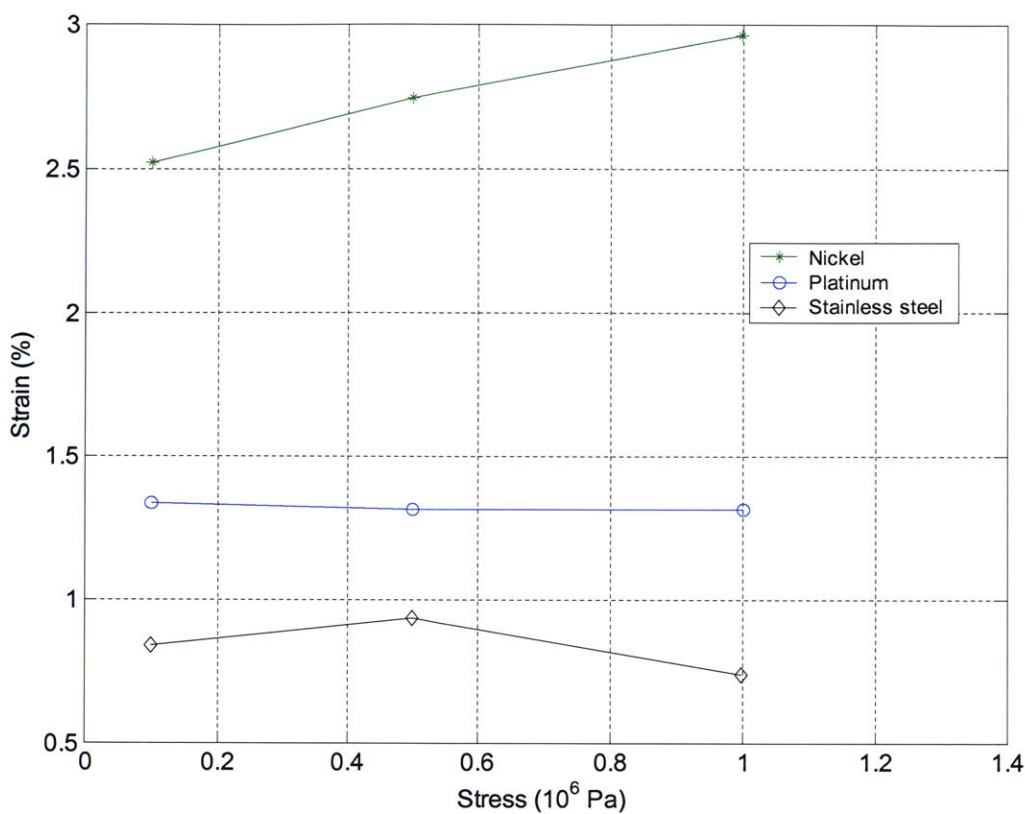
Figure 3-9. Strain versus stress characteristics for tubular films tested isotonically at an excitation voltage of ±0.8 V versus Ag/AgClO$_4$ and a frequency of 0.1 Hz continue to exhibit larger strains for nickel than the platinum and stainless steel actuators.

While some of the behavior characteristics appear consistent there are some intriguing differences in the performance of the films. The first noticeable difference was in the two batches of films deposited on stainless steel and platinum. In Figures 3-6 through Figures 3-8 they did not exhibit the same performance difference as they do in Figure 3-9. The difference in performance between these two films was in the same range but, where the film grown on stainless steel had been the better of the two in the previous tests, in this test they switched. This raises an important point question in the variability between batches. In Figure 3-10 two separately grown films on the nickel tubes were compared. Each of the samples was tested at ±0.8 V versus Ag/AgClO$_4$ and ±1.2 V versus Ag/AgClO$_4$ at 0.25 Hz. The maximum difference in strain output between the two films was 48 %. This is a significant variability in performance.
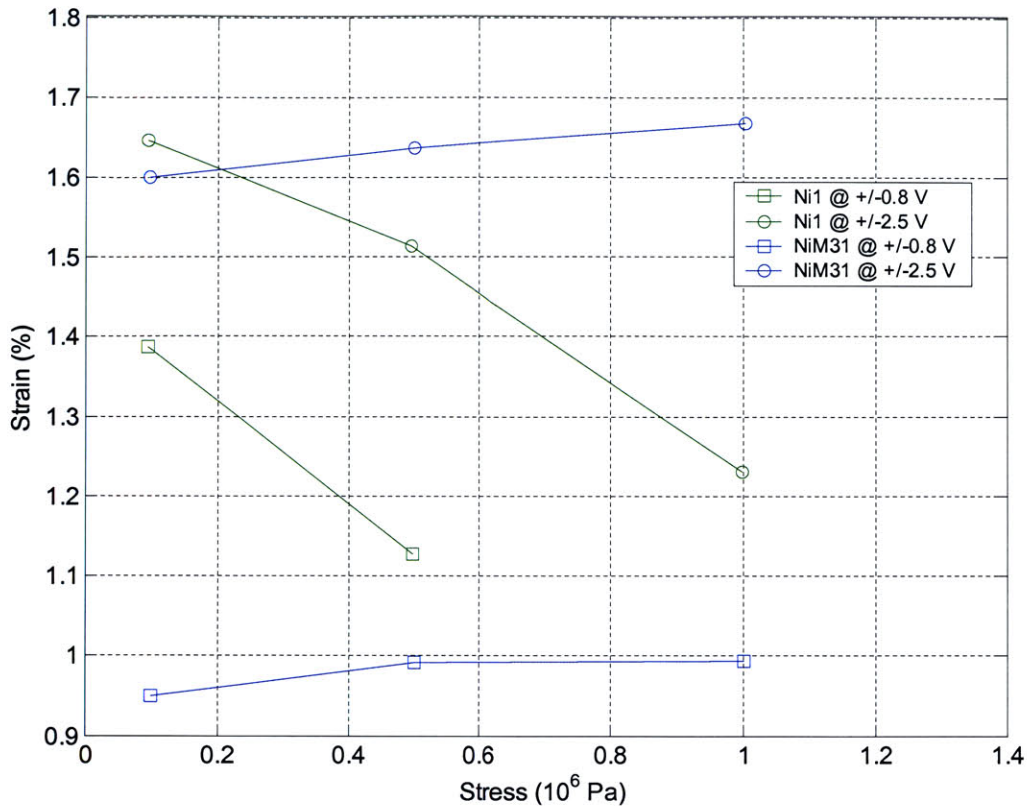
Figure 3-10. Variability between batches synthesized on the same material show a difference in strain output by as much as 48%. The films were all grown on nickel tubes and tested with excitation voltages of ±0.8 V versus Ag/AgClO₄ and ±1.2 V versus Ag/AgClO₄ at 0.25 Hz

Another important set of differences in the behavior of the films is seen in the flat films versus the tubular films. While the previous results show that in both cases the actuators differentiate themselves in performance at higher voltages, there was no direct correlation between the type of metal the films were deposited on and their performance as an actuator. Figure 3-11 compares the results of the isotonic tests performed on all of the tubular and flat films at ±0.8 V versus Ag/AgClO₄ at 0.25 Hz. At this applied potential there is no "best" actuator. Three of the flat films (grown on platinum, gold, and glassy carbon) yield an almost identical result under a load of 1 MPa.
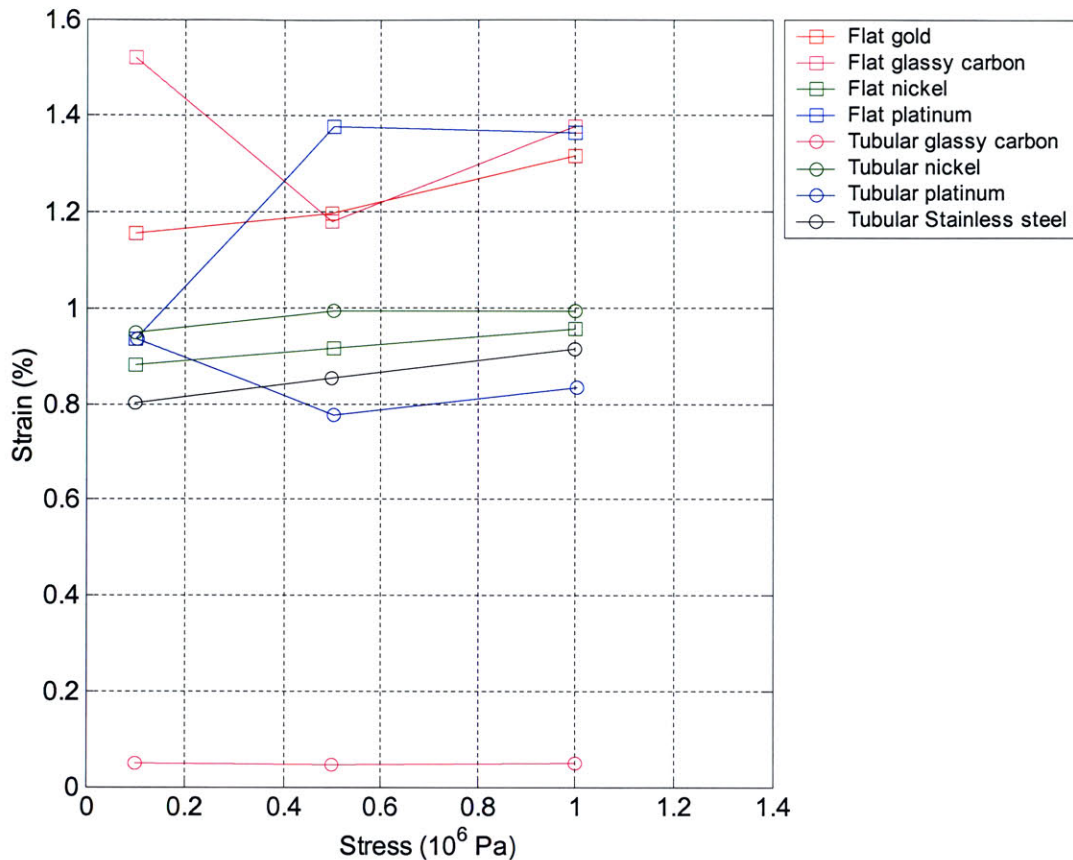
Figure 3-11. Flat and tubular films were compared for their strain properties at ±0.8 V versus Ag/AgClO₄ and 0.25 Hz. The flat films were generally better except in the case of the sample deposited on nickel.

The difference in performance between actuators increases in Figure 3-12. The tubular film grown on nickel once again yields the largest strains over the next best actuator by as much as 28%, but when grown on a flat plate produces the lowest strains of the group. Although the maximum reported strain rates are 3 to 3.4 %/s the average strain rates are typically much less (Dinga, 2003; Madden, et al., 2000). Because the time scale of actuation measured for pectoral fin swimming is on the order of 0.5 to 2 Hz, the average strain rates are a more important figure of merit for this application. The highest average strain rates were exhibited by the films grown on nickel; rates were as high as 1 to 2 %/s at ±2.5 V at 0.25 Hz and 5 MPa. These are not particularly fast actuators but at thicknesses of 30 to 50 μm they were not grown for optimized speed. Faster actuation can be achieved as films are grown thinner.
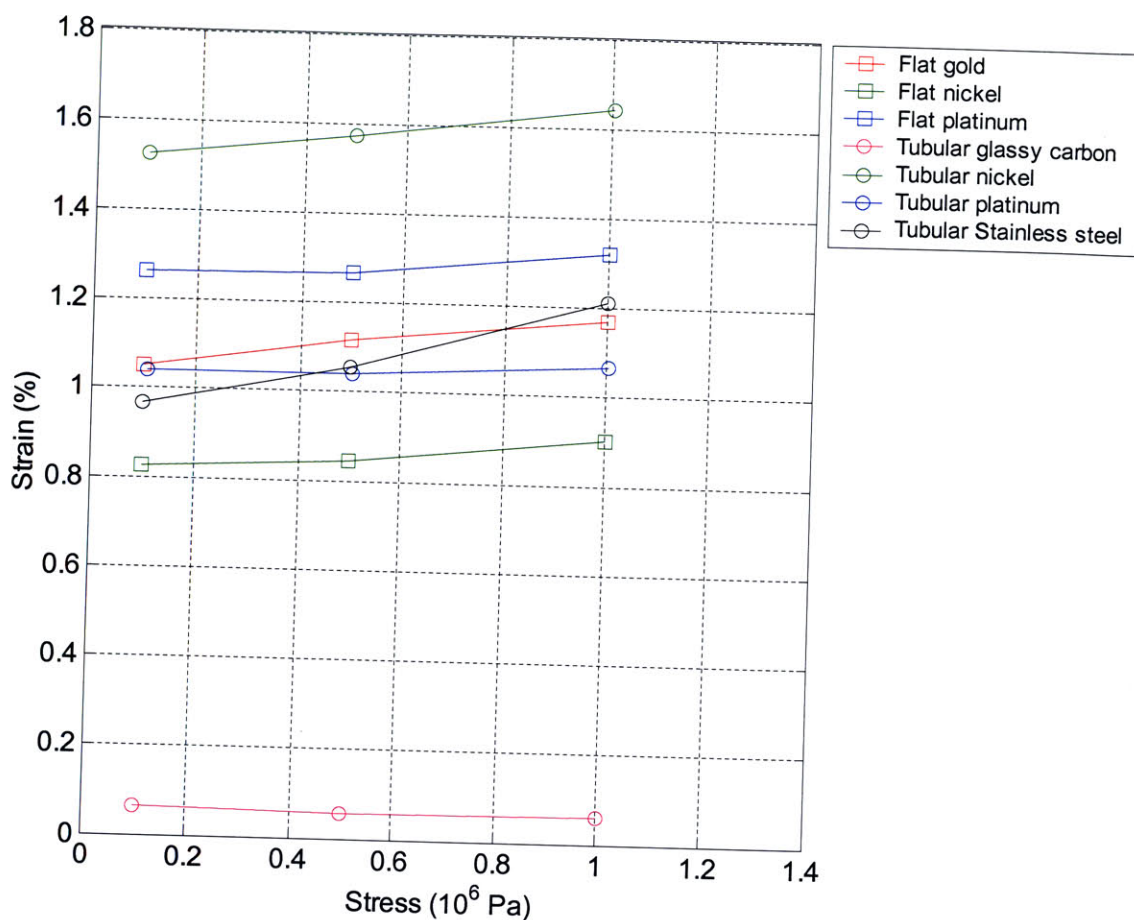
Figure 3-12. Flat and tubular films were compared for their strain properties at ±1.2 V versus Ag/AgClO₄ and 0.25 Hz. The flat films are fairly clustered in their performance while the tubular films show a widening range of strain amplitudes.

Table 3-6 lists a summary of the highest strains achieved by each of the actuators in Figures 3-11 and 3-12. Tests were performed at ±0.8 V and ±1.2 V versus Ag/AgClO₄ at stresses up to 1 MPa and a frequency of 0.25 Hz.

Table 3-6. A summary of the best actuation mode for each of the actuators shows the maximum average strain achieved at the given applied potential and stress.

Deposition Electrode Material	Glassy Carbon Rod	Nickel Rod	Platinum Rod	Stainless Steel Rod	Glassy Carbon Plate	Gold Foil	Nickel Foil	Platinum Foil
Strain (%)	0.06	1.64	1.07	1.21	1.38	1.30	0.95	1.38
Applied Peak-to-Peak Voltage (V)	1.2	1.2	1.2	1.2	0.8	0.8	0.8	0.8
Stress (MPa)	1	1	1	1	1	1	1	0.5

Interestingly, the flat films all yielded their highest strains at ± 0.8 V, this is most likely due to reaching an earlier degradation potential on these polypyrrole samples. Figures 3-13 and 3-14 show the voltage versus strain profiles for the tubular films and flat films respectively. The tubular films show an increase in strain output as the potential applied is increased while the opposite trend is evident in the flat films. The tubular nickel film not only yields the highest strains but also exhibits greater resilience to degradation due to the applied voltage than any other actuator.
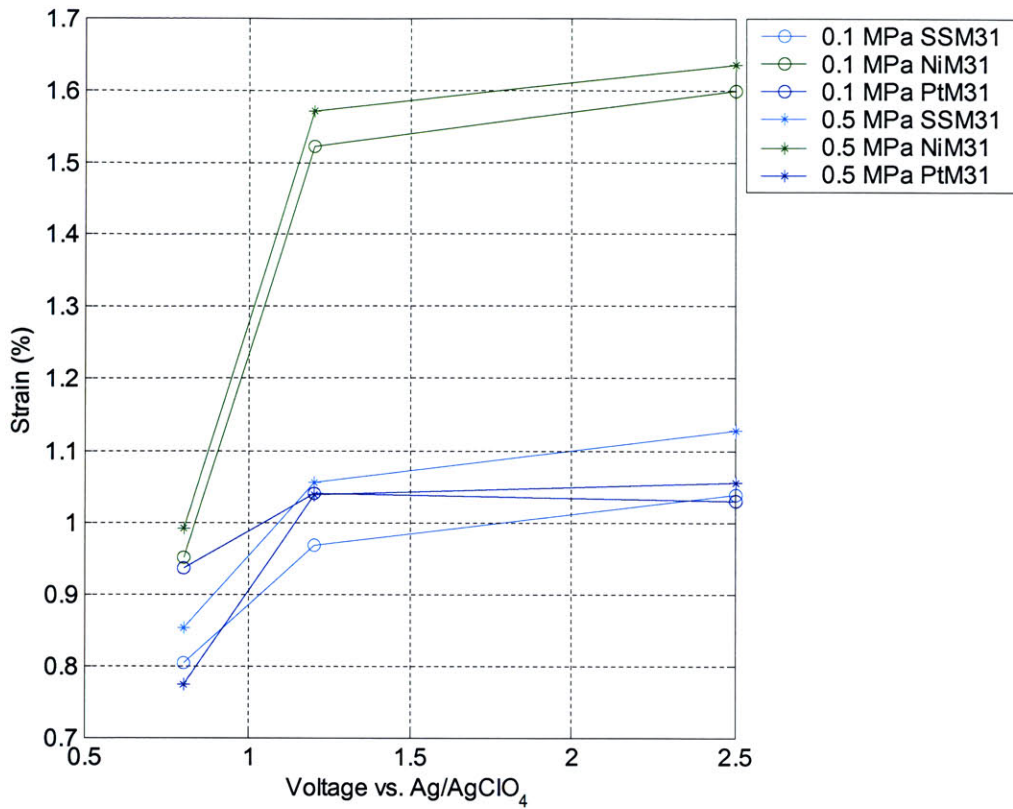
Figure 3-13. Strain versus voltage characteristics for the tubular films shows the film synthesized on nickel to possess the highest strain outputs and increase in strain as the voltage is increased.
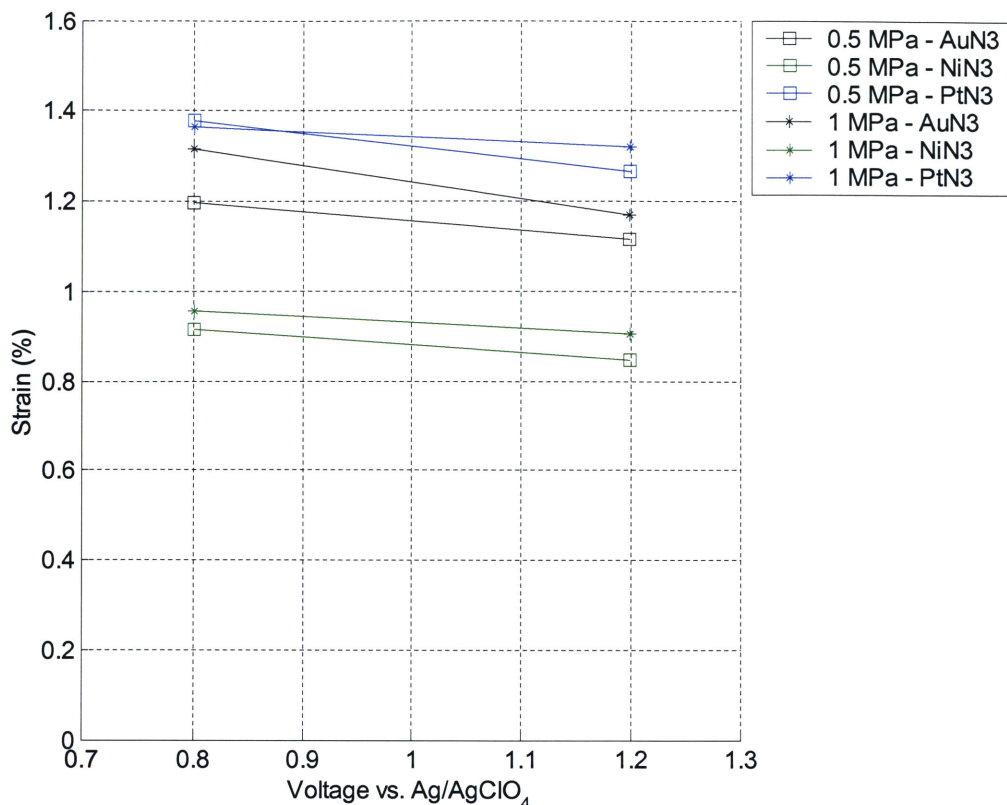
Figure 3-14. The strain versus voltage characteristics for the flat films show a consistent trend decrease in strain output as the voltage increased.

3.1.3.2 Passive Properties

The source of the greater performance of the nickel film grown on the rod as opposed to the flat foil as well as the general variability in these actuators was explored further through investigation of various passive and physical characteristics of the films including. A higher elastic modulus yields leads to an increase in the stress that can be generated per unit charge (see Equation 3-2). Figure 3-15 shows the results of the modulus tests performed on the glassy carbon, nickel, platinum, and stainless steel grown films. The tests were performed by applying a given stress and measuring the strain response; the line connecting the data points indicates the order in which tests were performed. The samples were all dried for one hour in a vacuum oven at 90 °C. Testing was performed in 0.1 M tetraethylammonium hexafluorophosphate in propylene carbonate. Samples were soaked for a minimum of 1.5 hours before attempting modulus tests. The nickel and platinum pyrrole had the greatest consistent modulus. This is

consistent with the active testing results shown in Figure 3-8 where these two films survived tests at much higher stresses while outputting higher strains for the same applied potential
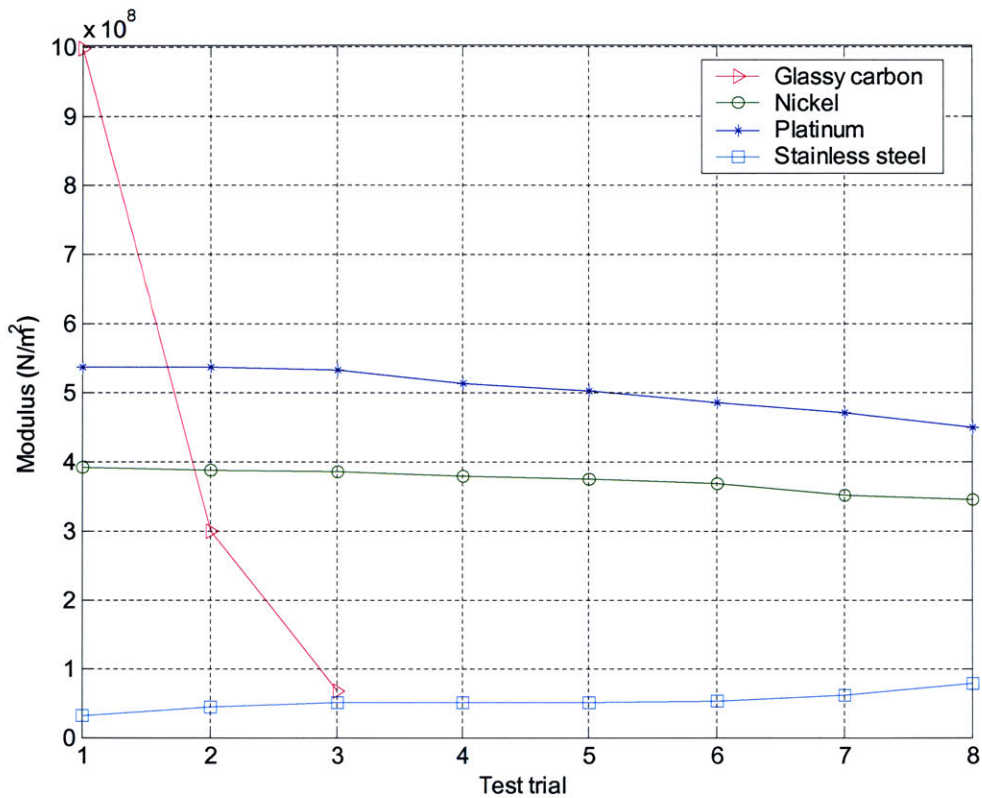

Figure 3-15. The Young's modulus measurements of the tube films were measured in consecutively conducted tests.

Unlike the polypyrrole synthesized on glassy carbon all of the films yielded reasonably consistent results as shown in Table 3-7. The standard deviation on the modulus measurements for the nickel and platinum grown films are less than 10 % of the measured value, the stainless steel grown films show significant variance at 28 %, but the glassy carbon synthesized film yielded over 100 % variance in the measured values. The differences in measurement values in the glassy carbon film may be due to inconsistent clamping pressure on the films causing slipping.

Table 3-7. The mean and variance values are listed below for the Young's Modulus tests that were performed on the DMA.

Material	Nickel	Platinum	Stainless Steal	Glassy Carbon
Mean Modulus $(1.0 \times 10^6$ N·m$^{-2})$	361.5	492	52.0	454
Standard Deviation $(1.0 \times 10^6$ N·m$^{-2})$	17.3	42.3	13.4	483

Table 3-8 lists the conductivities of the films. The highest conductivities of the films synthesized were on gold and glassy carbon. There is a significant jump in values between the nickel and platinum grown films. Correlating these values to their performance as actuators is difficult because the flat platinum polypyrrole was the only actuator that consistently yielded higher strain outputs.

Table 3-8. The conductivity measurements for films synthesized on the deposition materials listed.

Material	Nickel	Platinum	Gold	Glassy Carbon
Conductivity $(S· m^{-1})$	1.2×10^3	1.6×10^3	5.1×10^4	1.7×10^4

Morphologies of Tubular Films

Nickel Rod Electrode

The physical structure of the films was investigated with the use of an SEM. The surface roughness was photographed on the solution side of the film, and texture and porosity on the electrode side of the film. In Figure 3-15 the tubular sample of polypyrrole grown on nickel is shown at various magnifications. The electrolyte side of the film is shown at 34× (Figure 3-15 (A)) and 842× (Figure 3-15 (B)). There are cauliflower-like structures evident in both photographs; these are often seen in films of polypyrrole. Overall, the surface of this film appears quite smooth with the bumps only really becoming evident at

the higher magnification. The size of these features is estimated to be between 10 to 30 µm in diameter. On the inner surface of the film in Figure 3-15 (C), shown at a magnification of 643×, rows of pores are distributed along the length of the tube. The surface is striated with what appear to be two basic sizes of dimples. Some of the pores are larger and roughly 10 µm in diameter while the other set is much smaller and appear to be 0.5 to 1 µm on the average.

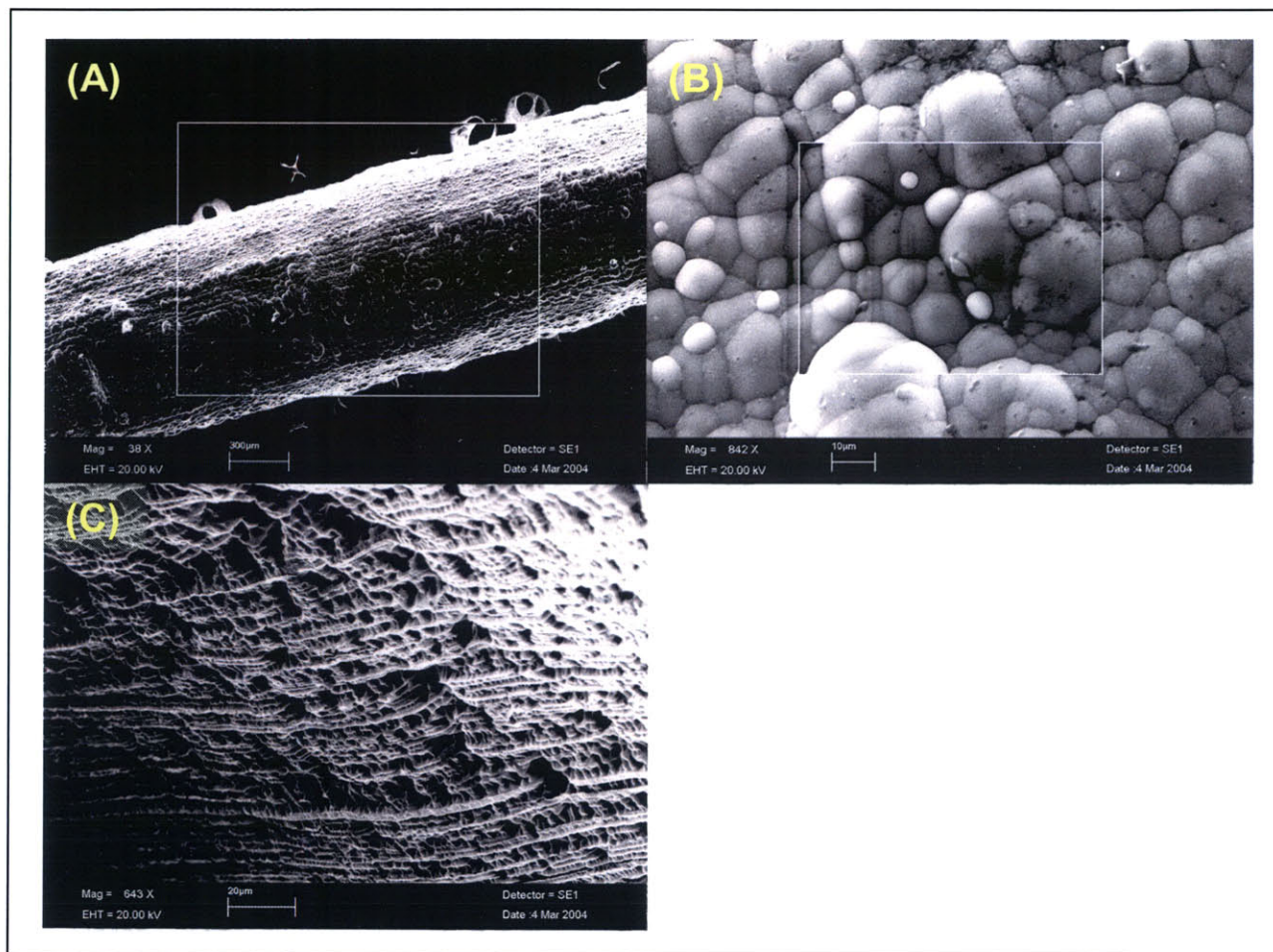Figure 3-15. The photographs on the SEM of the film grown on a nickel rod on (A) the electrolyte surface at a magnification of 34× appears to have a smooth finish. A closer view (B) of the electrolyte side of the film at a magnification of 842× reveals amorphous bumps that are between 10 to 30 µm in diameter. The inner surface of the tube (C), the electrode side, was photographed at a magnification of 643×. This side of the film exhibits a fine porosity.

Platinum Rod Electrode

The film synthesized on the platinum rod, shown in Figure 3-16, is evidently different in morphology from the tube grown on nickel. The images of the electrolyte surface of this sample of polypyrrole show both larger sized and higher density features. Estimating the size of these growths from the magnification at 37× (Figure 3-16 (A)) and 851× (Figure 3-16 (B)), the diameters appear to be 20 to 80 µm in diameter. The inner surface of this polymer tube is also striated along the length of the rod. The photographs, at magnifications of 339× (C) and 1310× (D), reveal pores apparently 15 to 20 µm in diameter. Completely unlike the film synthesized on the nickel rod, the striated ridges are smooth. There only appears to be one scale of surface effects as opposed to the two seen on the nickel tube.
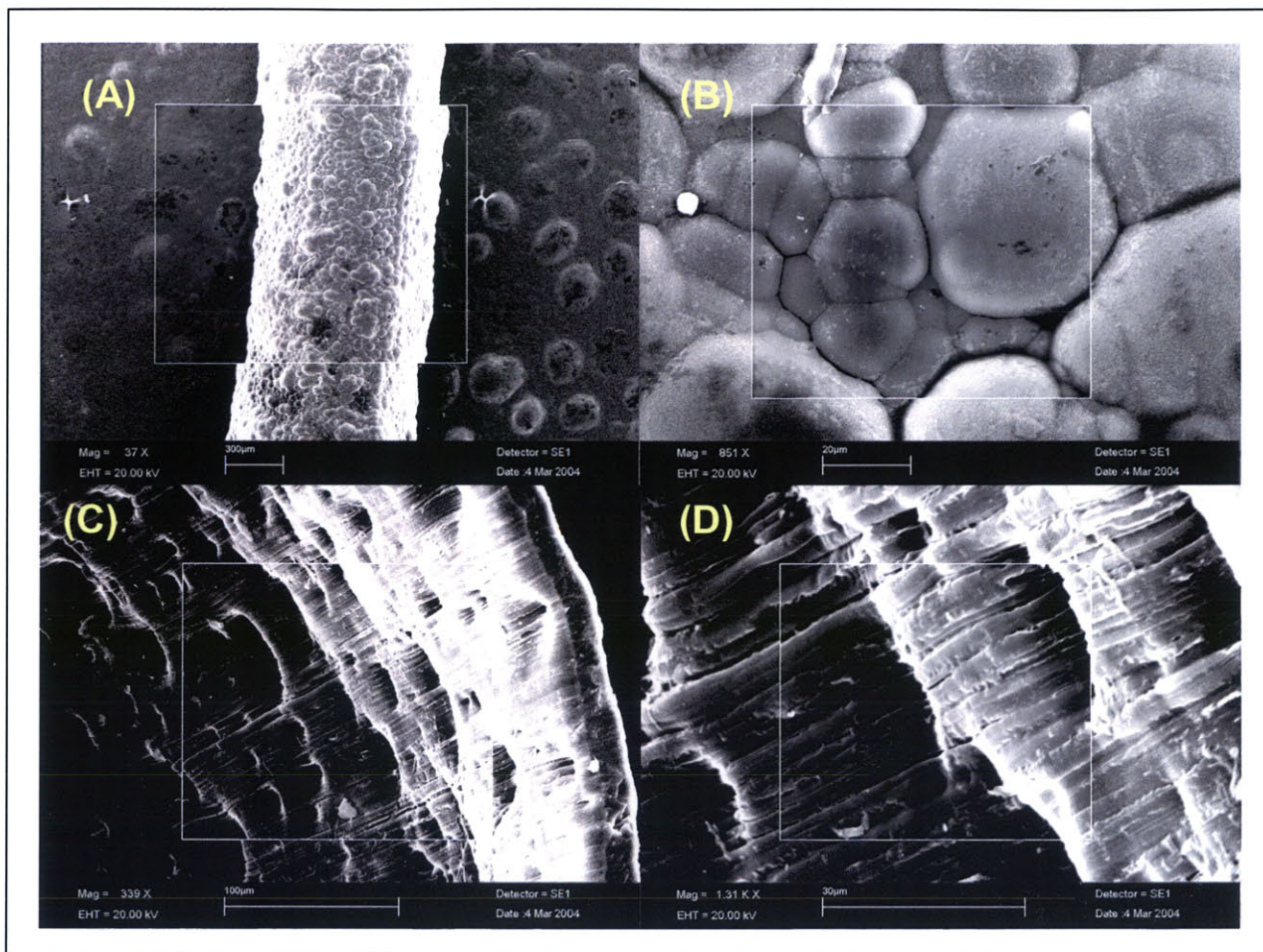
Figure 3-16. This SEM image of the film grown on a platinum rod of (A) the electrolyte surface at a magnification of 37× shows a higher density of greater sized nodules. Between this photograph and the closer view (B) of the electrolyte side of the film at a magnification of 851×, these surface features are estimated to be 20 to 80 μm in diameter. The electrode surface of the tube was photographed at a magnification of 339× (C) and 1310× (D). This side of the film shows porous features that are roughly 15 to 20 μm in diameter.

Stainless Steel Rod Electrode

The features of the tube grown on the stainless steel rod are the most varied in height, formation, and texture. In Figure 3-17 the electrolyte surface of the film shown at a magnification of 37× (A) and 880× (B) the nodules conglomerate and form ridges around the circumference of the tube. The inner surface (C) photographed at a magnification of 735×, exhibit the same striations along the length of the rod as the other two films. The pores on this film are the largest reaching approximately 60 μm in diameter and the

striated ridges are smooth as with the actuator synthesized on platinum. There are many irregularities evident in the picture, but the most unique feature on the electrode face of this film is the broken or torn looking edges.
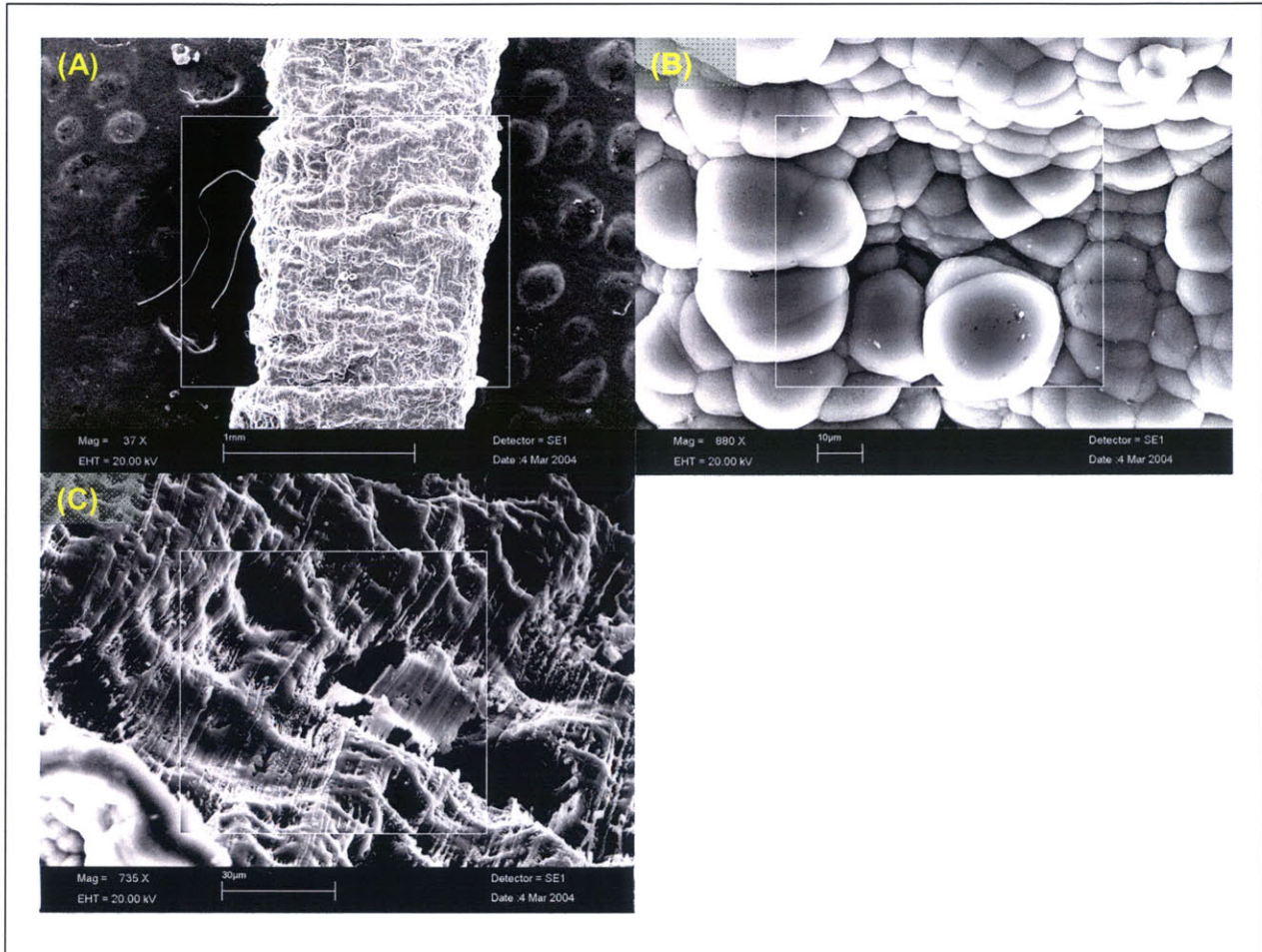

Figure 3-17. This photograph of the electrolyte surface of the film grown on a stainless steel rod at a magnification of 37× (A) shows the most uneven texture of the three films; with conglomerations of nodules forming ridges around the circumference of the tube. In the closer view (B) of the electrolyte side of the film at a magnification of 880× these surface features appear to be approximately 10 to 30 μm in diameter. At a magnification of 735× (C), the electrode surface of the tube is characterized by the same striations as the other two films, pores that are as large as 60 μm in diameter, and even some broken or non-uniform features.

Morphologies of Flat Films

Glassy Carbon Plate Electrode

In the next series of photographs, the flat films are shown. None of these films shows the same striated ridges on the electrode surface. Initially, it was assumed that these features in the tubular films were artifacts from polishing with the 1500 grit sandpaper. However, the flat foils were also treated with the same sanding process and yet do not show the same surface effects. In Figure 3-18 the film grown on the glassy carbon plate, a patterned region of pores close to 1 mm wide is distinctly evident in the magnification of 42× (A). In the closer views, at 144× (Figure 3-18 (B)) and at 1430× (Figure 3-18 (C)), the porous features appear to be roughly 5 to 25 μm in diameter. In the photograph of the opposite face (Figure 3-18 (D)) at a magnification of 143×, the bumpy surface features are on the same order of magnitude and relative dispersion as the pores. Other than the porous and raised bumps, the film is extremely smooth.
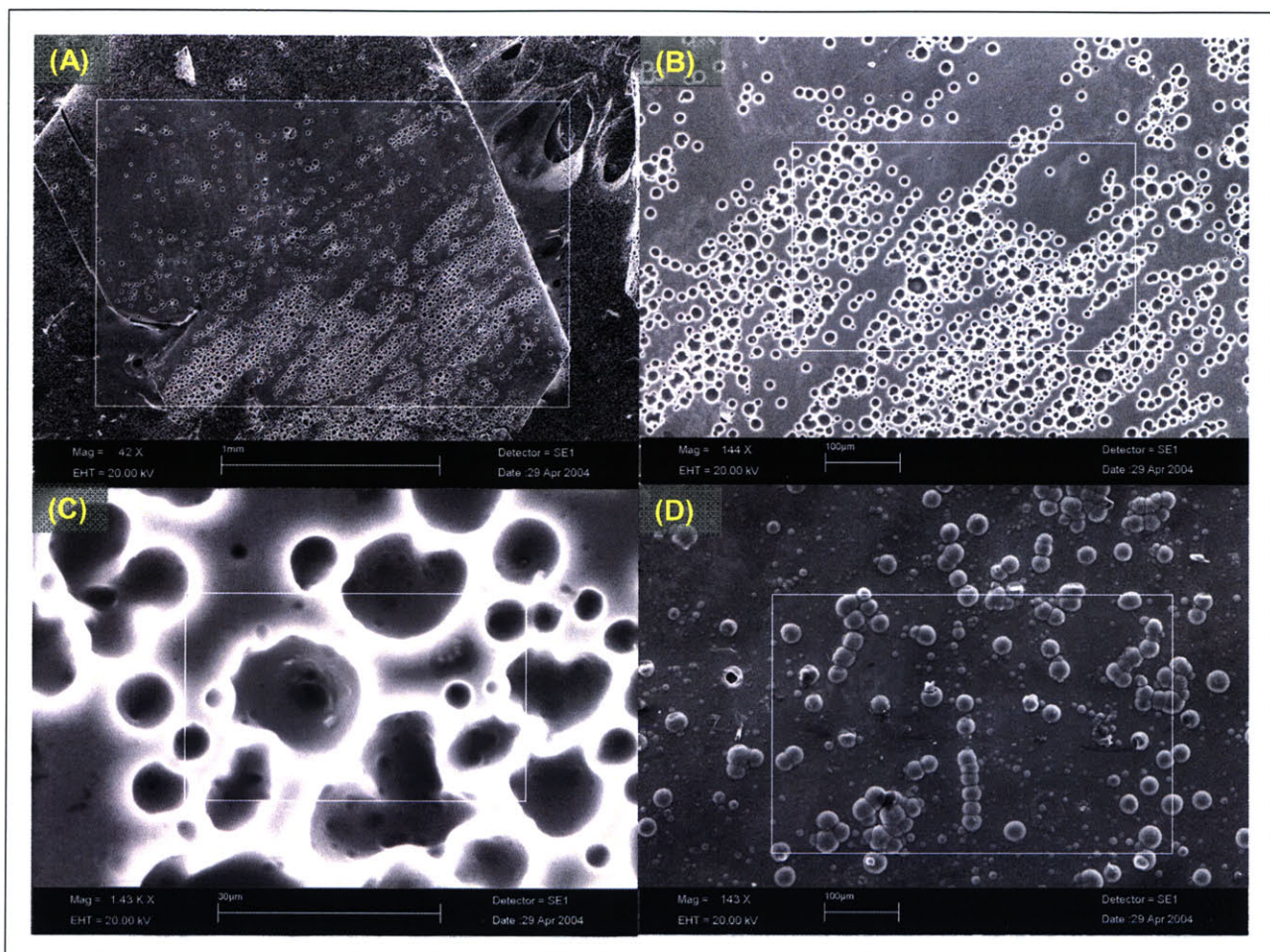
Figure 3-18. This SEM image of the film grown on a glassy carbon plate (A) of the electrode surface at a magnification of 42× shows a patterned region of pores close to 1 mm wide. A closer view (B) at a magnification of 144× and at 1430× (C) reveals these surface features to be roughly 5 to 10 μm in diameter. The electrolyte surface of the film was photographed at a magnification of 143 (D); showing nodules that appear to be the same size as the dimples on the opposite face.

Gold Foil Electrode

The film grown on gold foil also shows patterned regions with and without pores (Figure 3-19) on the electrode surface of the polymer. At a magnification of 62× (Figure 3-19 (A)) the width of the porous regions appear to be roughly 400 μm wide. The closer views at a magnification of 178× (Figure 3-19 (B)) and at 1430× (Figure 3-19 (C)), were used to estimate the diameter of these features which were determined to be close to 5 – to10 μm in diameter. The nodules that are visible in the photograph of the electrolyte

surface at a magnification of 143× appear to be approximately 25 µm, the same size as the dimples on the electrode face of the film as was the case with the glassy carbon plate.
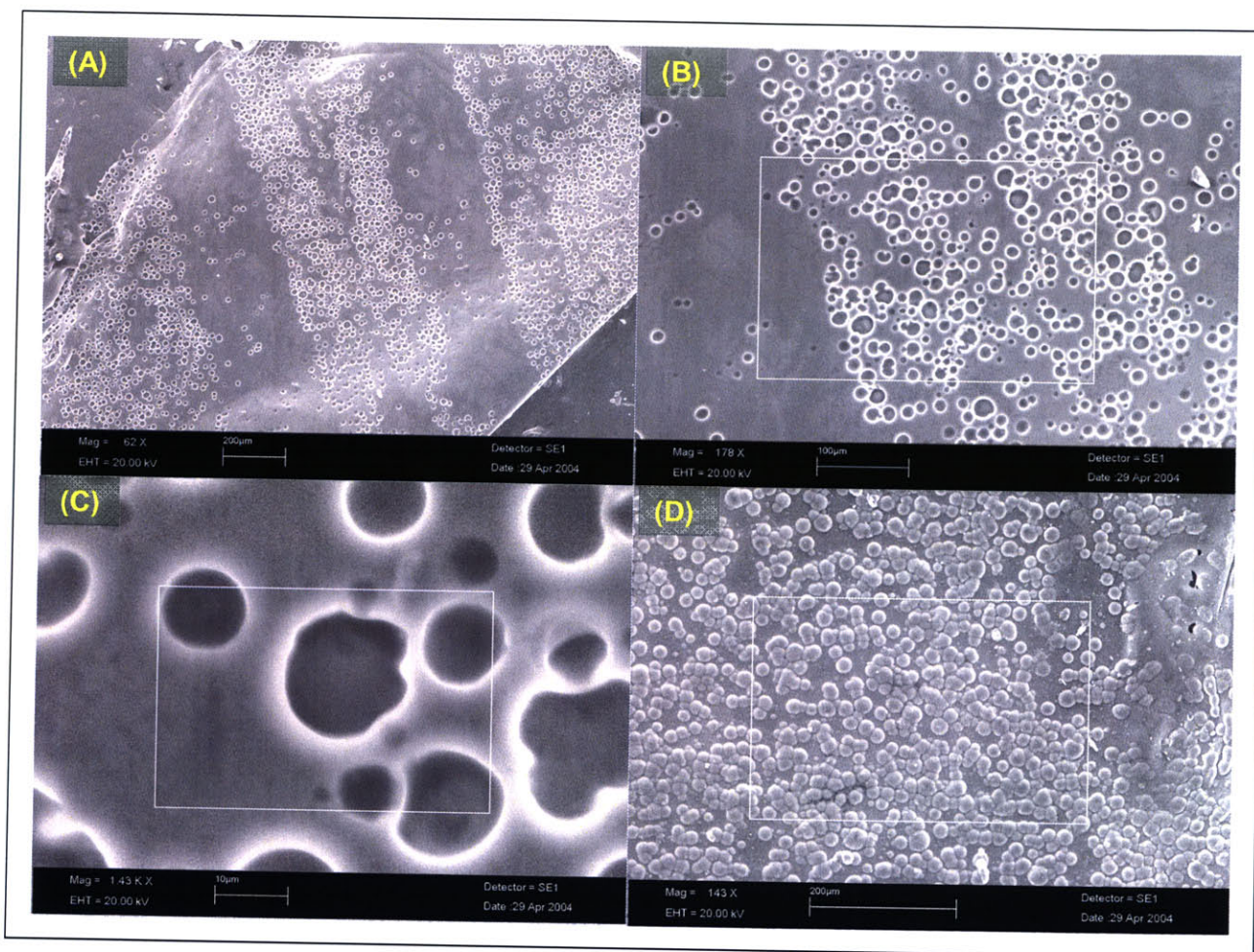

Figure 3-19. In this photograph of the film grown on a gold thin foil of (A) the electrode surface at a magnification of 62× also shows patterned regions with and without pores roughly 400 µm wide. Views at a magnification of 178× (B) and at 1430× (C) shows these features to be close to 5 to 25 µm in diameter. As with the glassy carbon synthesized film, the electrolyte surface of the film showed at a magnification of 143× (D) reveals nodules that appear to be the same size as the dimples on the opposite face.

Nickel Foil Electrode

The features on the film grown on the nickel foil are radically different in texture from the gold and glassy carbon films. The photographs of the electrode surface at magnifications of 135× (Figure 3-20 (A)) and 1430× (Figure 3-20 (B)), show variations from the previous two flat films in textural differences in height, decreased porosity,

wrinkling, and the presence of fine white specks. The electrolyte surface of the film, that was photographed at 177× (Figure 3-20 (C)), shows the same variations in height seen on the bottom surface of the polymer. Unlike the previous two flat films this sample of polypyrrole increased consistency in the presence and size of the small nodules. In a sense, there is both an increase and decrease in the variability of features on this sample.
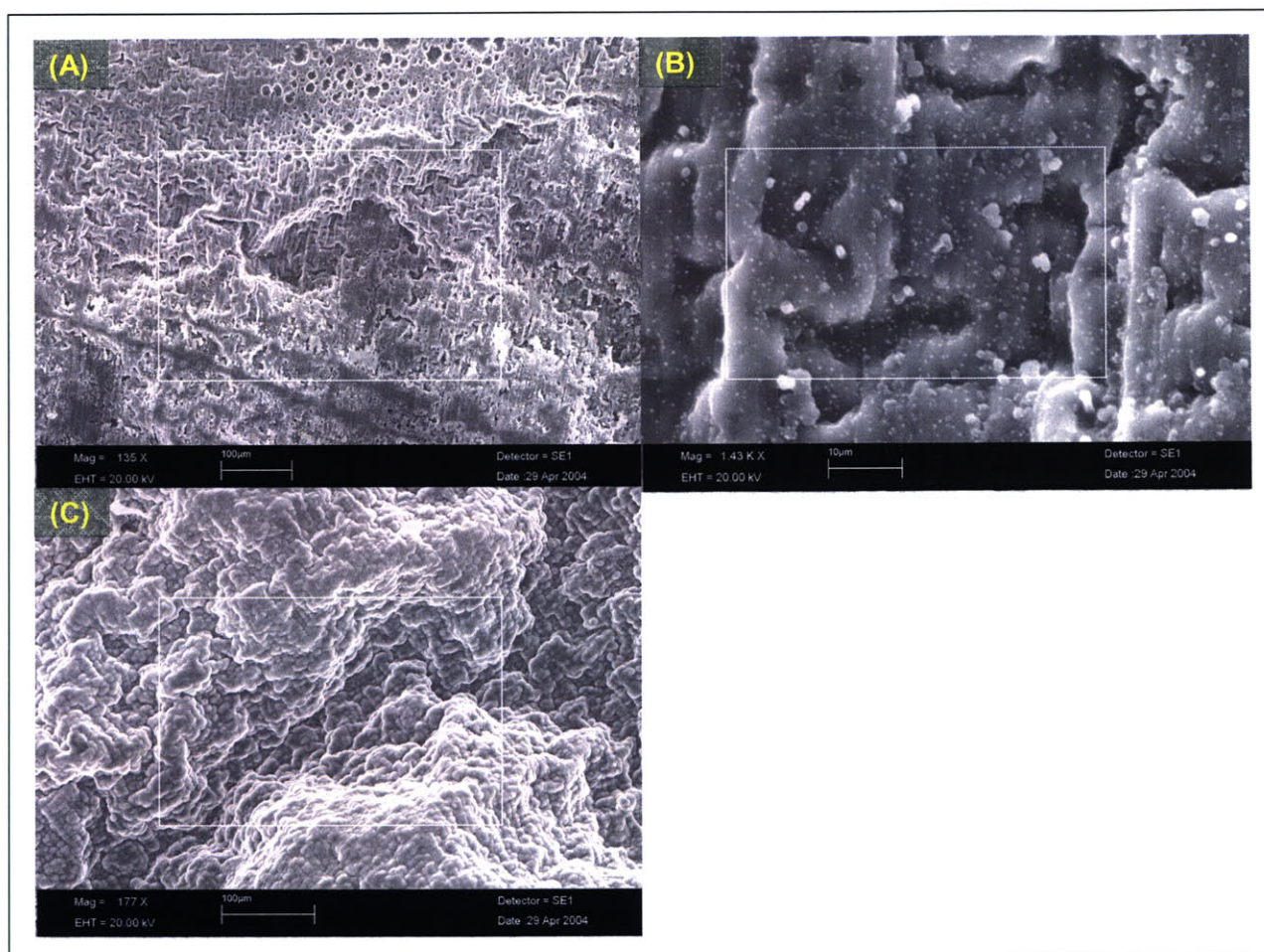
Figure 3-20. The film synthesized on a nickel foil has a radically different texture than the glassy carbon and gold films. The picture of the electrode surface at a magnification of 135× (A) shows variations in height, less porosity, and even wrinkling. A closer view, under a magnification 1430× (B), reveals fine white specks that seem to occur at the same density everywhere in the field of view. The electrolyte surface of the film that was photographed at a magnification of 177× (C) shows the same order of variations in height but appears well ordered in the sense of the size and shape of the nodules.

Platinum Foil Electrode

Finally, the film that was grown on the platinum foil is shown under a magnification of 54× (Figure 3-21 (A)). This sample does not exhibit patterned regions of pores, but is characterized by the even distributions of the 5 to 10 μm features in a well ordered horizontal pattern. In the views at a magnification of 143× (Figure 3-21 (B)) and at 1440× (Figure 3-21 (C)), the dimples appear somewhat irregular in the roundness of their shape, but distribution and size are relatively consistent. The photograph of the electrolyte surface of the film is shown at a magnification of 142× (Figure 3-21 (D)). The cauliflower-like structures are ubiquitous as with the film grown on nickel foil, but appear to be approximately twice as large as the pores on the opposite side of the film.
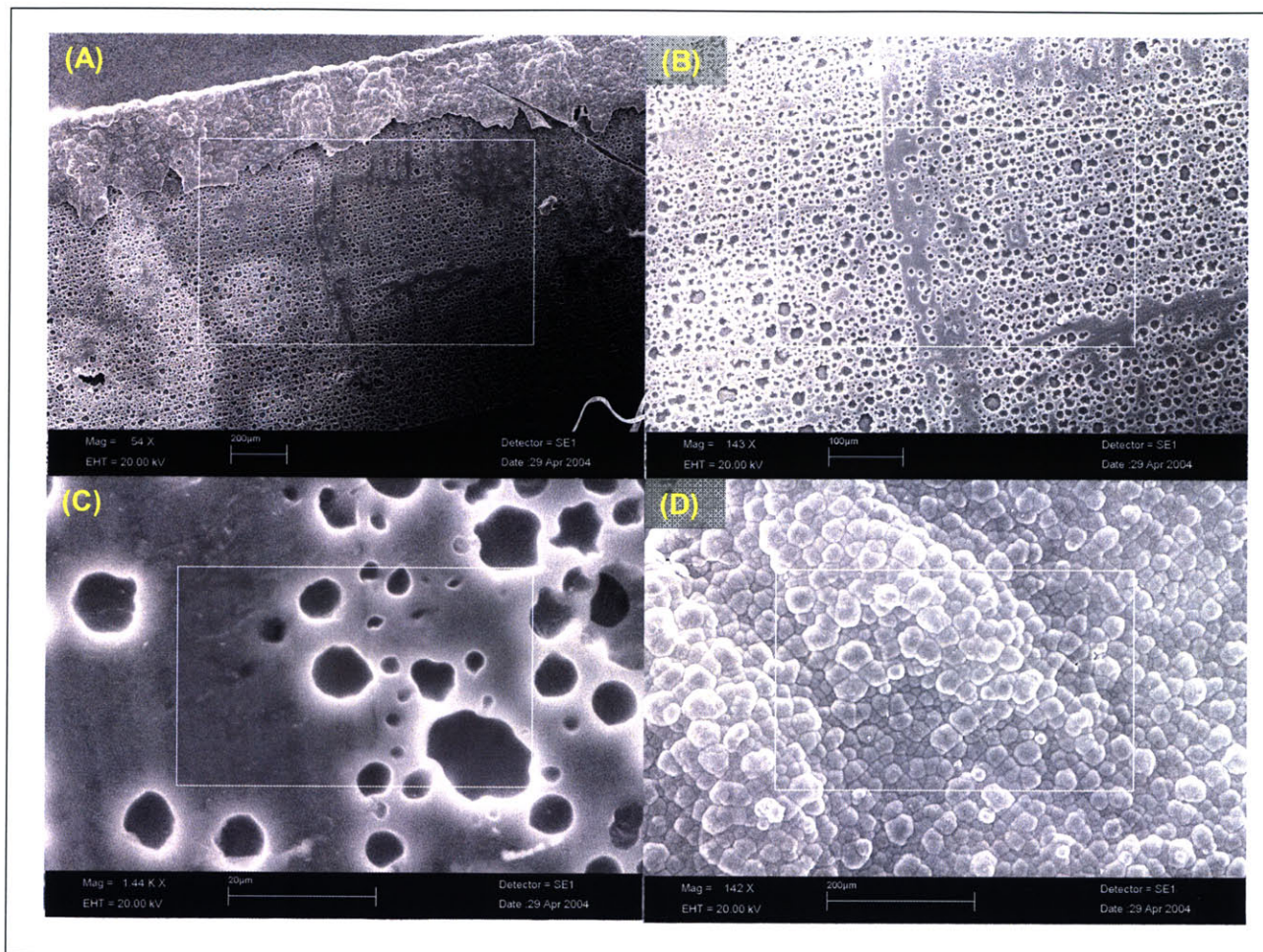
Figure 3-21. This picture of the film grown on a platinum foil is characterized by the evenness of features on its surface. In the view at a magnification of 54× (A) there are no apparent interruptions in the porosity. The dimples are formed in a horizontally striped pattern and in the views at a magnification of 143× (B) and at 1440× (C) would appear to be 5 to 10 µm in diameter. The electrolyte surface of the film showed at a magnification of 142× (D) reveals nodules that appear to be roughly 1.5 to 2× larger than the dimples on the opposite face.

3.1.3.3 Discussion

The most striking correlations between passive properties and active, in the morphological structure of the films was the link between having large numbers of small pores and performance. The two best actuators were the films grown on a nickel tube and a platinum foil. Both of these films exhibit a dramatic difference from the other

films in the regular patterning of fine pores on the electrode surface of the samples. The nickel film exhibited the best performance by an average of 17 % over the platinum film and had pores size approximately 1/5 the size at greater density of dispersal over the electrode surface. The trend continues to correlate with the actuation data as the flat glassy carbon and gold appeared to have the same size pores as the flat platinum film but not as evenly coated over the surface, with completely non-porous regions in both of the films. Both of these actuators consistently output less strain at the higher voltages. One of the least effective actuators was the film synthesized on the nickel foil, similarly this had no porosity at all. While there appears to be no correlation between the material itself and the properties of the films, there does seem to be a direct correlation between actuation properties and morphology. Table 3-8 summarizes the most notable differences in the physical characteristics of the films and compares this with their actuation performance. Morphologically, the film grown on the nickel rod and the platinum foil are closest in pore density and distribution. While in the summary in Table 3-8 the film grown on the glassy carbon plate yielded a slightly higher maximum strain, overall the flat film grown on platinum outperformed this actuator by withstanding higher applied voltages and where it matched and sometimes exceeded the strain output. The root of the morphological changes could be due to material treatments during processing. However, all the actuators underwent the same polishing and cleaning during synthesis so if this is the case it may have to do with material hardness in that the treatment process had differing effects on the electrode surface. Further study is required in order to understand how to control the presence and frequency of pores in conducting polymers and their effect on strain output.

Table 3-8. A comparison of the morphological properties of the films grown on different electrode materials with their performance as actuators (the maximum strains listed are for trials performed at 0.25 Hz).

Deposition Electrode Material	Nickel Rod	Platinum Rod	Stainless Steel Rod	Glassy Carbon Plate	Gold Foil	Nickel Foil	Platinum Foil
Pore Size (μm)	0.5 to 1	15 to 20	5 to 60	5 to 25	5 to 25	20 to 50	5 to 10
Pore Density Distribution (Average distance between features)	Even rows (1 to 2 μm)	Even rows (20 to 30 μm)	Uneven rows (3 to 30 μm)	Patterned regions 1 mm wide (5 to 25 μm)	Patterned regions 400 μm wide (5 to 25 μm)	No pattern (20 to 500 or more μm)	Even rows (5 to 50 μm)
Electrolyte Surface Nodules (μm)	10 to 30	20 to 80	10 to 30	25	25	N/A	25 to 35
Maximum Average Strain (%)	2.02	1.2	1.3	1.5	1.3	0.95	1.4
Voltage at Maximum Strain (V)	±2.5	±2.5	±2.5	±0.8	±0.8	±0.8	±0.8
Stress at Maximum Strain (MPa)	5	5	1	0.1	1	1	1

3.2 Embedded Wire Inserts

In one technique developed at the University of Wollongong by Spinks et al. (Dinga, 2003), increasing the charge injection into the film is improved through integration of fine metal wires during synthesis. Essentially their approach involved depositing a film onto a platinum rod which had been wrapped in a helical winding pattern with a very small gold diameter wire. Once removed from the cylinder on which it was deposited the resulting film is a hollow tube with a helically embedded conductive strip along its

length. Active tests were performed with these films using the resistance compensation technique developed by Madden et al., (Madden, et al., 2000). The peak strains reported by Spinks et al. were on the order of 0.5 % at 1Hz and strain rates as high as 3.4 %/s. Typical strains of 1% were measured isotonically at stresses as high as 8 MPa for actuation at 2.5 V peak-to-peak. These values exceeded the performance characteristics reported by Madden etal. for plain flat films using the resistance compensation wave form (Dinga, 2003; Madden, et al., 2000).

Incorporating wires a helically wound structure into the film improves actuation in the following manner:

- Decreases voltage drop due to resistance across the actuator,
- Increases potential for better electrical contact at the connection.

One fundamental limitation arises due to the embedded wire. As the film is fused to the stiff metal inserts they cause mechanical impedance at the interface between the film and the embedded material as well as along the length of the helix. In order to mitigate this effect a thinner diameter insert is desirable, however this in turn limits the current that can be delivered to the actuator unit. The wire insert can overheat burning out or causing delamination between the two materials. This conflict between mechanical impedance and maximum voltage was settled by choosing a wire diameter that could withstand the typical maximum potentials expected.

Another method of winding wires into a conducting polymer was also attempted. In this approach discrete winding bundles were spaced at even intervals along the length of the film allowing the wire to extend out of the film as tendrils for electrode attachment. The purpose was to remove the mechanical impedance of compressing the helix along the entire length of the film while maintaining the advantages listed above. The other potential benefit expected of this approach was the reduced length between electrode spacing. In the relationship between the voltage drop along the length of the polymer strip defined by Equation 3-1 decreasing the length between electrodes increases the potential gradient along the length of the film. This increases the efficiency of ion flow into the polymer. This is supported by the time constant due to volumetric charging (see

Equation 2-4) which states that in the case where the polymer resistance is significant relative to the solution resistance reducing the spacing between electrodes speeds the rate of response by the square of the difference in length.

Because of the increased performance measured from films grown on nickel rods, this was the deposition material of choice for this section. This change in the base material at the working electrode was expected to create an increase in strains from those synthesized by the University of Wollongong on the platinum rods in the same way that the plain tubes synthesized and tested in the previous section yielded dramatically different results.

3.2.1 Fabrication Methods

Films were grown in a solution of 0.05 M distilled pyrrole monomer and 0.05 M tetraethylammonium hexafluorophosphate in propylene carbonate with 1 % distilled water. The film was synthesized galvanostatically at -20 °C at current densities of approximately 1.25 to 1.5 $A \cdot m^{-2}$. This resulted in films that were generally 35 to 50 μm thick. Depositions were made onto three 1 mm diameter nickel 99.95% rod suspended in a 500 mL graduated cylinder with a copper counter electrode pressed against the walls of the glass. Prior to each deposition the nickel rods were sanded with 1500 grit sandpaper, and wiped clean with acetone. The helical inserts were gold wire 0.025 mm in diameter. Figure 3-22 shows the stages of the deposition process from winding the gold wire to the actuation configuration. In Figure 3-22 (a) the nickel rod which serves as the working electrode for the deposition process is shown with the gold wire wound helically along its length; (b) the nickel/gold wire is placed in the deposition solution with a copper counter electrode; (c) once synthesis is complete the nickel core is removed leaving a hollow tube of polypyrrole with the gold wire helically embedded in the film; and (d) the tubes were then epoxied at each end to a shortened length of nickel rod reinserted into the polymer tube such that electrical contact can be made at both ends.
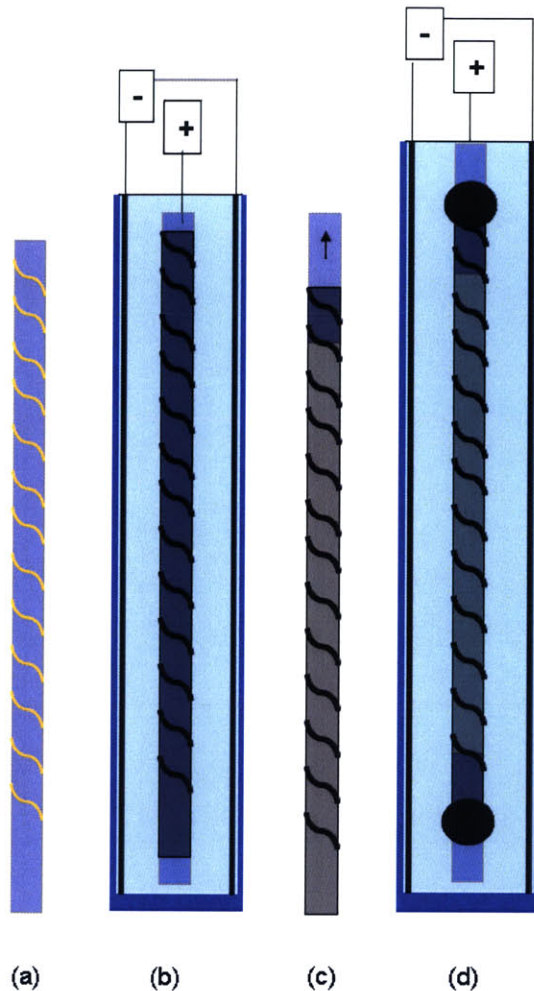
(a)   (b)   (c)   (d)

Figure 3-22. The fabrication process for synthesizing tubes of conducting polymer films with helically embedded wire was performed on (a) a nickel rod with the gold wire wrapped along its length; (b) the unit was placed in a cylinder with a copper counter electrode synthesis is accomplished galvanostatically; (c) once deposition was complete the nickel core was removed leaving a hollow tube with helical wire inserts; (d) the final configuration for the actuator with shortened platinum rods were reinserted into the tube and glued at the ends for electrical contact.

The second method of embedding wire into the hollow tube of polypyrrole involved the use of the same conditions for deposition. Figure 3-23 (a) shows the manner in which the winding for the wires was different as it was wound in discrete bundles three loops at a time over the platinum core; (b) the combined unit was placed in the deposition solution (taking care not to create a short between the copper counter electrode and the dangling gold wire extensions) and synthesis was performed galvanostatically; (c) once the deposition was complete the nickel core is removed leaving a hollow tube of polypyrrole with the embedded wire inserts; (d) the final actuation scheme is shown with two of the

tubes attached to their respective capsules. The walls of the actuation capsules are designed to be conductive such that the gold wire extensions could be soldered or pressed against them for electrical contact along the length of the film. As they share the electrolyte bath one tube acts as a working electrode while the other is the counter electrode.
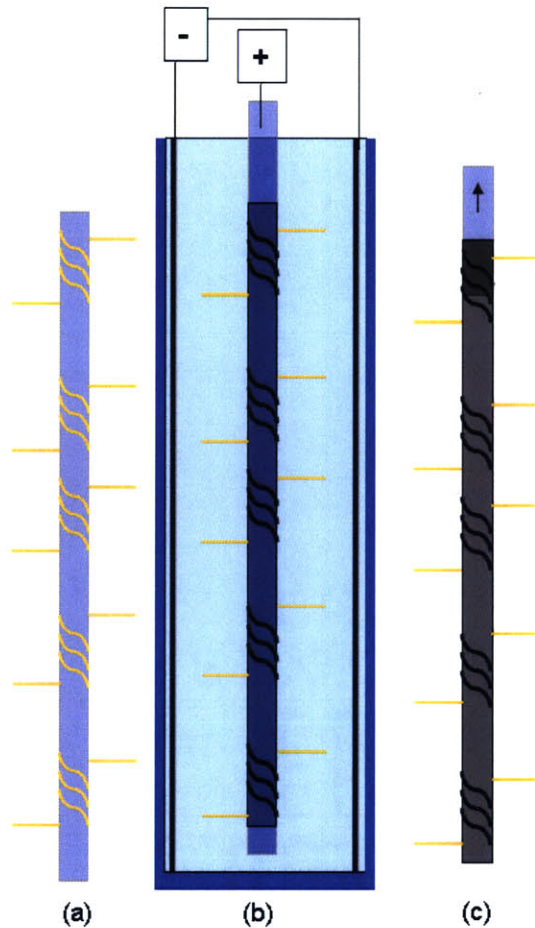

Figure 3-23. The fabrication process for synthesizing tubes of conducting polymer films with brush-like extensions that serve as electrode attachments; (a) a nickel rod was wrapped in evenly spaced intervals with three loops per segment; (b) the unit was placed in the deposition solution taking care not to create a short between dangling wires and the counter electrode; (c) deposition is galvanostatically controlled and the resulting film was removed from the nickel core leaving a hollow tube with electrode attachments along its length.

The brush-like actuators were difficult to work with and yielded unevenly manufactured results. Controlling the wire extensions during winding and deposition was problematic.

The gold wire bundles needed to be long enough to be attached to the actuator column without introducing mechanical impedance. However, the trailing edges of the wires were easily tangled and tended to push against the counter electrode during deposition. This had the effect of shorting the circuit and halting synthesis. Other complications arose from removing them from the platinum core once film synthesis was completed. The trailing leads were easily yanked which would tear the film.

The helical inserts were easier to manufacture as the embedded wire was sealed within the wall of the polymer tube making it easier to handle without danger of tearing during removal of the platinum rod. The one major challenge in the fabrication process of the helix embedded polymer tubes was the tension and regularity of the winding. If the wire was wound too tight it would be impossible to remove from the inner core after deposition. If it was wound too loosely it would separate from the platinum rod creating gaps in the film. Since the wires were wound by hand, achieving the proper tension was a matter of practice.

3.2.2 Testing

Films were tested for dynamic properties on the DMA. Experiments were performed isotonically at specified voltages and frequencies using the resistance compensation wave form developed by Madden et al. The voltage across the polymer film, current, force, and displacement were actively measured. Strain, stress, and charge were calculated from dimensions taken from the polymer tubes using a micrometer to gage film thickness and data taken from the DMA during isotonic testing. Table 3-9 lists the dimensional properties of the samples that were tested. The effective length measurement is the height between clamps on the film. Films were cut to lengths of 15 to 25 mm in order to satisfy the St. Venant's clamping principle which states that the length must be 3 times the width in order to avoid error due to clamping issues.

Table 3-9. The following is a list of dimensions taken from the samples that were used for testing active properties of the two different actuator configurations.

Sample	Effective Length (mm)	Film Thickness (μm)	Cross-sectional Area (10^{-6} m^2)
Helical Insert	9.7	28	0.088
Electrode Extensions	21.7	39	0.12

3.2.3 Results

The results from a typical test are shown in Figure 3-24. The resistance compensation waveform is evident in the measurement of the potential across the film. A 4 V potential was applied for 1×10^{-3} s over each cycle during tests on both films. There is some noise in the stress on this run which was in part due to leaving a stepper motor, used to achieve gross motions, on during testing. Unfortunately, this was an error incurred for this series of tests. There is approximately 0.15 % creep evident in the course of this test performed at 0.1 MPa where the average strain amplitude was 0.56 % at 0.25 Hz of actuation. This apparent creep is less likely to be due to actual creep in the film and more likely attributed to expansion caused by absorption of solvent not reaching an equilibrium point. In previous experiments performed on polypyrrole investigating the creep response of the polymer longer time scales and greater stresses were required to generate a significant creep response (Madden, et al., 2002). Although, samples were left at open circuit potential for a half an hour before testing such that strain due to solvent absorption and expulsion of anions during synthesis could occur; some of this variation was probably due to not attaining a completely steady state before tests were run. By integrating with respect to time the current over each cycle Figure 3-25 was generated. Effects from this apparent creep can be seen in the strain-to-charge ratio as the cycles progress.
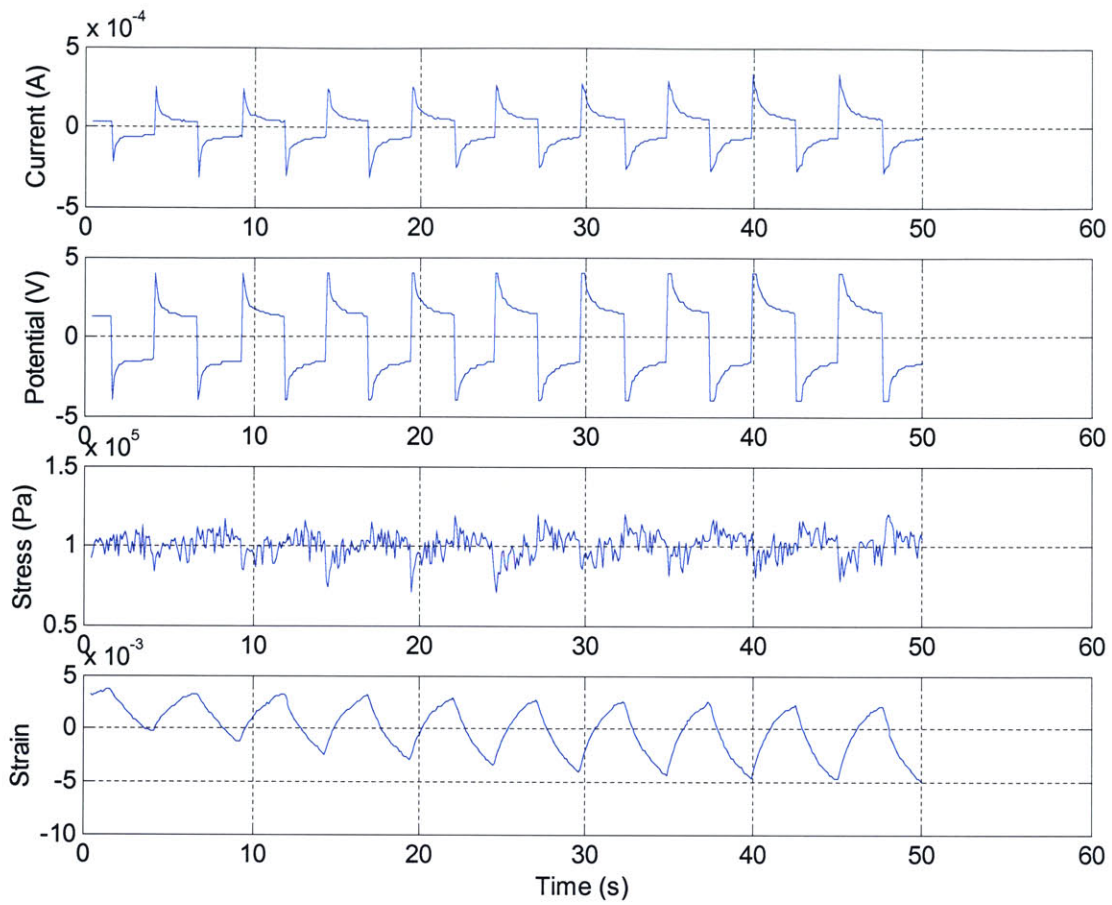
Figure 3-24. Active testing results are shown from a typical trial under isotonic testing of one of the actuator configurations (helix insert).
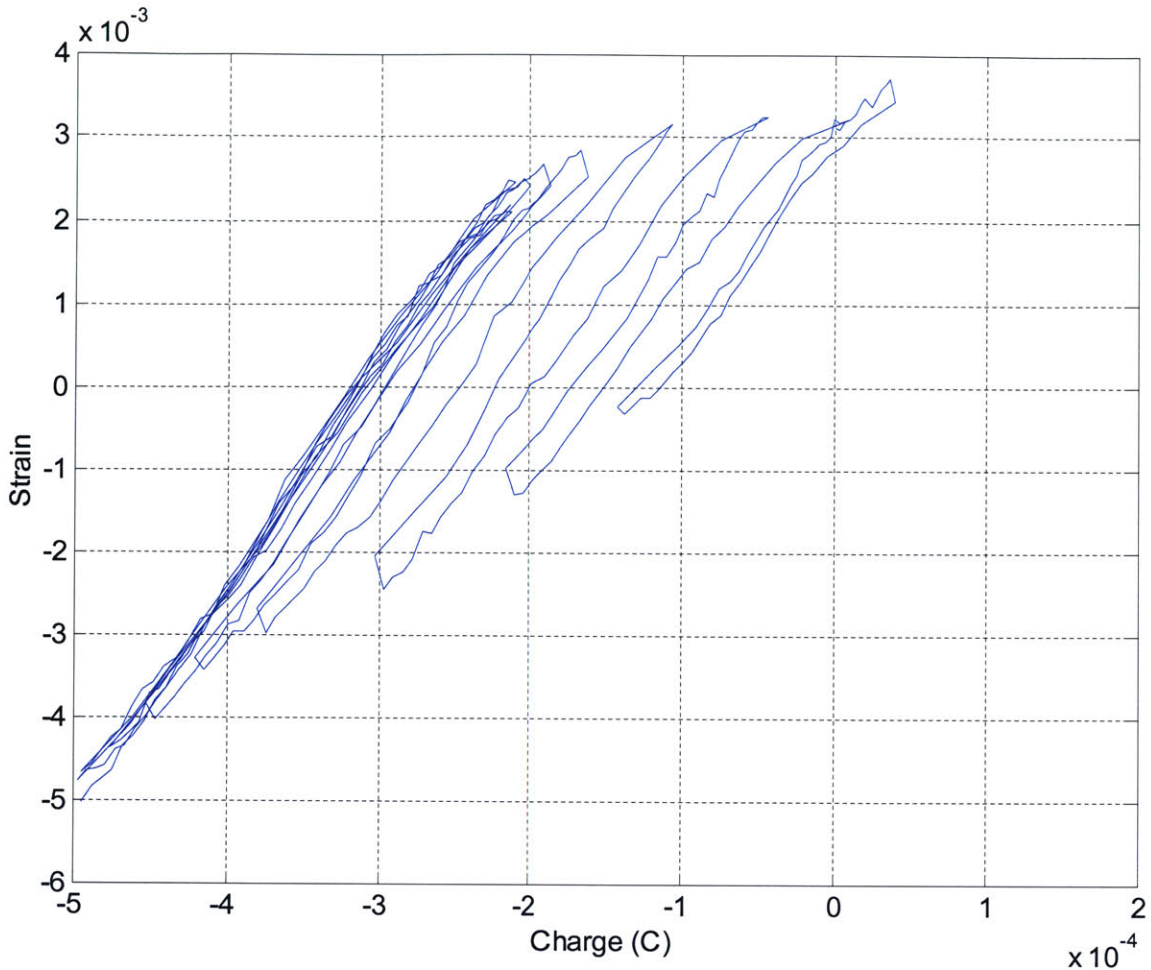
Figure 3-25. Strain versus charge for a typical active test performed on the DMA shows the strain-to-charge relationship for this actuator.

Each sample was excited for 10 cycles per trial. Testing was performed to destruction by applying gradually increasing voltages from ±0.8V, ±1.2 V, and up to ±2.5 V peak-to-peak versus Ag/AgClO$_4$. At each voltage, stresses were increased from 0.1 MPa to 10 MPa in standardized increments. Strain amplitudes were averaged over the 10 cycles for each trial and the results are shown in Figure 3-26. The electrode extension embedded tubes shown in blue (Figure 3-26 (a) and (b)) reached strains of 0.5 % at 0.25 Hz. The sample was tested to failure and broke during a test at ±2.5 V excitation and 0.5 MPa applied stress; just prior to this the actuator yielded its maximum displacement of 0.52 % at 0.1 MPa and ±2.5 V. The helix embedded tubes outperformed these results by more than 200 %. In Figure 3-26 ((c), (d), and (e)) the helically inserted actuators are shown in red. In the final trial shown the actuator reaches strains as high as 1.85 % (Figure 3-26

(e)) at an excitation voltage of ±2.5 V and 0.25 Hz. A peak strain of 2.2 % was attained during this trial and the actuator sample was robust enough to be tested at voltages up to ±5 V and 0.5 MPa although the film began to degrade and strains only reached 1.7 %.
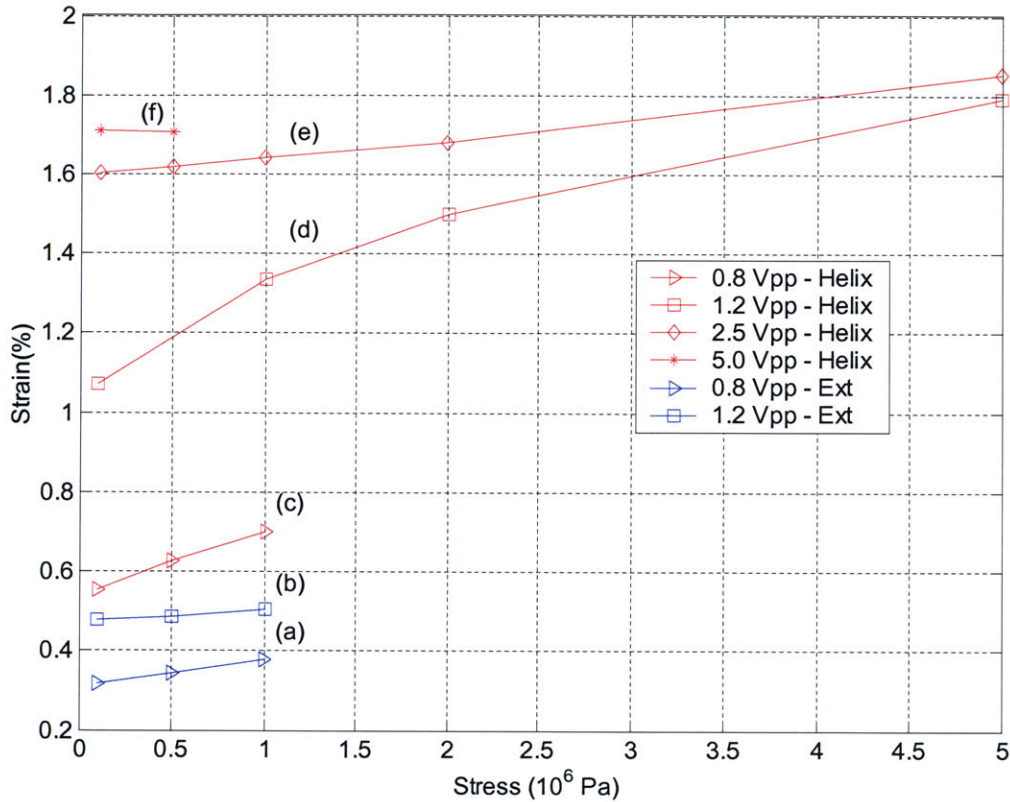

Figure 3-26. The stress versus strain profiles for the electrode extension inserted wires in blue ((a) and (b)) and helix embedded wires ((c), (d), (e), and (f)) are shown in red. The lines are not trend indicators but are intended to demonstrate trials performed at increasing peak-to-peak excitation potentials of ±0.8V ((a) and (c)), ±1.2V ((b) and (d)), ±2.5V (e), and ± 5 V (f) versus Ag/AgClO$_4$. All tests were performed at 0.25 Hz.

The relationship between actuator performance and their maximum potential characteristics are shown in Figure 3-27. The tubular films with the helical inserts not only withstood the highest voltages without degrading, they also showed greater increases in strain between the applied potentials.
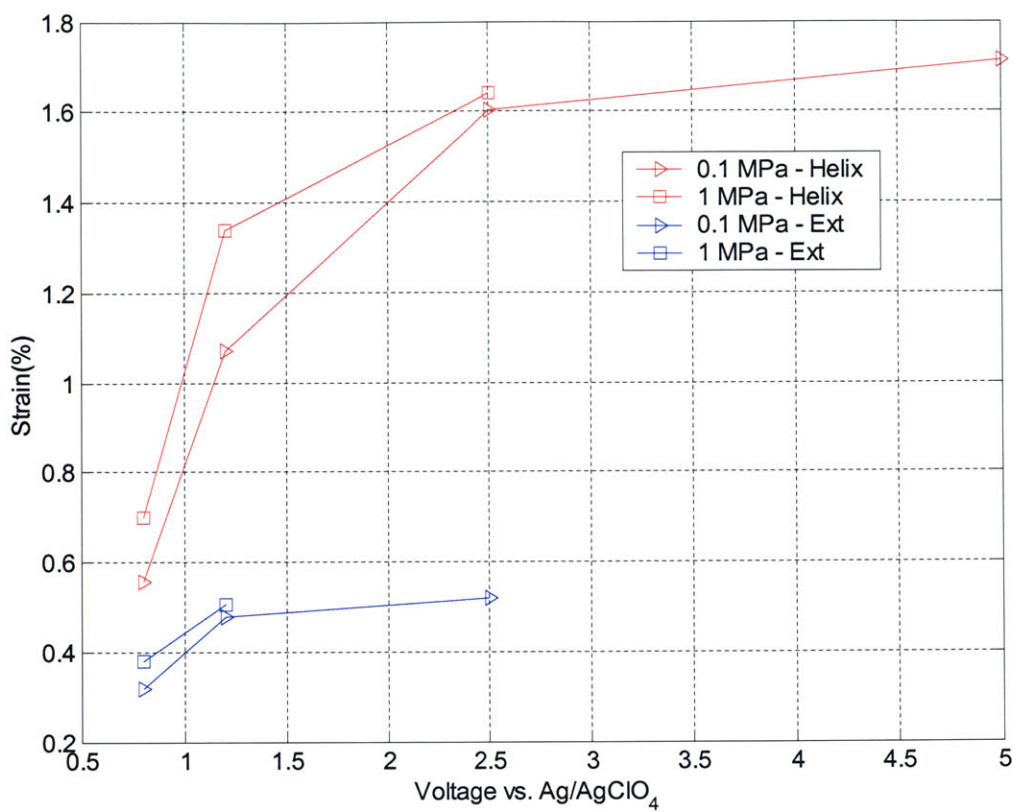
Figure 3-27. The strain versus voltage characteristics for the helically embedded and electrode extension inserted films shows a greater maximum voltage capacity for the helix films as well as greater increases in strain between applied potentials.

Two other measures of the relative effectiveness of these actuators is the efficiency of strain versus charge injection as well as the charging rate. Increasing the strain rate of the actuator can be achieved by improving these two figures of merit. However, in order to accomplish an overall benefit in performance it is necessary that neither one of these figures of merit is sacrificed over the other. Figure 3-28 compares the strain versus charge relationship for the two actuators during the isotonic tests performed under an excitation potential of ± 0.8V versus Ag/AgClO$_4$ at 0.25 Hz and 0.1 MPa. Similarly, Figure 3-29 shows the same test at ± 1.2 V versus Ag/AgClO$_4$ (frequency and stress remained unchanged). Table 3-10 summarizes the results of the figures where the actuators with the helically embedded wires exhibit consistently lower charge injection over a cycle with larger strain amplitudes.

Table 3-10. Summary of strain versus charge results for the two actuator types during two isotonic testing cycles.

	±0.8 V versus Ag/AgClO$_4$ at 0.25 Hz and 0.1 MPa		±1.2 V versus Ag/AgClO$_4$ at 0.25 Hz and 0.1 MPa	
Actuator	Strain to Charge Ratio (C·m^3)	Strain (%)	Strain to Charge Ratio (C·m^3)	Strain (%)
Helix	8.2×10^6	0.56	6.9×10^6	1.1
Electrode Extensions	4.03×10^6	0.31	3.8×10^6	0.48

Figure 3-28. The helix embedded inserts yield a greater strain to charge ratio over the electrode extension inserted actuators during isotonic testing at ±0.8V versus Ag/AgClO$_4$ at 0.25 Hz and 0.1 MPa.
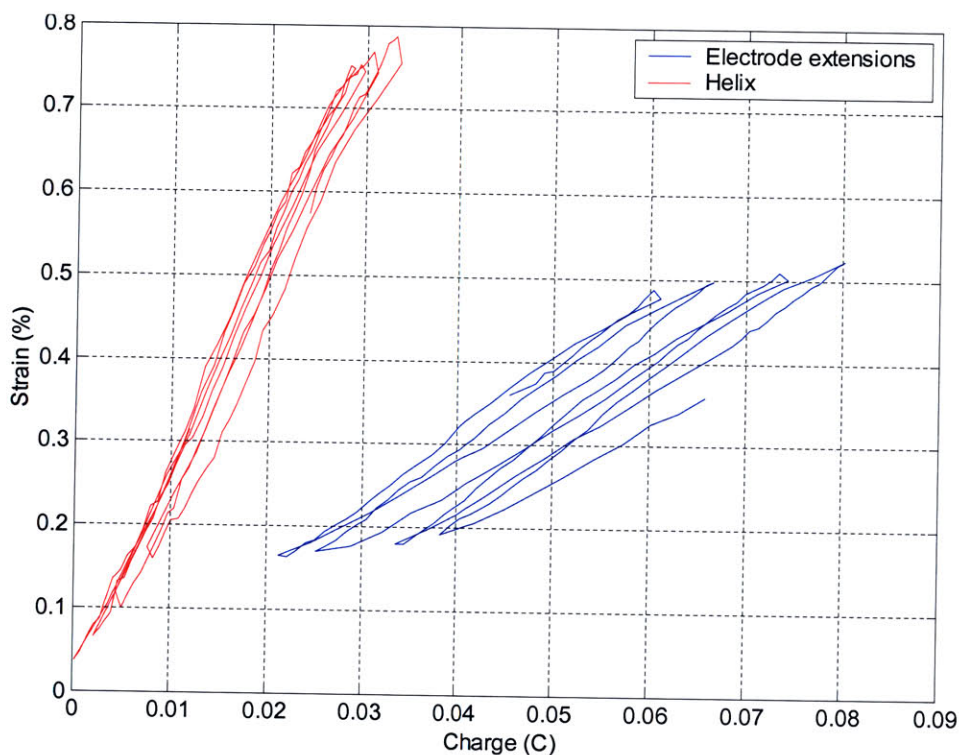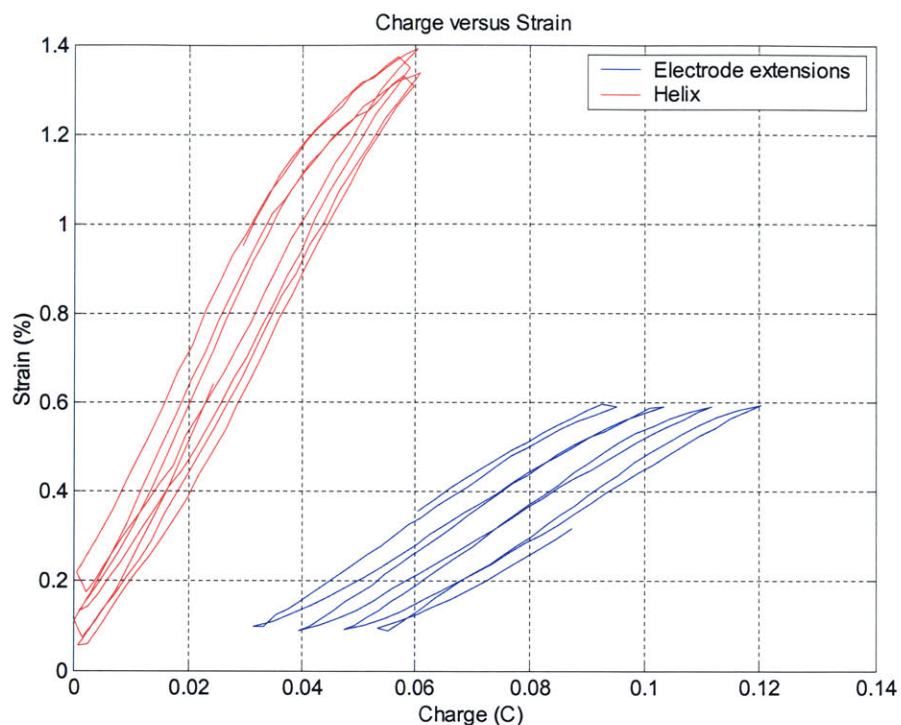
Figure 3-29. The helix embedded inserts yield a greater strain to charge ratio over the electrode extension inserted actuators during isotonic testing at ±1.2V versus Ag/AgClO₄ at 0.25 Hz and 0.1 MPa.

The helically embedded wires proved to be better actuators in the following ways:

- Better mechanical integrity under application of higher voltages and stresses,

- Increased strain to charge ratio,

- Increased strain rate,

- Increased strain,

- Easier manufacturability.

The electrode extension embedded actuators proved to be problematic in that the wires that extruded from their length were easily caught causing tearing. It also appears from the dynamic tests that the electrodes were not as effective at injecting charge into the actuator. It would seem from these results that the mechanical impedance of embedding a wire along the length of the tubular film is less of a liability than previously thought. The continuous electrical connection with the polymer appears to outstrip the periodic placement of wire inserts.

3.3 Embedded Electrodes in Flat Films

Achieving a good electrical connection with the actuator is one of the keys to improving the reliability and speed of an actuator. Cell resistance at the working electrode reduces the potential across the film (Spinks, 2003; Spink,s 2000). The potential at the electrode (V) is given by:

$$V = V_{App} - i(R_S + R_P) \, ,$$

<div align="right">3-2</div>

where V_{App} is the applied voltage, i is the current, R_S is the resistance of the electrolyte solution, and R_P is the resistance of the conducting polymer. The conductivity of the polymer affects the potential when this value is large or in other words across long films, poorly conductive films, or when there are clamping issues hampering connectivity. Maintaining the maximum voltage along the length of the polymer is essential as it increases reaction time by optimizing the concentration of ions in the double layer.

Increasing the conductivity of the polymer is one means of mitigating voltage drop across the polymer. Another method is to incorporate materials into the film. Embedding wiring into tubular films was explored in the previous section. This work was extended to flat films where the geometry and fabrication methods are slightly more versatile. The same issues arise in this work as other properties such as the Young's modulus and the overall strain/charge ratio may be adversely affected such that care must be taken to diminish any negative effects.

3.3.1 Fabrication Methods

Films were grown in a solution of 0.05 M distilled pyrrole monomer and 0.05 M tetraethylammonium hexafluorophosphate in propylene carbonate with 1% distilled water. The film was synthesized galvanostatically at -40 °C at current densities of approximately 1.25 to 1.5 $A \cdot m^{-2}$. Synthesizing a minimum film thickness was necessary for coating embedded fabrics and fibers. Depositions were made onto a glassy carbon crucible masked with Kapton © tape. Figure 3-30 shows the crucible after a deposition

with a variety of conductive materials that were masked to the cylinder's surface during synthesis. Electrical contact with the crucible was made by taping the materials down.
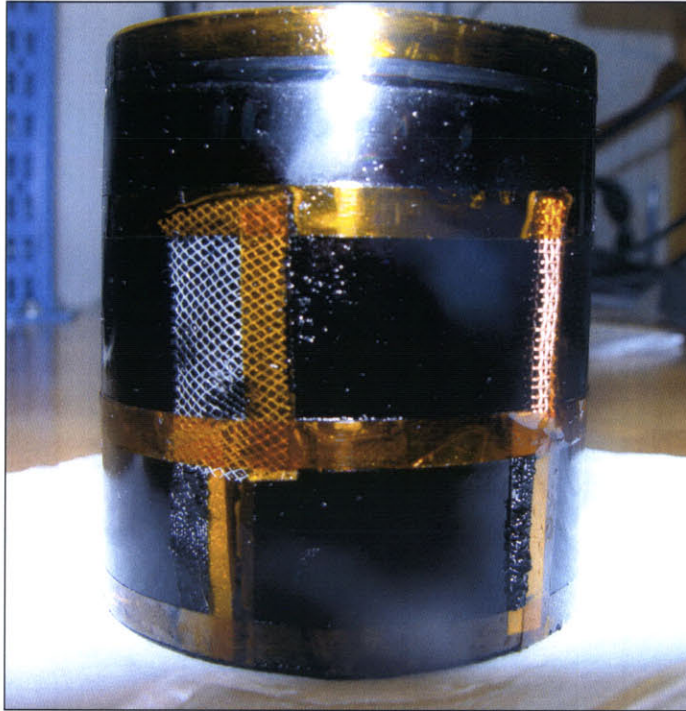
Figure 3-30. A glassy carbon crucible masked with Kapton © tape was used to synthesize flat films with conductive materials embedded at the contact site on the actuators.

3.3.2 Testing

An assortment of fibers, fabrics, and films were taped to the crucible but only a few worked. The materials varied in thickness, tightness of weave, and conductivity. The two most successful adhesions between films and embedded materials were a 0.025 mm gold wire (Figure 3-31 (A)) and a silver coated tightly woven fabric (Figure 3-31 (B)). These two actuators were taken from the same crucible deposition and tested against a plain control sample.

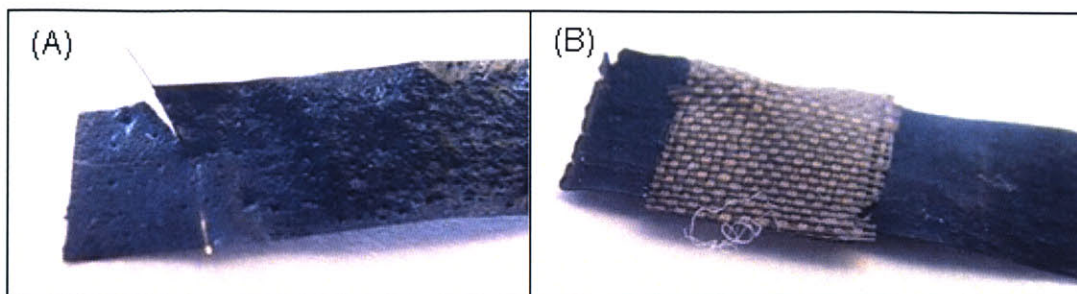Figure 3-31. Two strips with, a 0.075 mm diameter gold wire (A) and silver coated cloth (B), embedded perpendicularly to direction of actuation at the working electrode sight were fabricated at the same time on a glassy carbon crucible.

The films were tested for dynamic properties on the DMA. Experiments were performed isotonically at ±0.8 V versus Ag/AgClO$_4$ and a frequency of 0.25 Hz for 10 cycles per test using the resistance compensation wave form developed by Madden et. al. Table 3-11 lists the dimensional properties of the samples that were tested. The effective length measurement is the height between clamps on the film. Films were tested at lengths of 15 mm in order to satisfy the St. Venant's clamping principle which states that the length must be three times the width in order to avoid error due to clamping issues.

Table 3-11. The following is a list of dimensions taken from the samples that were used for testing active properties of the different actuator configurations.

Sample	Effective Length (mm)	Film Thickness (μm)	Film Width (mm)
Plain film	15.5	30	4.0
Silver cloth	17.9	30	5.0
Gold wire	20.4	30	4.5

3.3.3 Results

Table 3-12 summarizes the maximum strains exhibited for each actuator at an excitation voltage of ±0.8 V versus Ag/AgClO$_4$ and a frequency of 0.25 Hz. The actuator with the gold wire insert at the working electrode outperformed the other two actuators by as much as a factor of 3.3 even at their relative maximums but showed degradation between tests performed at 1 MPa and 5 MPa. The strain versus stress characteristics for this

group of actuators is shown in Figure 3-30. The drop in performance of the film with the gold wire inserted can be seen in the figure as the strains drop from an average of 1.9% average strain over the 10 testing cycles at 1 MPa to 1.4% at 5 MPa.

Table 3-12. Summary of maximum strains and their respective stress and charge conditions for the trial at which the maximums occurred.

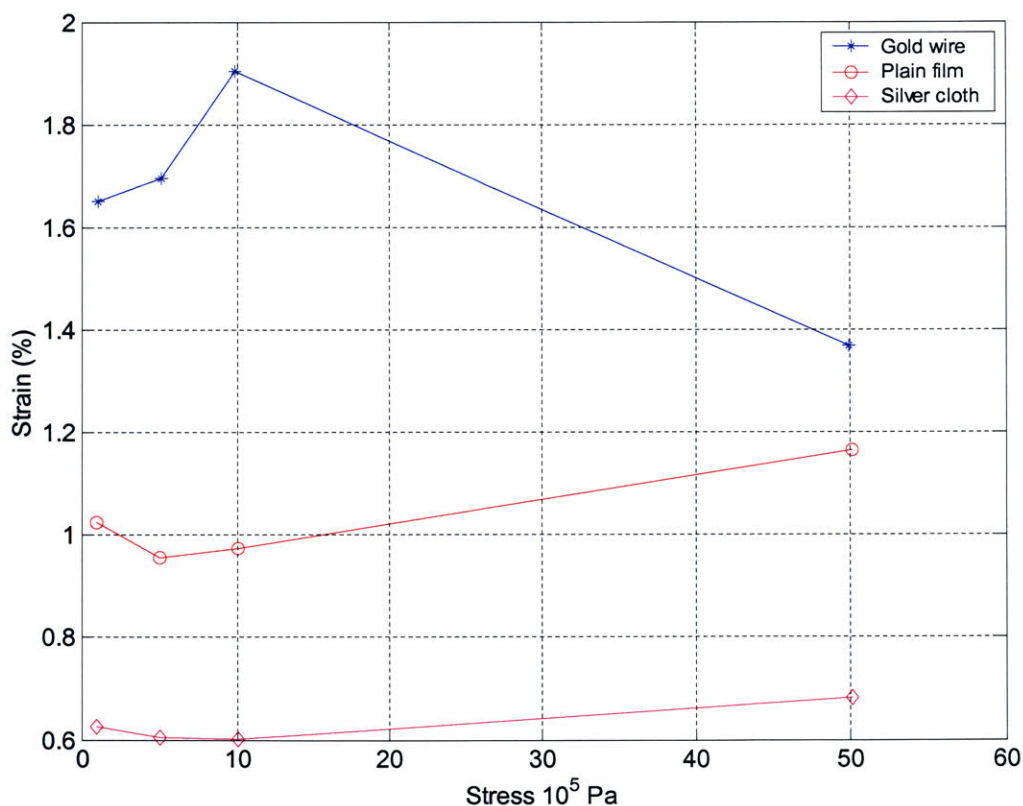| Sample	Maximum strain (%)	Stress (MPa)	Average charge (C)
Plain film	1.24	5	0.061
Gold wire	2.40	1	0.10
Silver cloth	0.73	5	0.051

Figure 3-32. The strain versus stress characteristics during isotonic testing at ±0.8 V versus Ag/AgClO$_4$ at 0.25 Hz are shown for the two flat films with embedded electrode materials as they compare with a plain flat film.

The plain film was outperformed by the actuator with a gold wire embedded at the working electrode sight as shown in Figure 3-33 by as much as 96 % at 1 MPa. Overall,

the film with the gold wire yielded the highest strains and strain to charge ratios (Table 3-13). Although Figure 3-32 suggests that the embedded film has an earlier mechanical degradation point as the strain dramatically decreased at 5 MPa for the gold wire inserted film. The silver cloth proved to have a negative effect on the overall performance of these actuators. The strain output was diminished and the strain to charge relationship was the lowest of the three samples (Table 3-13). This decrease in performance is probably due to lack of adhesion between the fibers of the cloth and the film. The net result of this would be an increase in resistance at the working electrode. The photograph shown in Figure 3-31 of the silver cloth embedded sample shows that the film grew around the cloth, but does not appear to have filled the spaces in between the fibers of the material.

Table 3-13. Strain to charge ratios for each isotonic test performed for the flat films with embedded materials testing at ±0.8 V versus Ag/AgClO$_4$ at 0.25 Hz.

Sample	Strain to Charge Ratio (10^6 C·m^3)	Strain (%)	Stress (MPa)
Gold Wire	7.5	1.65	0.1
	7.7	1.69	0.5
	8.6	1.90	1
	5.9	1.37	5
Plain Film	6.6	1.03	0.1
	6.2	0.96	0.5
	6.4	0.97	1
	7.5	1.16	5
Silver Cloth	4.2	0.63	0.1
	4.2	0.61	0.5
	4.2	0.60	1
	4.8	0.68	5

3.5 Chapter References

1. Anquetil, P. Large Contraction Conducting Polymer Actuators, Ph D. Thesis. Cambridge, Ma: Massachusetts Institute of Technology: 2005.

2. Jie D., Lu L., Spinks G., Dezhi Z., Wallace G., Gillespie J. High Performance Conducting Polymer Actuators Utilizing Tubular Geometry and Helical Wire Interconnects. Synthetic Metals. 2003; 138: 391–398.

3. Hutchison A., Lewis T., Moulton S., Spinks G., Wallace G. Development of Polypyrrole Based Electromechanical Actuators. SPIE Conference on Electroactive Polymer Actuators and Devices Newport Beach, 1999; 3669: 242-253.

4. Hunter, I., Lafontaine, S. A Comparison of Muscle with Artificial Actuators. Technical Digest IEEE Solid State Sensors and Actuators Workshop IEEE. 1992; 178-175

5. Madden J., Cush R., Kanigan T., Hunter I. Fast Contracting Polypyrrole Actuators. Synthetic Metals. 2000; 113: 185–192.

6. Madden, J. D. Conducting Polymer Actuators, Ph. D. Thesis. Cambridge, MA: Massachusetts Institute of Technology: 2000.

7. Madden, J. D., Madden, P. G., Hunter, I. Conducting Polymer Actuators as Engineering Materials. Smart Structures and Materials 2002: Electroactive Polymer Actuators and Devices (EAPAD), Yoseph Bar-Cohen, Ed., Proceedings of SPIE. 2002; 4695: 176-190.

8. Madden J., Rinderknecht D. Characterization of Polypyrrole Actuators. Report to the National Science Foundation. July 2002.

9. Madden, P. G. Development and Modeling of Conducting Polymer Actuators and the Fabrication of a Conducting Polymer Based Feedback Loop, Ph. D. Thesis. Cambridge, MA: Massachusetts Institute of Technology: 2003.

10. Otero T., Sansinena J., Soft and Wet Conducting Polymers for Artificial Muscles. Advanced Materials. 1998 Apr 16; 10(6):491.

11. Spinks G., Dezhi Z., Lu L., Wallace G. The Amounts per Cycle of Polypyrrole Electromechanical Actuators. Smart Materials and Structures. 2003;12: 468-472.

12. Rinderknecht, D. Design of a Dynamic Mechanical Analyzer for the Active Characterization of Conducting Polymer Actuators, Bachelor Thesis. Cambridge, MA: Massachusetts Institute of Technology: 2002.

4.0 Co-fabrication

Assembly represents one of the most significant portions of the manufacturing costs for classical mechatronic devices. Handling, maneuvering, connecting, aligning, building, and managing parts in the assembly process can represent as much as 90 % of the total manufacturing cost (see Table 4-1). At GM and Ford, designers estimate approximately 1000 to 1800 manufacturing equipment parts for every product part. In other words, for every toleranced dimension or feature on a product part, there are about 1000 toleranced dimensions or features on manufacturing equipment. For the purposes of this discussion manufacturing equipment includes fixtures, transporters, dies, clamps, robots, machine tool elements, etc (Whitney, 2004). The ideal assembly process defined by Dr. Peter Will of ISI/USC emphasizes the minimization of parts and the impact of making connections between them. The "assembly process from heaven" is designed such that:

- Parts can be assembled one-handed by a blind person wearing a boxing glove,
- Parts are stable and self-aligning,
- Tolerances are large enough for loose and forgiving connections,
- There are few fasteners,
- It requires few tools and fixtures,
- Parts are presented in the right orientation,
- Parts are asymmetric for easy feeding,
- Parts are easy to grasp and insert.

These ideas are echoed in the research findings of Geoffrey Boothroyd who found in his studies conducted in the 60's and 70's that the main cost in the assembly process are the parts. He asserted that because of the expense they generate products should be designed for the minimum number of parts possible even if those parts were then required to be more complex. These ideas are supported by the cost estimations reported in a study of manufacturing cost conducted by the International Motor Vehicle Program (Whitney, 2004; Boothroyd, 1991). The results of their study are summarized in Table 4-1.

Table 4-1. A manufacturing cost breakdown study highlights the impact of parts on the total cost of manufacture (Whitney, 2004).

Product	Parts (%)	Labor (%)	Capital (%)
VCR	90	5	-
Car engines	75	7	7
Mini computers	65	25	-
Fighter planes	50	40	-

Given the cost associated with the manufacture and fabrication methods required to put together classical mechatronic systems, it seems evident that a novel approach which evades assembly altogether would have profound consequences. Such a process could potentially create a price reduction phenomenon similar to that seen with the personal computer. As the production of transistors went from an assembly of components to an integrated device that was "grown" the cost of making computers dropped by orders of magnitude making them more powerful and prolific than could have been imagined prior to this technological breakthrough in their manufacture. This potential for a dramatic reduction in the cost of manufacture is the impetus for the creation a co-fabricated robotic device.

Because of the diversity in form and function achievable with conducting polymers they are a particularly promising technology in the realization of a co-fabricated mechatronic device. The electrochemical synthesis process lends tremendous flexibility in the geometric form, conductivity, actuation and material properties of the polymer allowing their use as actuators, structural elements, sensors, passive and active electronic circuit elements, and batteries. The primary approach adopted for the scope of this work was to explore a variety of casting and synthesis techniques which incorporate conducting polymer actuators into a mechanical model of the pectoral fish fin. The casting and molding process is well suited to the needs of this project because complex geometries and material interactions can be implemented for the purpose of creating compliant mechanisms for joints and achieving varied structural properties. The end result is exactly what Boothroyd asserts is the ideal design for assembly: fewer parts that have more functionality built into each element.

4.1 Molding Techniques

There are two different approaches to the molding/casting process that were used. Both involved the use of the 3D Systems rapid prototyping device; a stereo lithography based 3D printer with up to 50 μm resolution. This printer uses an epoxy resin that cures with material properties very similar to polycarbonate (see Appendix A). The final product has a smooth finish, is machinable, and optically translucent. The desired fin geometries were designed in the Unigraphics NX 2.0, a 3D CAD environment, and were either printed as positives for the purposes of casting into a soft mold or were used to generate hard molds that were printed for use as a direct pour. A variety of urethanes and silicones were used to either serve as mold material or for the fin itself. The fin design capitalizes on the use of different durometer elastomers where the physical properties of the fin are required to change in order to achieve mechanical connections, structural elements, or joints. This often created complexity in terms of material interactions. Some elastomers will bond to each other while others will not. Also, the viscosity of the elastomer in its uncured state affects the workability of the material in that it is sensitive to whether the mold is hard or soft. The hardness of the cured elastomer will also affect its workability and whether the mold it was poured in was either hard or soft. The basic benefits and drawbacks of using hard or soft molding techniques is discussed for the purpose of illuminating the best methods for a given elastomer material. Factors such as their respective strengths and weaknesses were considered in terms of casting a fairly complex geometry with various material properties.

Soft molds were cast from positive geometries. For the purposes of this project the positives were generated in a 3D CAD environment an example of one such geometry is shown in Figure 4-1. The different material properties of this iteration of the fin design are represented by color. The dark amber base is a harder durometer than the lighter yellow webbing which was cast using the softest and most flexible silicones and urethanes available. Although it's not visible in this view, the three fin rays shown in Figure 4-1 are the hardest material in the fin. They were printed using the epoxy resin

and molded directly into the fin. This feature is not evident in the figure as the fins are embedded in the webbing material.
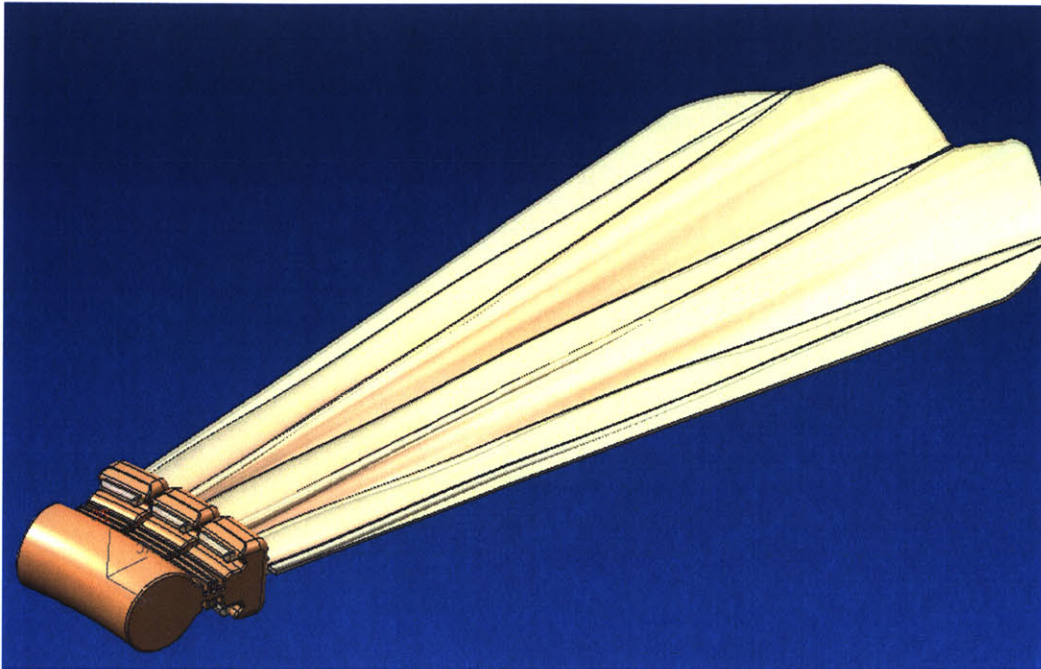

Figure 4-1. A 3D CAD model of the fin shows the details of the geometries on this iteration of the fin design.

Once the positive form is printed as a solid it is used to cast a soft mold. Figure 4-2 shows the positive next to a urethane mold that was cast from it. Soft molds tend to yield the best results when using materials that have a high viscosity in their uncured state. Because the molds are flexible the elastomer can be poured in slowly after it has been degassed. By carefully pressing the two sides together, air bubbles are rarely introduced in the final product. Lower viscosity elastomers will also work in a soft mold but because they run easily the previous technique for keeping air out is not as effective making this method more vulnerable to air in the cured result.

Achieving variation in the material properties of the final version of the cast fin is accomplished by pouring in phases. The uncured elastomer is poured to the desired level in the mold and stored such that the material settles into the desired zone of the mold. Subsequent pours fill the rest of the mold and different layers of varying durometer can be attained. This is an effective method as long as the materials bond.

The primary benefit of this approach is its quick development time. Soft molds require an extra casting step in that the mold is poured around a positive. Regardless, of the fact that hard molds will take a direct pour of the uncured elastomer they require far more detail in the design at the CAD level. It is often faster to make the mold than to draw it. Another benefit of soft molds is the ease of release from the mold. At times, the complex geometries or harder durometer materials are difficult to remove from a mold. This is almost never an issue with soft molds. The draw backs in this approach involve trade-offs in degradation (number of successful uses of the mold) and reliability. Soft molds will begin to wear which decreases their life time and also the reliability of the net result.
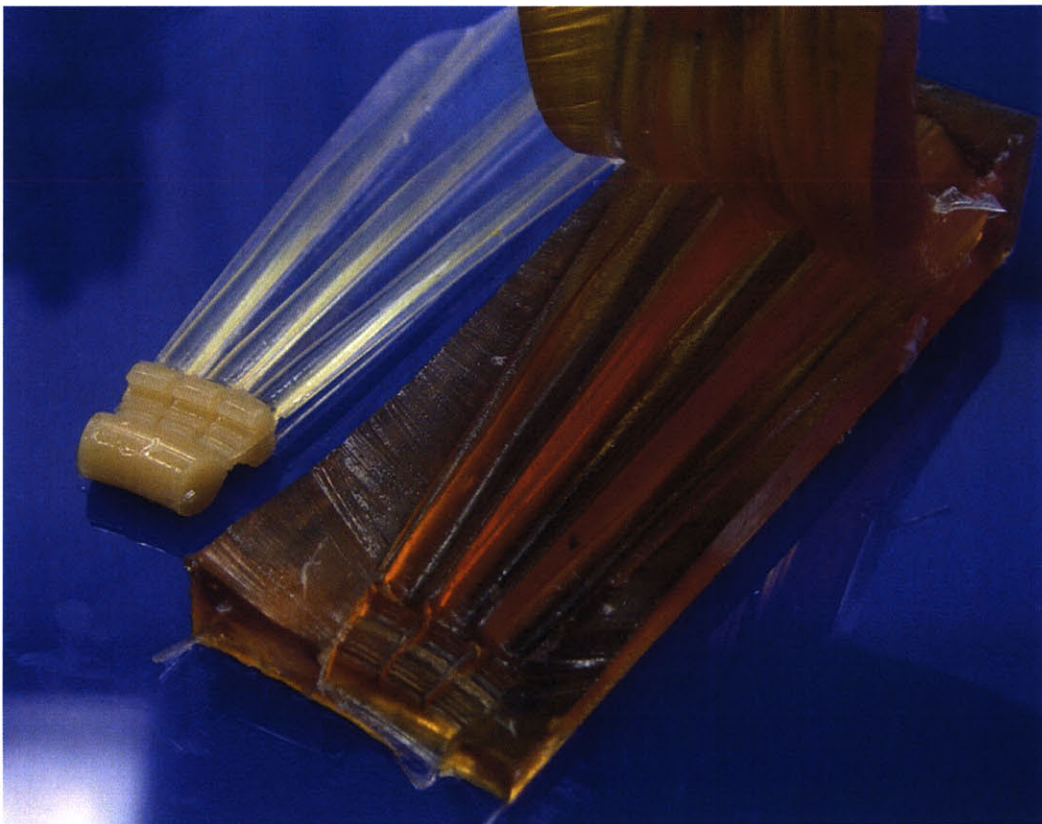

Figure 4-2. The positive printed solid version of this iteration of the fin design sits next to the soft mold that was cast in urethane.

Hard molds are created from the same initially desired geometry as in the case of a soft mold. However, in this method the fin is extracted at the CAD level of design. Figure 4-3 shows the CAD model of a hard mold that was printed and used to pour fins. This particular iteration of the fin design is simpler than the version shown with the soft mold

techniques. This is an earlier rendering of the fin where the web design was flat. The mold is shown split in half so that the details of the fin geometry and the mold can be seen. There are many gates and vents on the mold, these features are used to aid in the prevention of bubble formation during pouring. Because gates and vents can be easily incorporated into hard molds this process is more amenable to low viscosity pour elastomers. Using a syringe, the fluid (which has already been degassed) is pumped into the mold pushing out any trapped air.

There are actually two molds shown in Figure 4-4. The white base is a stand alone mold. The yellow and white sections are independently sealable such that various materials can be poured into each segment without interaction or interference. The ability to control the shape of the seal also yields an interesting result in that one can attain voids or geometries within the cast product. Figure 4-3 shows a seal that was used with this fin design. This seal or plug has features that are created inside of the upper portion of the web. When the upper portion of the fin is connected to the white base shown in Figure 4-4, the elastomer will fill the voids created by the plug. One of the major benefits of this technique is that it offers tremendous control over variation of material properties within the design, an increased ability to accomplish unusual geometries, and/or stronger connections between material phases.

In contrast with the soft mold this process is characterized by a slower development time. However, the finished product is printed in a hard enough material that there were no effective degradation issues yielding a more reliable output product. More importantly, hard molds are better for achieving the truest resolution. Because the mold is used directly from the rapid prototyping environment the only constraint to resolution issues are a factor of the printing process and not prone to losses incorporated from casting a soft mold.
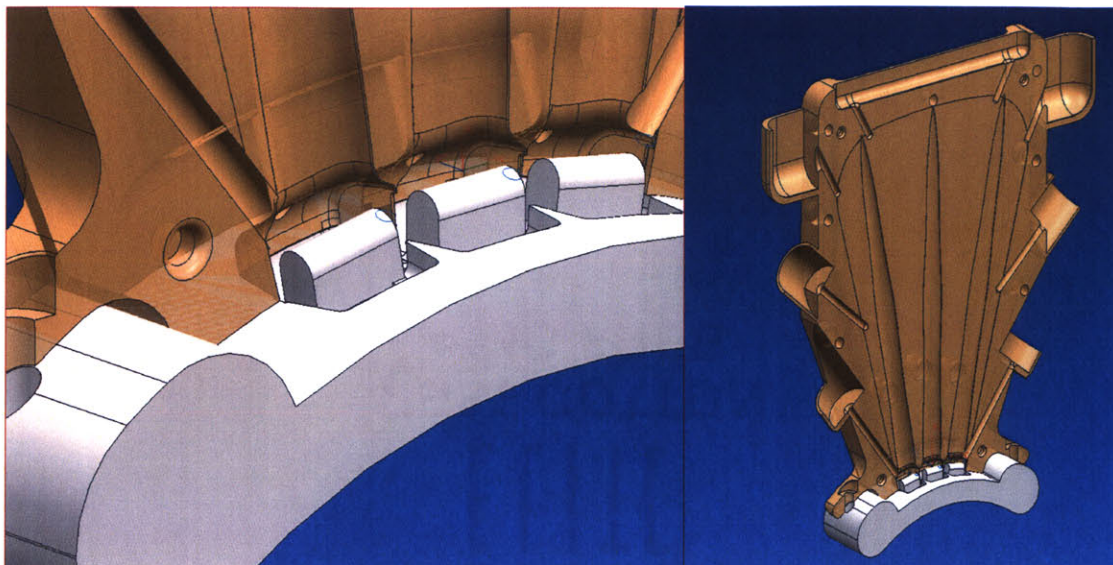
Figure 4-3. The white segment is the plug that was used to seal the mold for the web. This plug created voids in the cast web that were filled with a harder durometer material in the next pouring cycle.
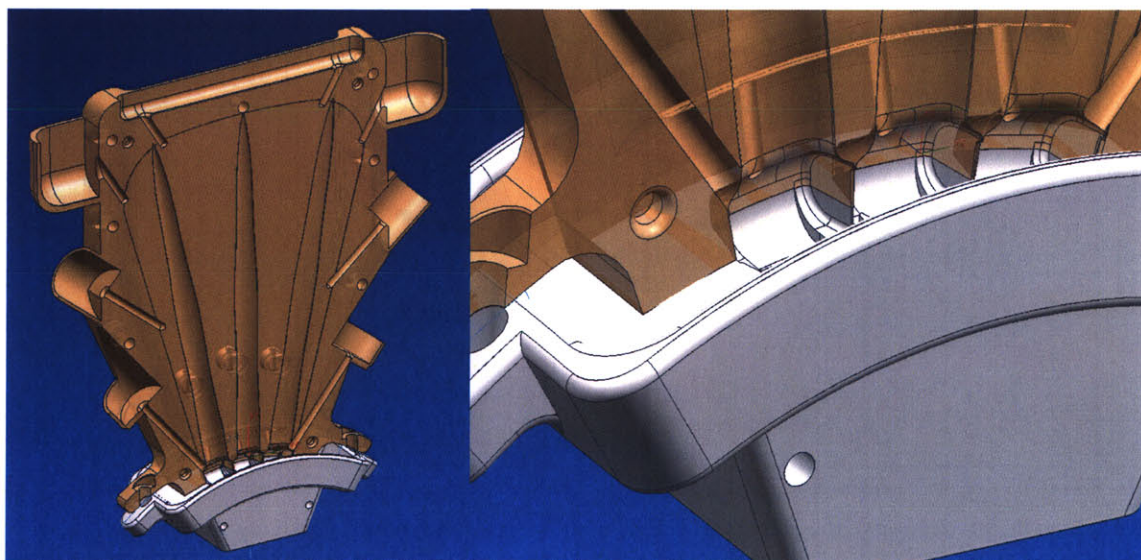

Figure 4-4. This hard mold design is shown split in half such that details of the vents and the fin geometry are visible. The upper yellow portion is a mold of the web while the white base is a mold of the lower part of the fin.

The final process used for casting the fin used both hard and soft mold phases of the pouring procedures.

4.2 Integration of Conducting Polymer

4.2.1 Chemical Deposition

Films were deposited onto an elastomer substrate by creating a conductive surface via chemical deposition of a conducting polymer film. Chemically deposited films can be synthesized on almost any material and surface texture; however the quality of these films is often unreliable. Difficulties in attaining a contiguous film and/or retaining conductivity in the films were common. Because chemically oxidized films are generally poorer quality than electrochemically synthesized films in terms of their conductivity and actuation properties, the chemical deposition process was followed by an electrochemical phase.

Two chemical oxidation solutions were prepared. Samples of urethane, silicone, and epoxy resin with characteristic geometric features immersed in the mixture and stored for 24 to 48 hours. The recipes for each deposition solution are as follows:

- Iron (III) chloride based solution in distilled water (De Rossi, Della Santa, and Mazzoldi, 1999; Spinks, 2002; Madden , 2003). The 1,5 Napthalenedisulfonic acid tetrahydrate and pyrrole were mixed together while the ferric (III) chloride was dissolved in a separate aqueous solution.
  - o 0.006 M 1,5 Napthalenedisulfonic acid tetrahydrate,
  - o 0.02 M Pyrrole,
  - o 0.046 M ferric (III) chloride.
- Silver Nitrate based solution in propylene carbonate was simply combined and stirred.
  - o 0.05 M silver nitrate,
  - o 0.05 M pyrrole,
  - o 0.05 M tetraethylene ammonium phosphate,
  - o 1% distilled water.

The iron (III) chloride and silver nitrate solutions yielded very different results. In the ferric solution some films appeared smooth and adhered completely to the surface of the

elastomer substrate while others were crumbly and rubbed off easily when dried. The quality of the film was dependent on the material substrate and was probably largely affected by the degree of its hydrophilicity. Figure 4-5 shows the results of a 24 hour deposition on the three samples of urethane, silicone, and epoxy resin with characteristic features found on the fin design. The urethane sample appears to be evenly coated but no conductivity could be measured. Since the probes used to measure the resistance across the surface of the urethane dug into the elastomer it seemed possible that the measurement system was unable to detect its conductivity. As a result, attempts were made to perform an electrochemical synthesis regardless of resistance measurements. However, films oxidized in the ferric chloride solution did not yield films when exposed to an electrochemical synthesis deposition phase.

Urethane
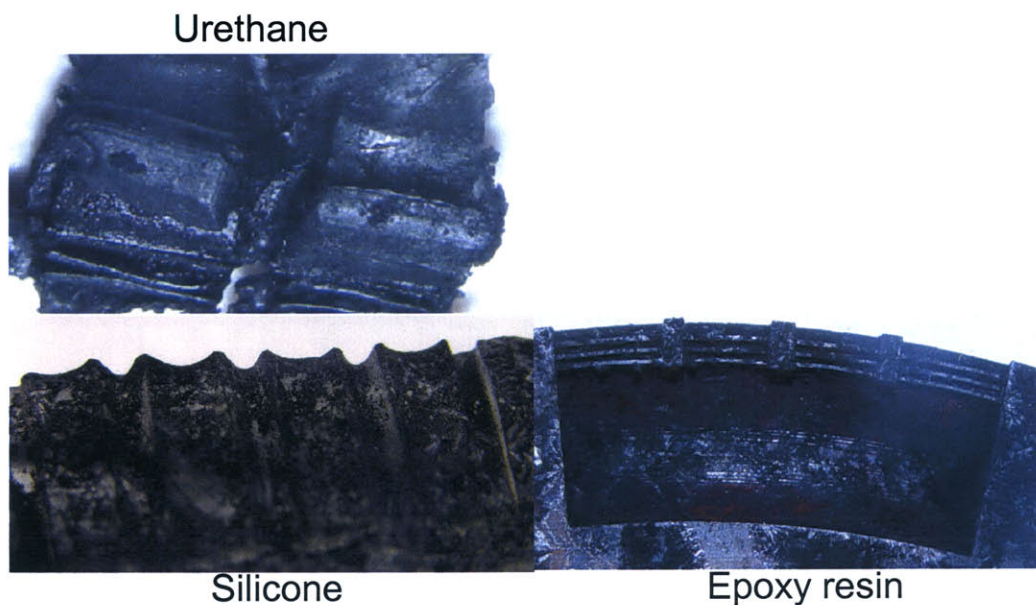

Silicone   Epoxy resin

Figure 4-5. Deposition results after 24 hours immersed in a ferric (III) chloride chemical oxidation solution.

The results of the silver nitrate based oxidation solution were more stable than the ferric (III) chloride mixture. Films appeared contiguous and were conductive enough to capture measurements although values were far too inconsistent to report. This variability is probably due to the softness of the materials. As the probes of the measurement system press into the film, the distance between probes and possibly the integrity of the film might change. Another interesting result of this process was a

corrosive quality it showed with certain urethanes. The Evergreen 10 urethane series (see Appendix A) was almost completely disintegrated in this solution, but is stable in propylene carbonate solutions containing no silver. Because of the caustic effects on this material, the possibility of creating an evacuated structure with a conducting polymer film is evident. Depositions can be performed on the urethane which is subsequently evacuated leaving a void in the core while continuing to oxidize conducting polymer on the remaining surfaces. The results of chemical oxidations on PMC 121/20 (urethane) and Dragon Skin (see Appendix A) fins in the silver nitrate solution are shown in Figure 4-6 The silicone fin's oxidation results are visibly better. The film is smooth and covers the surface geometries completely.
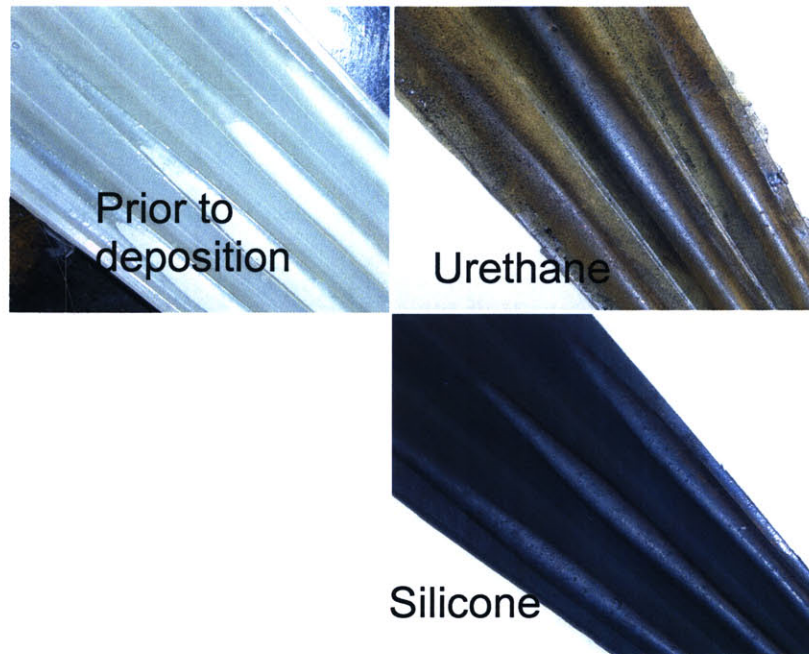

Figure 4-6. Deposition results after 24 hours immersed in a silver nitrate based chemical oxidation solution. The fin is shown prior to deposition and after for urethane and silicone.

The film formed on the silicone substrate was photographed in the SEM under magnifications of 20× and 1970× in Figure 4-7. The highly magnified image (right) was taken over the apparently smooth region in the lower magnification photograph (left). At this level of magnification, the film does not appear smooth relative to the electrochemically synthesized depositions seen in Chapter 2.
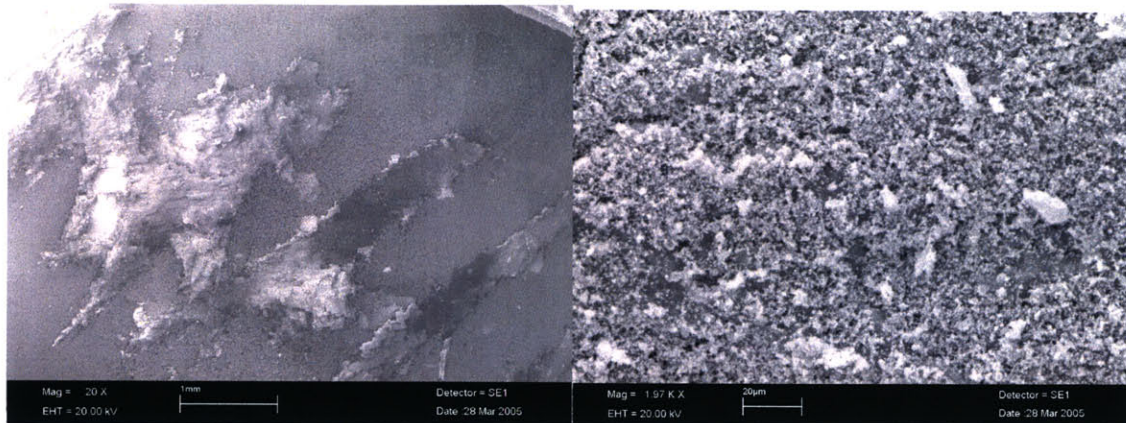
Figure 4-7. The surface of the silicone fin after chemical oxidation is photographed at 20× (left) and 1970× (right) magnifications.

Attempts to perform an electrochemical synthesis post chemical oxidation in the silver nitrate solution were moderately successful. Film growth did occur but the rate of deposition was slow. After 18 hours of deposition time, films of 20 to 50 micrometers were formed. Furthermore, the quality of the films appeared to be poor. Photographs taken of films deposited on silicone with a scanning electron microscope shown in Figure 4-8 and 4-9 reveal the texture of a film deposited on silicone at different magnifications. In Figure 4-8 at a magnification of 143×, the film is shown broken to reveal the surface of the silicone mold and the degree of resolution of surface geometry. Because of the roughness of the film, a degree of precision in surface replication is lost. A photograph of the top (left) and bottom (right) face of the film is shown in Figure 4-9 at 1430× magnification.
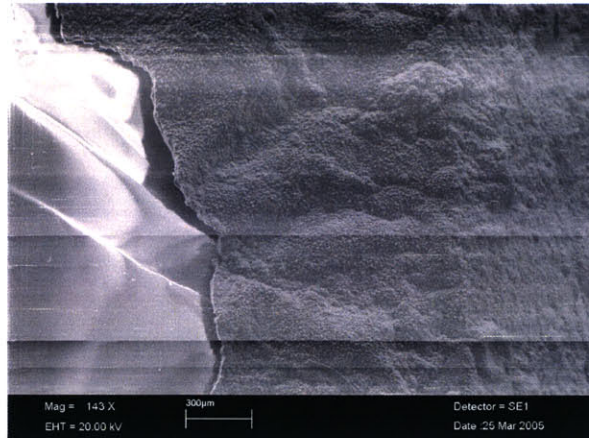
Figure 4-8 Silicone substrate is photographed with chemically and electrochemically deposited film at 143× magnification.
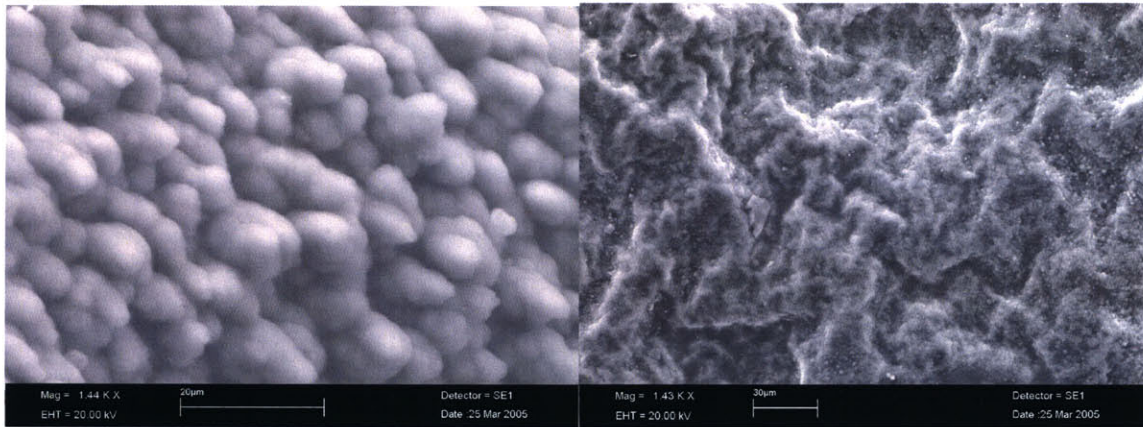

Figure 4-9 Rough textured film deposited on silicone substrate with silver nitrate chemical oxidation solution and followed with electrochemical synthesis was photographed at 1430× magnification on the top (left) and bottom (right) surface.

In contrast to the film grown on the silicone substrate, a film electrochemically synthesized on epoxy resin yielded a very smooth surface with a strong enough adhesion to the substrate material that the film could not be removed in any way that would retain the integrity of the polymer film. Figure 4-10 shows a cylinder of epoxy resin after chemical and electrochemical deposition under magnifications of 80× and 464×. The film is so well adhered that fine surface imperfections are visible through the polymer film at the stronger magnification.
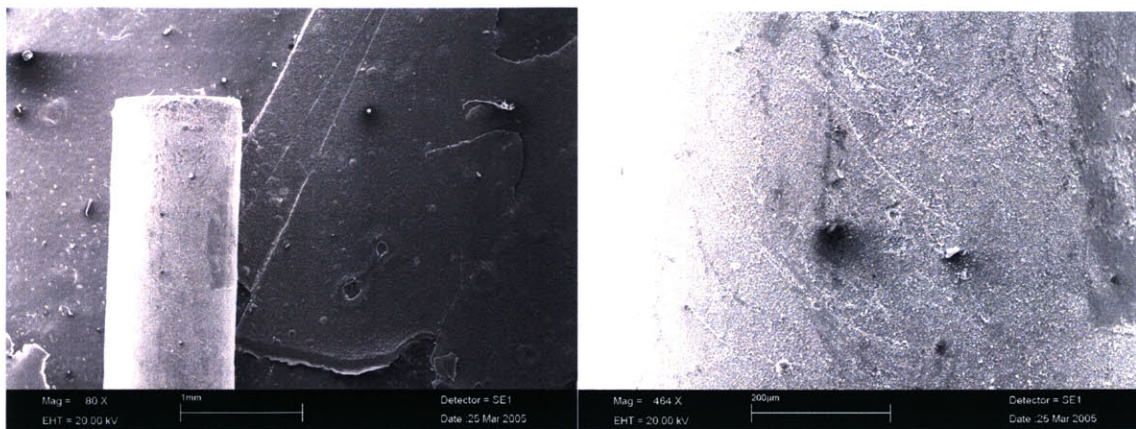
Figure 4-10 Smooth films adhered to the surface of a small epoxy resin cylinder to the extent that fine imperfections were resolved.

4.2.2 Casting Techniques

The other strategy used to integrate the polymer into a fin was to place a previously electrochemically synthesized film into a mold in which an elastomer film was cast. This method was perhaps the simplest and the fastest to realize. The films were synthesized in well-controlled and well-characterized conditions; enabling better consistency of active and passive properties of the film after the casting process. Adhesion between the conducting polymer film and elastomer materials was excellent. Figure 4-11 shows the top and bottom surfaces of a very simple step mold that was used to coat films with urethane. A height differential of 0.1 mm is shown in Figure 4-11 (a); by flipping the view in Figure 4-11 (b) the placement of the polymer film as it was mounted into place using Kapton tape placed can be seen in black.
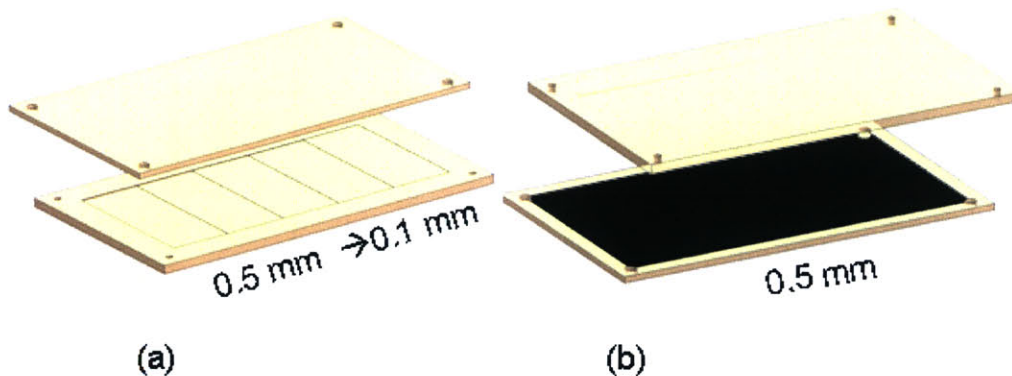
Figure 4-11. The step mold shown from the elastomer casting side (a). A mounted sample of conducting polymer film is shown schematically in black (b).

The problem with coating a film of polypyrrole with an insulating material is a loss in speed as an actuator. In a discussion of the governing time constants in the design and implementation of a conducting polymer actuator the diffusion reaction is reduced by a factor of four if both sides of the film are exposed (see Equation 2-5). Coating the film effectively removes this factor. Another molding technique was designed that would hopefully mitigate this effect by creating an open lattice on the surface of the coated side of the film. Figure 4-12 shows two open faced molds that were used to cast urethane onto films of polypyrrole. The grooves were either 2 mm or 1 mm in diameter and the conducting polymer was simply pressed against the surface of the molds.
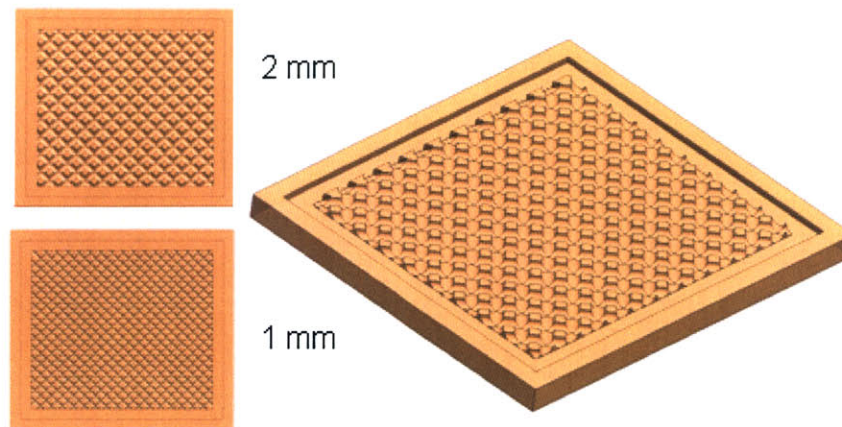
Figure 4-12. The patterned surface of these molds increases the exposed surface area of the conducting polymer after it was cast.

These two casting techniques were relatively successful. One important indicator was an almost non-existent effect on the conductivity of the films. Conductivity measurements from the films pre and post casting were 2.8×10^4 S/m uncoated versus 2.4×10^4 S/m coated.
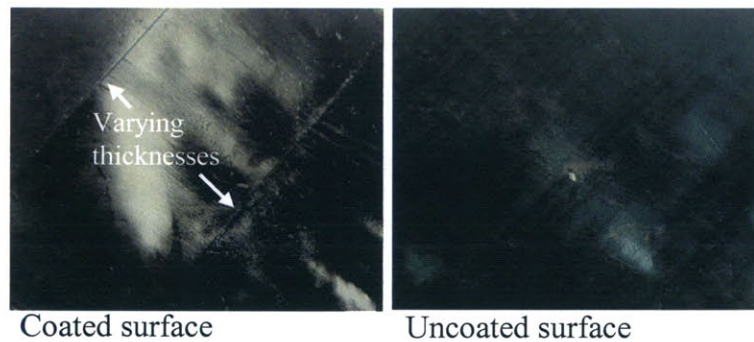

Coated surface   Uncoated surface

Figure 4-13. A photograph of the polymer after it was cast in the step mold shows the coated and uncoated surfaces of the film.

Figure 4-14 shows the results of the patterned mold, raised and lowered texture is evident on the surface of the coated side of the polymer. Because the patterned molds were intended to leave uncoated surface area measurements of conductivity were performed between open sections. While the results of these tests indicated that electrical connection could be made with the surface of the polymer film, it was difficult to

measure a reliable value. This is most likely due to very thin or uneven coating in the open sections of the lattice.
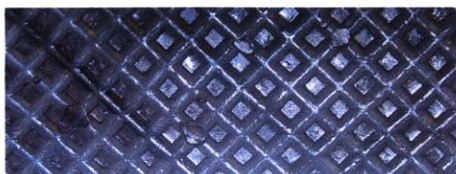

Figure 4-14. A photograph of a polypyrrole strip after it had been cast against the patterned mold.

In order to explore what sort of adhesion occurred between the two materials the sample was cut and photographed in the SEM. In Figure 4-15 a urethane/polypyrrole sample is shown; the conducting polymer is the thin feature along the bottom of the layered cross-section. The close adhesion between the two materials is evident as the elastomer follows the features of the conducting polymer perfectly along the cut.
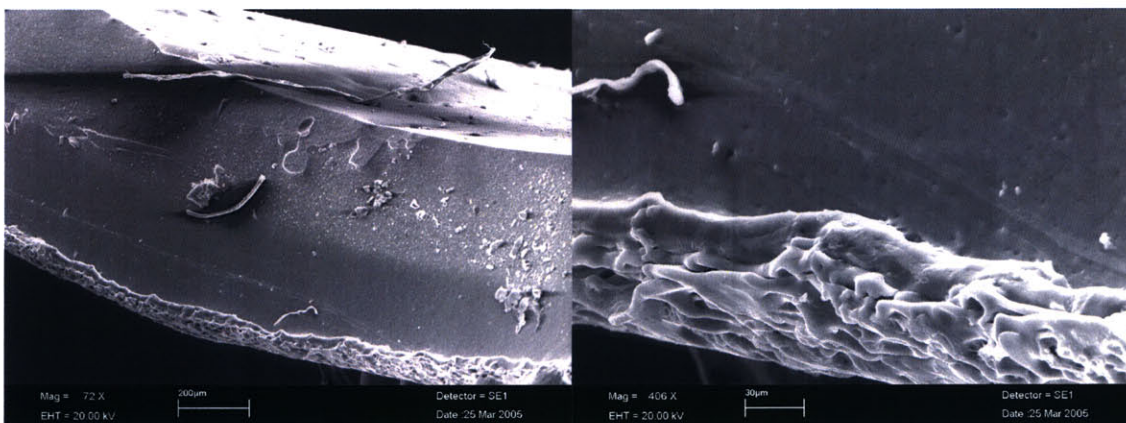

Figure 4-15. Urethane was cast against a prefabricated conducting polymer film; sample was sliced and adhesion between the two materials was photographed with SEM (scanning electron microscope) at 72× and 406× magnification.

During active testing of these cast polymer/elastomer films, separation would sometimes occur at the voltage application site. The photographs shown in Figure 4-16 expose the faces between the conducting polymer and urethane. The separated feature shows that the attachment between the films is not based on intervention or absorption between the conducting polymer and the elastomer as the urethane follows the features of the film perfectly but do not appear to leave a residue or show any disruption when separated.
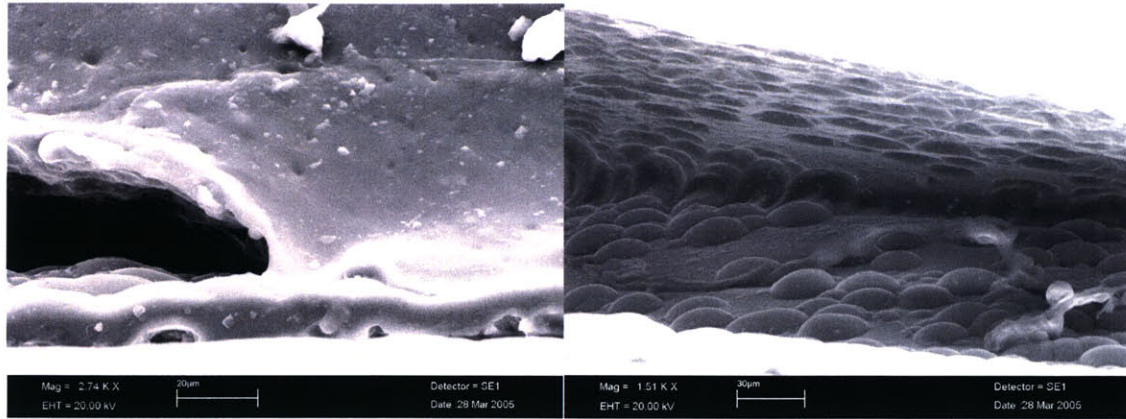
Figure 4-16. The separated urethane and conducting polymer films (left at 2740× magnification) show the surface adherence that occurred during casting in the texture of the underside of the elastomer (right at 1510× magnification).

In the bird's eye view of the film shown in Figure 4-17 the conducting polymer can be seen through the urethane film at the sight where separation between the electrical contact sight and the portion of the polymer that was expanding and contracting. This separation effect should be studied in further detail, but it is another level of detail illuminating the cohesion between the urethane and polymer surfaces as the SEM detected the conductive polymer through the insulating layer of urethane covering it.

Polypyrrole is visible beneath the surface of the urethane

Where separation occurred at the electrode attachment site, the polypyrrole can no longer be resolved by the SEM
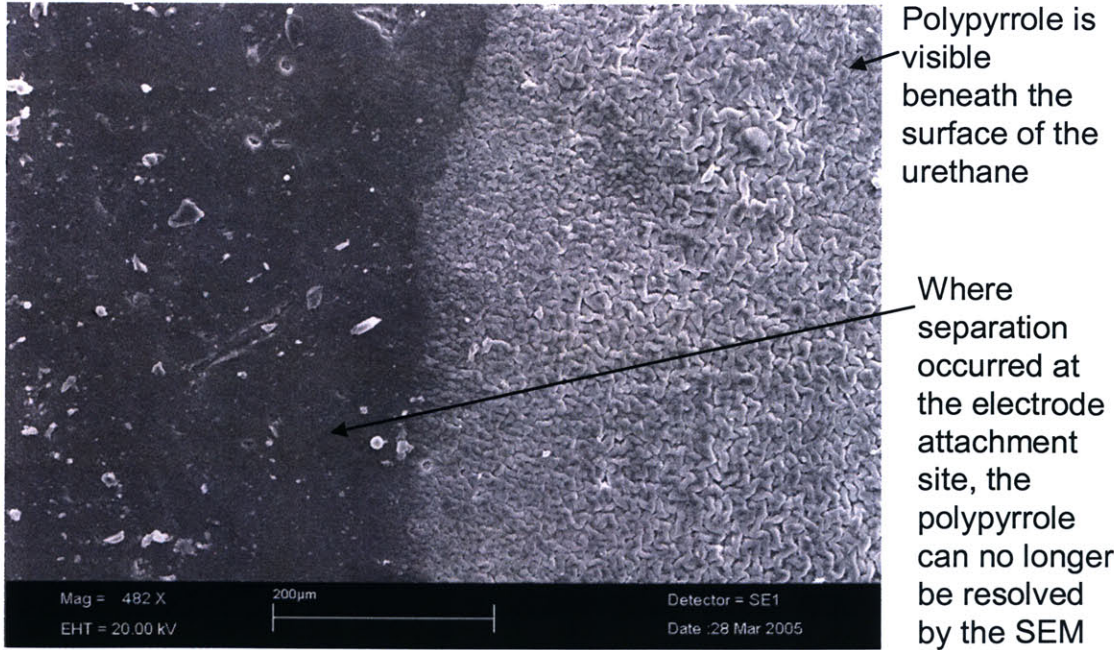
Figure 4-17. A bird's eye view of the urethane reveals conductive surface of artificial muscle film beneath the surface of the elastomer.

Active tests of the films coated with a solid surface of urethane were performed on the DMA. The results of these tests were very encouraging as the actuators yielded high strains under a simple sign wave voltage application. The strain amplitudes are expected to be significantly less than the values reported in Chapter 2 as the actuators were driven without the resistance compensation. In Figure 4-18 two of the coated strips were tested at ± 2.5 V versus Ag/AgClO$_4$ at frequencies of 0.1 to 0.5 Hz. The strain amplitudes and stresses were well within a usable range especially given the lowered response associated with this driving signal.
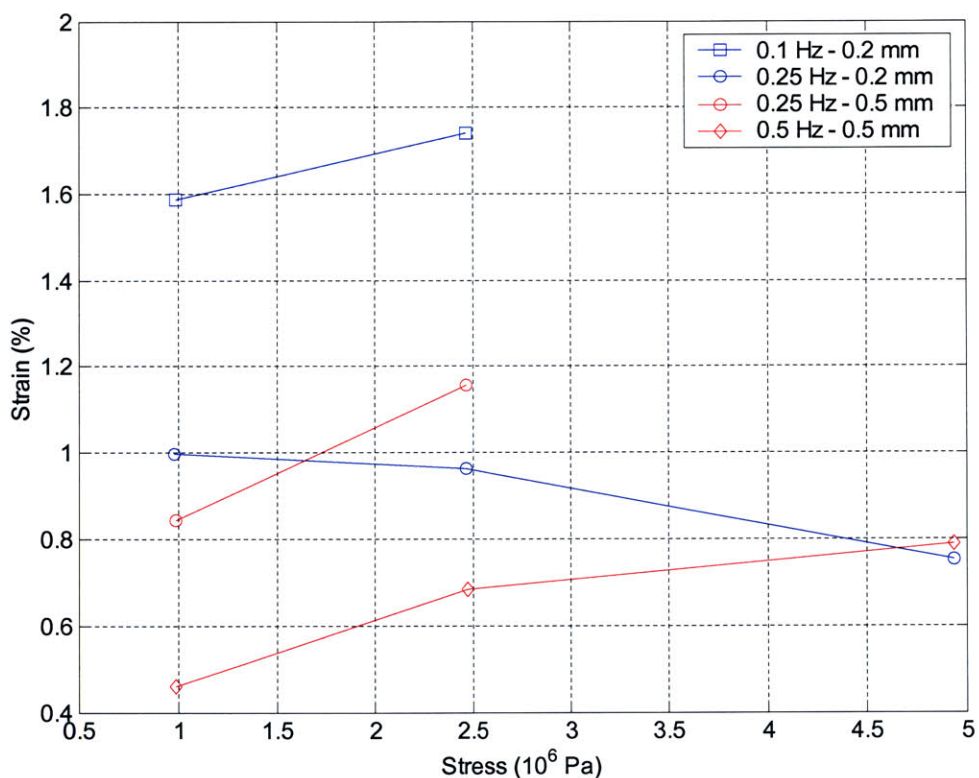
Figure 4-18. Actuation properties for 0.2 mm (blue) and 0.5 mm (red) thickness urethane coated films tested at various frequencies exhibited promising results for their incorporation into an active film.

In Figure 4-19 the thinly coated film was compared to an uncoated film from the same original sample of polypyrrole. These tests were performed at ±2.5 V versus Ag/AgClO$_4$ at frequencies of 0.1 and 0.25 Hz. The strain output of the coated actuator exceeds the plain sample by a minimum of 25 % indicating that the coated film outperformed the

uncoated sample. This increase in performance could be associated with the resonance of the urethane but should be explored further.
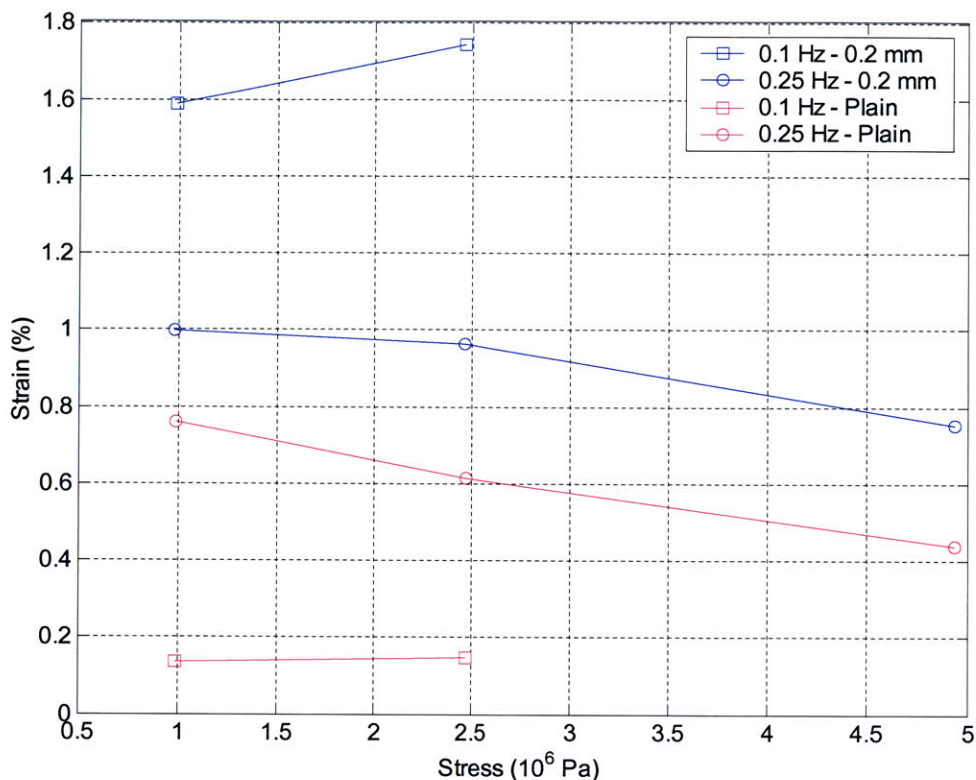

Figure 4-19. A plain strip and coated strip of polypyrrole from the same original batch were actuated at ±2.5 V versus Ag/AgClO$_4$ at frequencies of 0.1 and 0.25 Hz. The strain output of the coated actuator exceeds the plain sample by a minimum of 25%.

4.3 Chapter References

1. Boothroyd, G., Assembly Automation and Product Design. Marcel Dekker, Inc.: New York, NY, 1991.

2. De Rossi, D., Della Santa, A. and Mazzoldi, A. Dressware: Wearable hardware. Materials Science and Engineering C . 1999; 7(1):31-35.

3. Madden, P. G. Development and Modeling of Conducting Polymer Actuators and the Fabrication of a Conducting Polymer Based Feedback Loop, Ph. D. Thesis. Cambridge, MA: Massachusetts Institute of Technology: 2003.

4. Spinks, G. (University of Wollongong). Letter To: Peter Madden. 2002 Jan. Recipe for Manufacturing Conducting Polymer Strain Gages.

5. Whitney D. Mechanical Assemblies: Their Design Manufacture, and Role in Product Development. Oxford University Press: Oxford, UK, 2004.

5.0 Mechanical Model of Artificial Pectoral Fish Fin

A mechanical model of the pectoral fish fin was built to serve as a link in the chain of development between biological data, hydrodynamic analysis, and the realization of a comprehensive kinematic/kinetic model. The design was based in the casting/molding methods, explored in Chapter 4, as a way to develop the construction techniques for co-fabrication in parallel with the mechanics required for a biorobotic pectoral fish fin. The eventual goal of the mechanical model was to contribute to an understanding of pectoral fin swimming such that a comprehensive computational model can be implemented.

One of the common pitfalls of biologically inspired design is to attempt to copy nature. While a detailed understanding of the physiology and kinematics of biological locomotor systems is essential in developing a comparably functional device, the systems we are analyzing are amazingly complex. This complexity is what has traditionally prohibited the achievement of equally performing mechanisms. The challenge occurs at two levels. Primarily, classic mechatronic technology is far too cumbersome and inefficient. Parts in the system are only able to perform singular functions forcing the incorporation of multiple devices to accomplish what nature might with a single element. Each connection carries with it its own hardware, friction, stiction, backlash, vulnerability to wear, etc. The second issue is that all the elements in a biological system are not optimized for the accomplishment of motion or manipulation, as living creatures their bodies are also designed to feed and reproduce. Biological systems contain elements and features that are unnecessary in a bioinspired robot. Nature is also bound by parameters of evolution that do not require absolute optimization as much as the survival (Full, Lauder). While this produces incredible performance, it may not produce the best. A good example of this might be seen in aircraft technology. While the flexible wings of birds are currently being studied for their high performance ability when it comes to maneuverability, birds are limited in their power output in a way that modern aircraft are not.

Fin anatomy and kinematics of the Bluegill Sunfish were studied at the Lauder Lab at Harvard. Using what was learned from the natural system a distilled physical model was designed with the intention of capturing the fundamental functionality of the fin. The model was built and basic swimming maneuvers were implemented. The current model is actuated using standard servo motors in order to speed development time. However, artificial muscles will be incorporated into subsequent designs.

5.1 Design Parameters

5.1.1 Pectoral Fin Anatomy

The fin of a Bluegill Sunfish has a typical anatomy for ray-finned fish. When dissected and stained such that cartilaginous tissue shows in blue and bone in pink, the complex skeletal anatomy can be seen (see Figure 5-1). A pectoral girdle supports small hourglass shaped radials (Figure 5-1 (A) and (B)). A long arced cartilage pad sits between the radials and the fin rays offering support between the two bone sets (Figure 5-1 (B)). Although in the figure it may appear as though the base of the rays is embedded in the cartilage pad, it is actually resting over the surface. Figure 5-1 (C) shows the distinctive structure of the base of the first fin ray. Although the first ray has a particularly exaggerated contour, each fin ray has a uniquely shaped extruded process to which the tendons connect. Upon closer inspection, we find that there are many interesting features within the fin ray itself. The first of these features is known as bifurcation and can be clearly seen in Figure 5-1 (D); where the rays divide apart somewhat like a tree branch. The second feature visible in Figure 5-1 (D) is the bony segments of each ray. This feature is a little harder to see, but is well characterized (Lauder and Drucker, 2004; Geerlink, 1987; Lanzing, 2003).
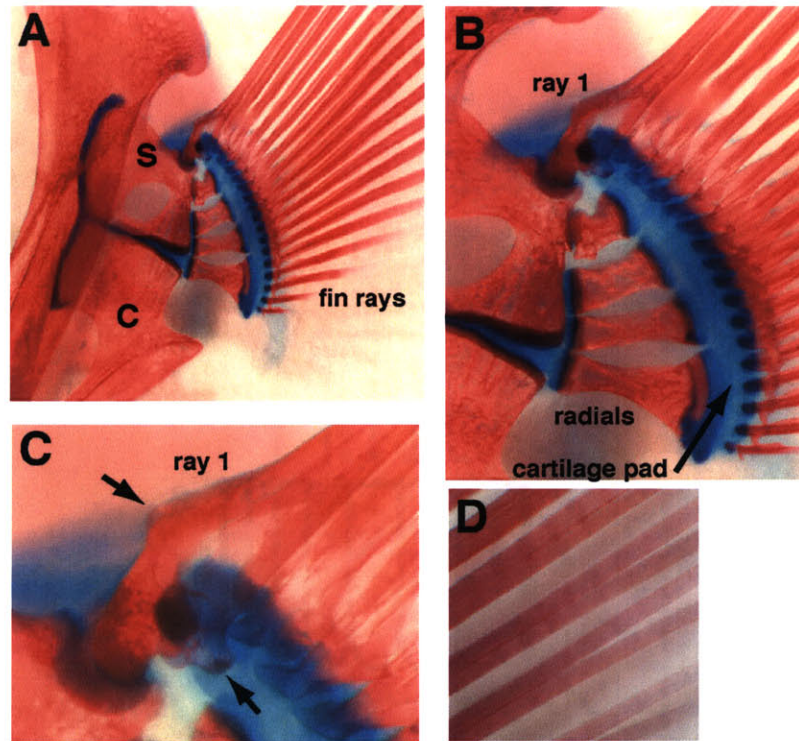
Figure 5-1. Pectoral fin anatomy of a Bluegill Sunfish shows the bone (stained pink) and the cartilage (stained blue). A: the pectoral girdle supporting the fin rays. B: small hourglass-shaped bones called radials articulate motion of the cartilage pad and the heads of the fin rays. C: distinctive processes extend from the fin rays for muscle tendon attachment; ray 1 has a unique shape as it connects to more muscle groups than any other ray. D: the fin rays branch distally bifurcating at the tip. (Copied from: Lauder and Drucker, 2004)

There is another very important structural characteristic of the fin rays not visible form the perspective in Figure 5-1. Each ray is split in half along its center, which is how the rays sit on the cartilage pad. They are not embedded in it as it may appear in the stained and dissected image in Figure 5-1. Figure 5 is a diagrammatic representation of the bony segments of the ray and the division between them. Each side of the fin ray is referred to as a hemitrichium and is a mirror image of the other. The hemitrichia are connected via transverse collagenous fibers. The fibers are elastic and therefore allow each segment of the hemitrichia to shear past one another. At their elastic limit, these fibers serve as a mechanical stop for the bending motion of the ray (Geerlink, 1987). This bending motion is discussed in further detail in the following section.
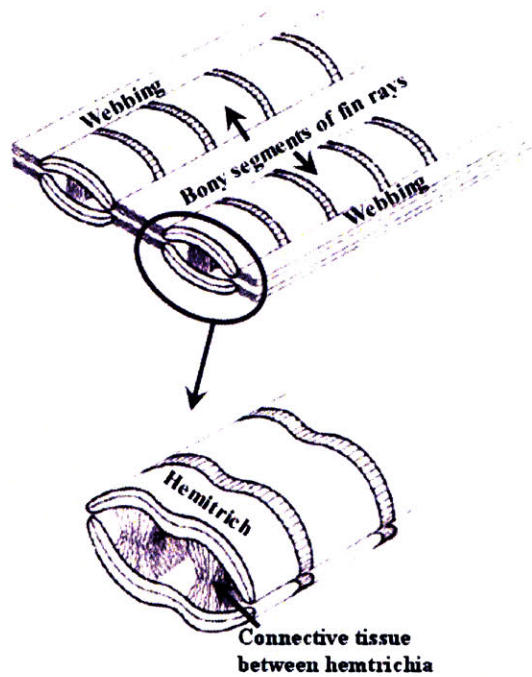
Figure 5-2. Cross sections of the fin rays show the two phases of the fin ray as they are joined by a connective tissue which travels down the center of the ray. The bony segments of the rays are also shown as they relate to the hemitrichia as well as the relative position of the fin webbing (Adapted from Geerlink, 1987).

As previously mentioned the hemitrichia saddle the cartilaginous pad. Figure 5-3 shows the ligament that connects to the hemitrichia at their base. The ligament provides support keeping the ray from being pulled over the cartilage pad when muscular activation occurs. Because of the smoothness of the ligament tissue the hemitrichium are able to slide vertically as shown (Figure 5-3).
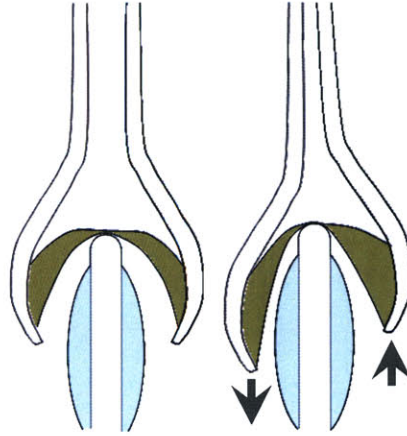
Figure 5-3. The hemitrichia rest on the cartilage pad connected at the base by a ligament shown in green. The ligament allows the hemitrichium to shift in the vertical direction while maintaining their attachment to the pad below.

Figure 5-4 illustrates the orientation of the muscular attachments in the pectoral fin. There are a total of 58 muscles activating motion across 14 fin rays. These muscles are classified into the abductor and adductor groups which attach to each fin ray shown in blue and green in Figure 5-4. Dissection of the fin musculature preformed in the Lauder Lab has revealed a distinct double layering of the abductor and adductor groups which is not shown. Each of these layers has separate discrete tendon attachment to the base of the fin ray. Each ray is therefore controlled by four separate lines of force. This muscular configuration enables a tremendous degree of control over the motion of each fin ray. There is one other distinct muscle group shown in red in Figure 5-4 this is the arrector group and is exclusively associated with the first fin ray in addition to the abductors and adductors (arrector dorsalis is not shown). These muscles have a distinct purpose and illustrate the critical role of the leading edge of the fin. The arrector group drives expansion (or spreading), acceleration and deceleration, and increases power in the dorsal/ventral motion of the fin. Kinematic analyses of fin movement shows that the first fin ray leads the remaining rays during the fin beat cycle (Lauder and Drucker, 2004),
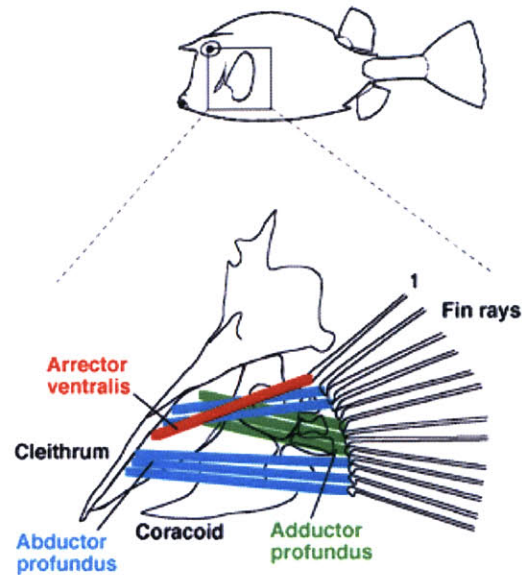
..

Figure 5-4. Illustration of the muscle groups found in the pectoral fin of a ray-finned fish. (Copied from: Lauder and Drucker, 2004).

5.1.2 Kinematics of Pectoral Fin Swimming

There are five distinct motion sets of the fin; 1) curl, 2) sweep, 3) spread, 4) cupping, and 5) fin reorientation. The pectoral fin's active ability to curl is one of the more striking features of its conformational control. Although not extensively studied, this feature of pectoral fin swimming is believed to be of critical importance in the manipulation of flow over the fin surface. In one study performed by P.J. Geerlink individual rays were actuated in a bending motion; their curvature, stiffness, and bending force were quantified. Figure 5-5 shows the results of one of Geerlink's experiments where he placed a differential displacement at the base of a fin ray observing the degree of bending as the magnitude of that displacement is increased. This is a simulation of the shift that would be caused by a contraction of the abductor versus the adductor muscle group. Geerlink made the observation from this data that the curvature of the fin does not occur evenly over the entire ray, but instead reaches a maximum at a median position where it is believed the maximum forces from flow over the fin's surface would also likely to be. Studies have shown that the curling motion is activated primarily at the beginning and the end of a stroke (McCutchen, 1970; Videler, 1975). This is also believed to be consistent with exertion of maximum force from the fin on the water at the moment where maximum pressure from the water on the fin is expected to be found (Geerlink, 1987).

The results of these studies seemed to suggest that fish are largely exploiting the curling motion as a means of tuning the stiffness of the fin.
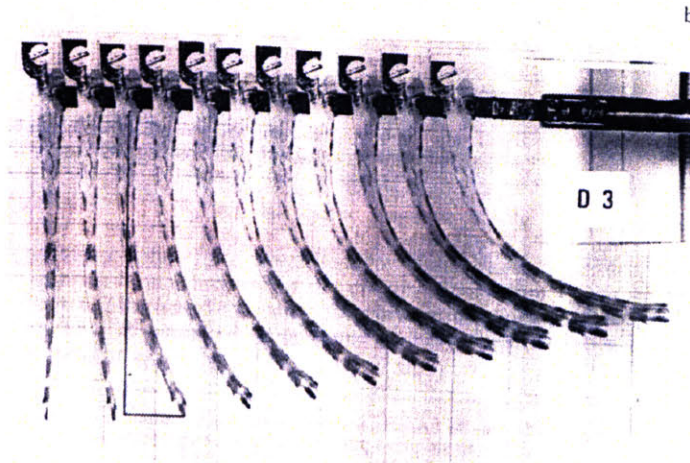

Figure 5-5. Fin rays undergo bending via a differential displacement exerted at the base of the fin. Curvature over the ray is not consistent but reaches a maximum at the mid region of the ray where it is believed the maximum forces exerted by the flow over the fin would occur (Copied from: Geerlink, 1987).

A diagram of the sweep, cupping, and spread vectors of motion are defined relative to the position of the fin is shown in Figure 5-6. As discussed earlier, the adductor and abductor muscles control the sweeping motion while the arrector muscles attached to the leading edge of the fin control a spreading motion between the rays. Spread occurs in the plane of the fin, while sweep is the stroke of the fin into and out of the flow. The cupping motion is shown in green in the figure and is like a pinching motion between the fin rays. This has the effect of diminishing the fin's surface area as the fins pull together, it is called cupping because the surface of the fin cups as the edges pull together.
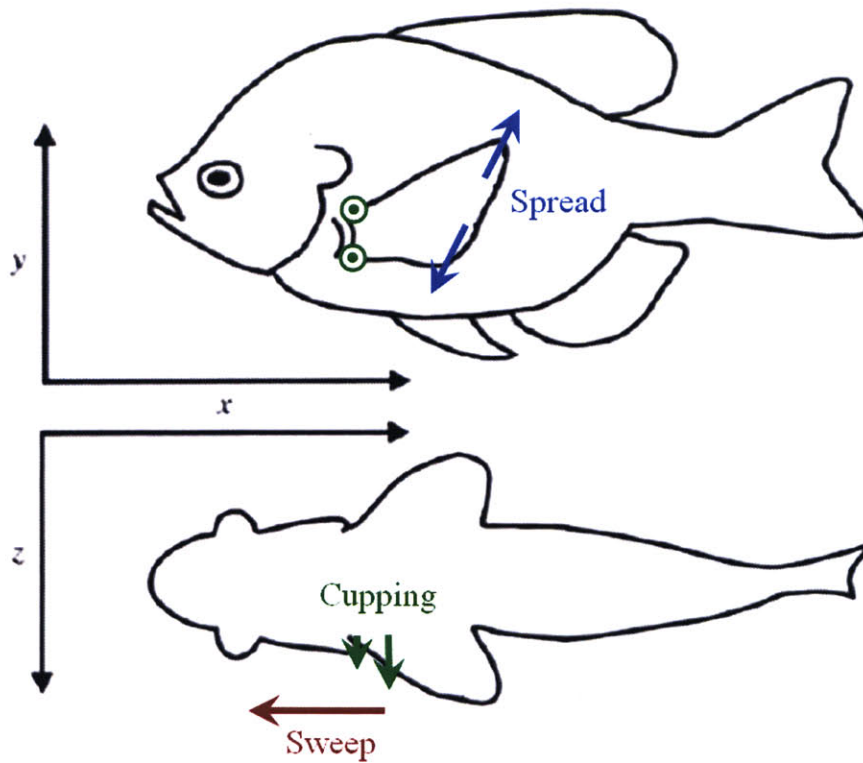
Figure 5-6 Sweep, spread, and cupping vectors are shown in relation to the flow stream past the body of the fish (Adapted from Lauder, 2004).

For the purpose of visually describing these motions further, animations of an idealized fin were developed in ANSYS (www.ansys.com) a finite element modeling software. However, these models are intended for illustrative purposes only, a real FEA model of the fin is still in development and not covered in the scope of this work. The interaction between the material properties of the fin rays embedded within the fin's web is beyond the scope of the solution capabilities of this software. Figure 5-7 shows the deformations of the fin in the spread (A), cupping (B), and curling (C) actuation modes.
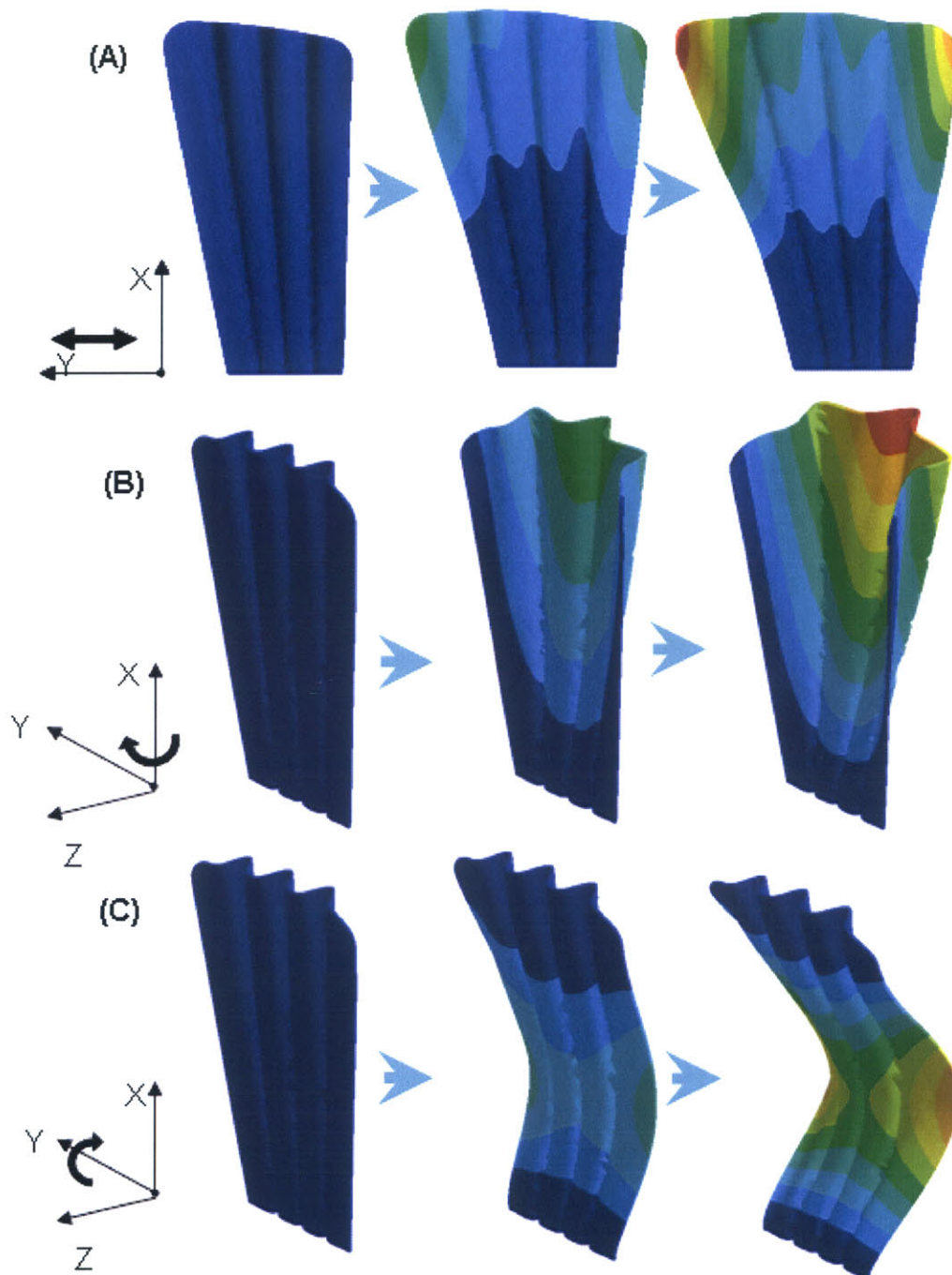
Figure 5-7. A visual demonstration of an idealized pectoral fin shows the modes of fin formation under spread (A), cupping (B), and curling (C) of the fin's surface.
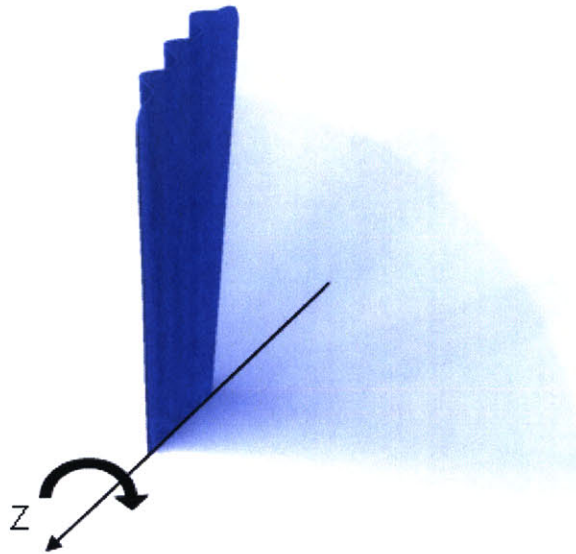
Figure 5-8. Sweep motion of the fin; a simple rotation of the fin into the flow past the body of the fish.

The fin does not deform during the sweep motion, it simply rotates into the flow in the manner shown in Figure 5-8. This is the simplest actuation mode. Of course, the real fin doesn't isolate these motions as they're shown here. A fish combines all of these motions to achieve refined control over the fin's surface in the water. Figure 5-9 shows a 3D digitized image taken from the fin of a Bluegill Sunfish during a steady swimming maneuver in the flow tank at the Lauder Lab at Harvard. The cupping, sweep, and leading edge control are evident in the fin's shape.

Figure 5-9. 3D digitized image taken from fish during steady swimming; cupping, sweep, and leading edge control are evident (Copied from: Lauder Lab). Blue arrows mark the direction of flow as well as the order in which the fin formations occur through the stroke.

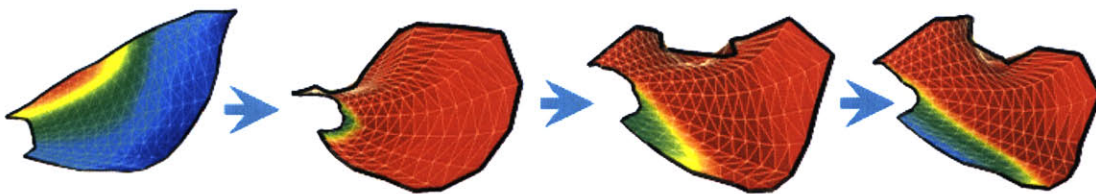Power and force requirements for actuating the fin were estimated from biological data and some basic fluid dynamic analysis. Measurements of the muscles taken during swimming revealed a dynamic range of 3 to 23 % strain. During steady swimming at a speed of 0.5 TL/s adductors averaged 6 % strain, the higher strains occurred when maneuvers were being performed. The force outputs are estimated at 100 to 200 mN on each ray (Gibb, 1994; Lauder and Drucker, 2004).

5.2 Compliant Mechanism Based Model of Pectoral Fin

The biological fin is far too complex to replicate and control with a reasonable design development time and the need for such intricacy is not apparent. In an effort to capture maximum functionality with minimum investment, several reductions were made architecturally and kinematically. Primary simplifications to the architecture of the mechanical model were as follows:

- Reduction of fin rays per fin,
- Reduction of actuators per fin ray,
- Exclusion of bifurcation of rays,
- Exclusion of bony segmentation of rays.

For the scope of this project, the following omissions to fin kinematics were made (although were not intended to be permanently removed from the final design):

- Exclusion of fin reorientation,
- Coupling of spread with sweep or curl activation,
- Cupping actuated across entire fin with a single actuator.

The other significant deviation from the fish fin was the change of scale. The design was scaled up by a factor of four from a nominally average sized specimen. The larger dimensions were easier to work with and potentially more useful when the fin is connected to a vehicle.

Because the fin is designed to be made using casting and molding techniques versus traditional assembly methods, joints and connections were accomplished using compliant

mechanism design features. This also has the benefit of keeping the structure efficiently small.

There were many design iterations as fabrication and kinemtic issues were resolved. Two versions of the fin that show characteristic phases of the design process are shown with the intention of discussing the strengths and weaknesses of the model.

5.2.1 First Generation Mechanical Model

The first design was mainly used to resolve molding and material issues. It provided a learning environment for testing material interactions, workability, and performance. The molding and casting process was also explored and many of the issues discussed in Chapter 4 regarding the soft and hard mold processes were discovered. Using living hinges has the benefit of decreasing the complexity of the mechanical model by part reduction, but increases development time as single elements of the model need to fulfill multiple functions.

Figure 5-10 shows the 3D CAD model of the first fin design. The basic structural elements are labeled as they were referred to during construction. There are two primary portions of the design: 1) the upper webbing and fin ray shown in yellow, and 2) the lower base shown in blue. The function of the base was to fulfill the function of the cartilage pad on a biological fin creating a post over which the rays can slide in the vertical direction. This is a necessary constraint in the realization of a curling motion. The base was also designed to provide a rotating joint. This lower portion also acts as method of clasping the fin for mounting which is why it was referred to as a handle.

Fin rays encased
in webbing

Webbing

Ray base joint

Cantilevers
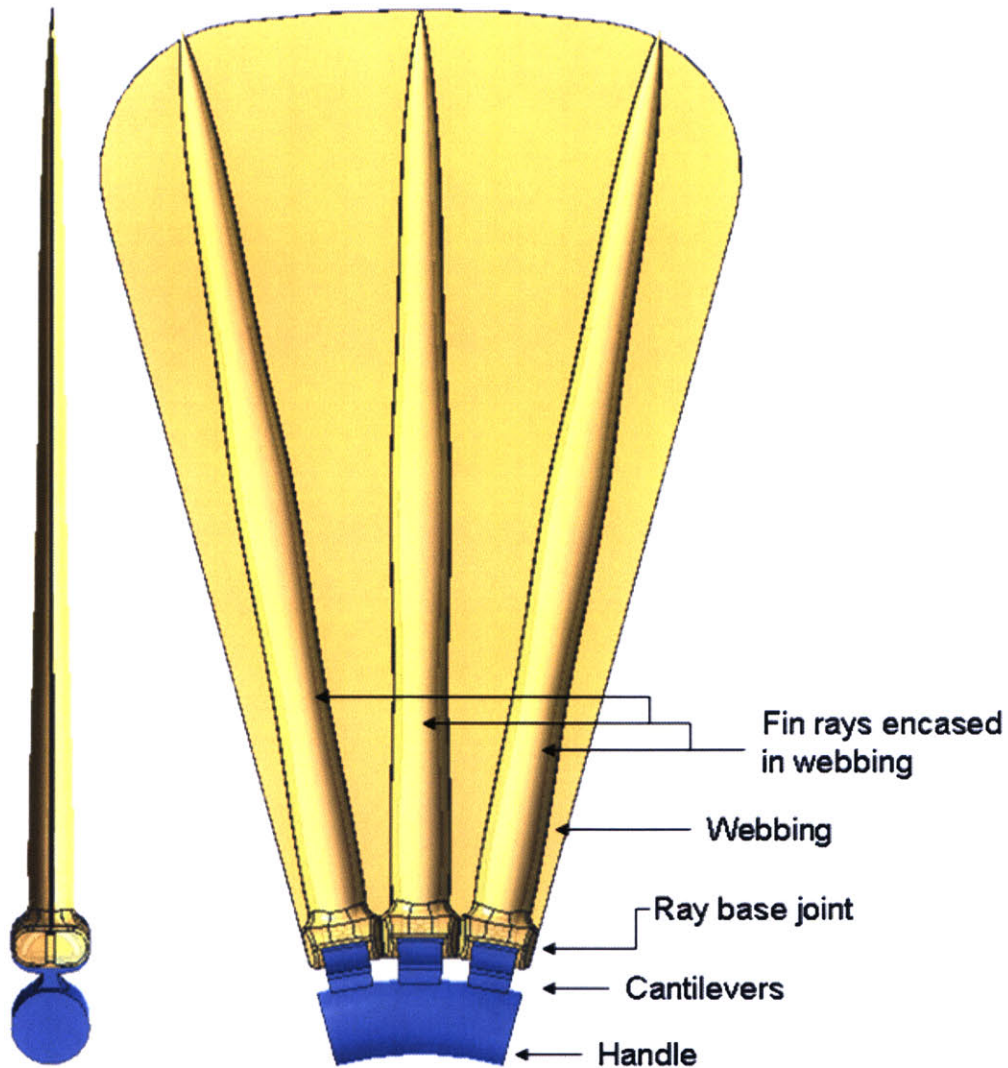
Handle

Figure 5-10. The first version of the mechanical model was greatly oversimplified; the web is flat and only three fin rays articulate motion. The two primary phases of the design: the web and fin ray (yellow) and the base handle (blue) are shown with prominent features.

The upper portion of the fin includes the webbing and fin rays. One of the modifications made for this iteration of the design was to work with a flat web. Because the web provides the control surface it is necessary to have maximum control over its shape and relative surface area. Certainly, a flat web severely limits these freedoms but was a sufficient beginning in resolving other mechanical and fabrication issues. In order to reduce mechanical impedances induced by having a thick web, it was made as thin as

possible given the workability of the elastomer and the mold. Generally, the thinnest web consistently achievable was 0.25 mm.

The rays were encased within the webbing material and were designed using geometries from a real fish. A Bluegill Sunfish was dissected and measurements were taken at six positions along the ray. These were imported directly into Unigraphics NX 2.0 and the ray shape was generated using the surface spline feature. Figure 5-11 shows the results of that operation. The rays were split along the center line; a necessary feature for creating the hemitrichia and active control over the curl of the fin. The side view of the fin in bottom of Figure 5-11 shows the fin ray as it is encased in a fine layer of elastic material that serves as the web.
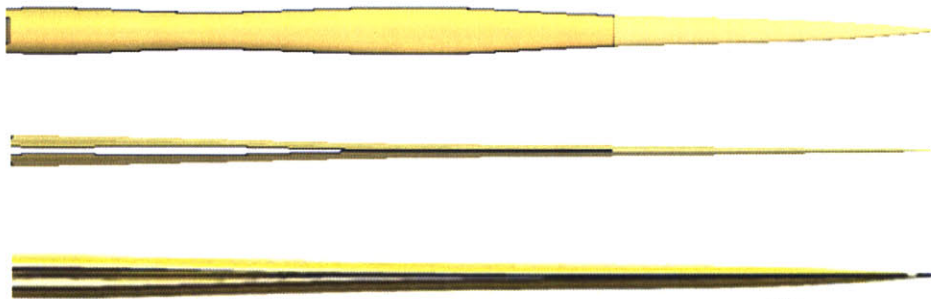

Figure 5-11. Fin ray geometries taken from a Bluegill Sunfish were modified only slightly and were printed with epoxy resin in 3D using the rapid prototyping stereolithographer. A side view shows the split line in the fin which defines the hemitrichia. The bottom side view shows the fin ray encased in the 0.250 mm thick web.

The spread and sweep motions were actuated through expansion and rotation of the cantilevers on the base as shown in Figure 5-12. The base material was cast in a 50 to 60 durometer urethane with a 450 % elongation at break and a tensile strength of 3.5 MPa (see Appendix A). The web extended over the base creating a surface bond between the fin and the cantilevers. Figure 5-13 shows a slightly transparent view of the web as it sat on the cantilevers. The rays can be seen beneath the surface of the webbing material.
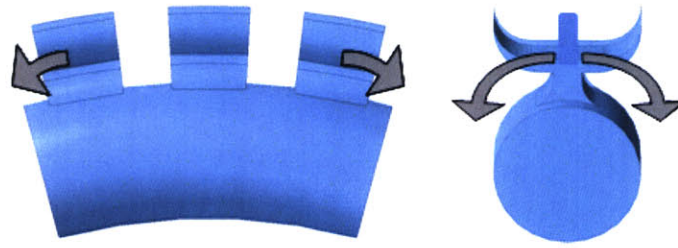
Figure 5-12. Supports at the base of the fin rays are flexible allowing the fin rays to sweep and spread as the cantilevers expand (left) and rotate (right).
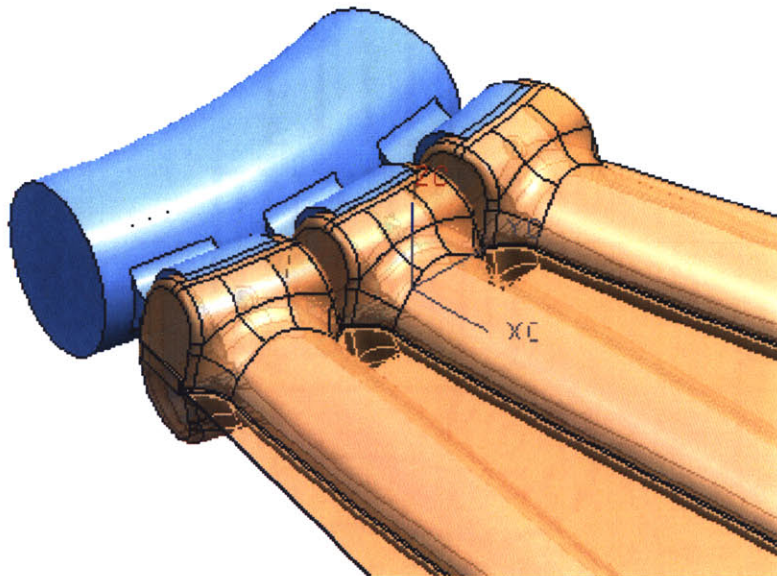
Figure 5-13. A close-up view of the fin rays as they are supported by the webbing and the cantilevers.

Tendons pull from the base of the fin rays to actuate multiple degrees of freedom; in the fish's fin the rays' bases have bony processes which extend from the ray creating a moment arm from which forces are applied. In the mechanical model the tendon attaches through a hole in an arc at the base of the ray as shown in Figure 5-14. The arc in the base of the ray was intended to aid the line of motion of the ray as it passed over the elastomer pad shown in grey. The vertical process which sits in between the two hemitrichium was molded in the same material as the cantilevers, the durometer of this material and the tensile strength were generally 1/3 greater than the web (depending on the material used). The curl actuation scheme involved applying a differential force to the two blue tendon lines shown in Figure 5-14.
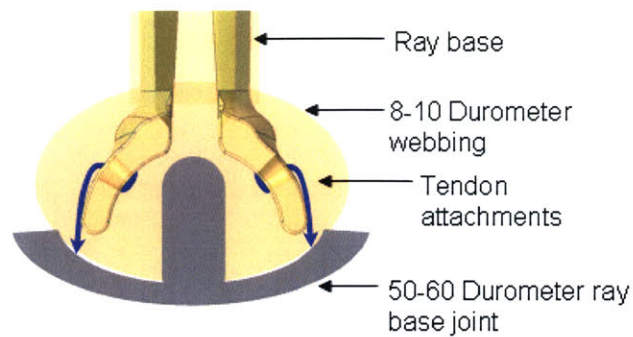
Figure 5-14. The connection between the web and the base; tendons attach through holes in the fin rays and pull through the elastomer web.

The fin was taken to a flow tank at the Lauder Lab at Harvard as shown in Figure 5-15. Using a hand operated force scale, called a fish scale, tendons were pulled with 5 N of force into a flow of approximately 0.3 TL·s^{-1} and were successfully able to withstand the flow. Figure 5-15 shows the fin as it was mounted in the tank. The results of this test were promising in that the forces were in an appropriate range for the conducting polymer actuators. This indicated that the choice of material properties in the elastomer based structure were suitable for the desired flow rates as well as the active properties of the artificial muscles.

Figure 5-15. First generation of fin is suspended in the flow tank at the Lauder Lab at Harvard. Tendons were pulled into a 0.3 TL·s^{-1} flow with 5 N of force.

The problems with this version of the design were mostly associated with the modifications made to increase ease of fabrication. In general this flaw was a matter of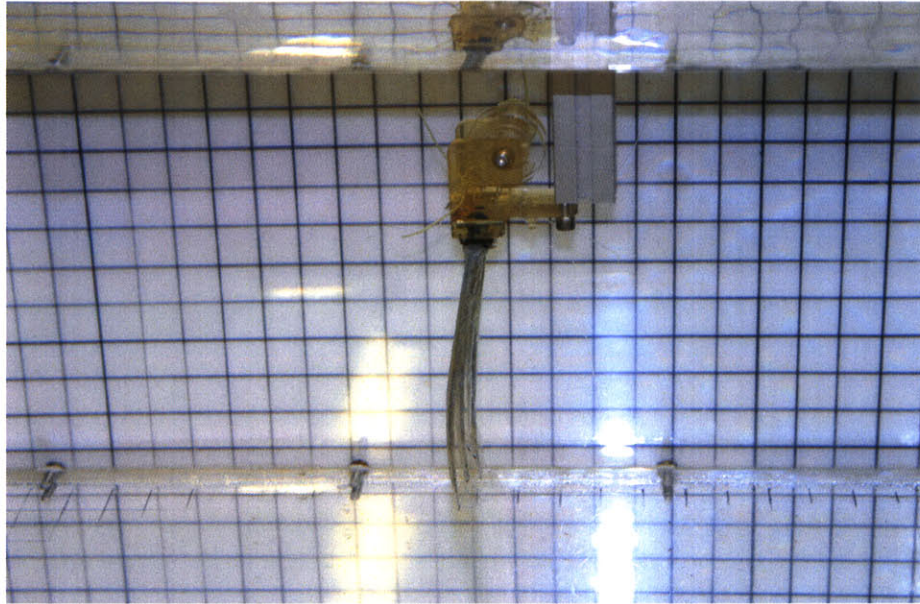 oversimplification. The flat web severely limited the ability to modify the fin's surface area since spread articulation is mechanically impeded in the stretch of the webbing material. Only three fin rays articulated motion; which was just enough to actuate leading edge control, curl, and sweep. However, three fin rays limit the degree of control over surface area during a stroke, as well as the shape of the fin during cupping.

There was significant difficulty in attaining curl actuation with this design. Some likely contributors to this problem involved conflicting design constraints. The first was a substantial error in the design of the ray base joint. Bonding the ray to the base joint within a capsule of webbing material created mechanical impedance of the vertical shift necessary for bending. The original idea surrounding this design choice was to provide support and placement between the ray and the cantilever. It was believed that the relative softness of the webbing material would mitigate the mechanical impedance it introduced. The second significant conflict involved the design of the cantilever. While these bending beams were meant to provide a sweep and spread articulation, they were

also supposed to provide vertical support under the application of a differential force on the hemitrichia. The beam is therefore required to be stiff in the vertical direction and flexible in bending. Unfortunately, there were problems with the beam buckling under the application of force at the tendons. Figure 5-16 shows the associated failure modes.
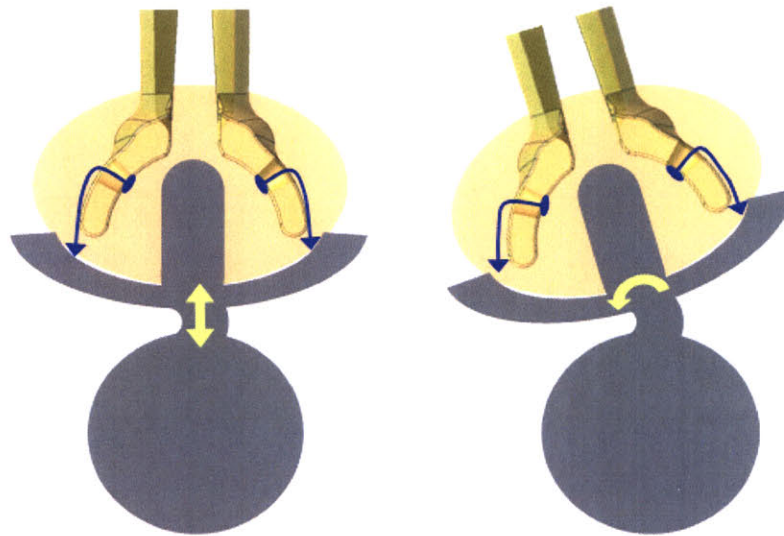
Figure 5-16. Cantilevers buckle under application of force on the tendons.

5.2.2 Second Generation Mechanical Model

In the second generation of the fin design several problems were corrected. Improvements to the design also arose from a greater understanding of the molding and casting process. The first significant improvement to the design was the incorporation of a curved fan-like webbing. This curvature in the web allows for greater spread of the surface area of the fin. Controlling the active area of the fin enables the fish to manipulate the magnitude of force on the water. Figure 5-17 shows the current form of the mechanical model. Another immediately apparent change in the design is the incorporation of a fourth fin ray. The fourth ray was intended to increase control over the conformation of the fin's surface.

Curved web surface

Four fin rays

Detachment between
web and base

Changed base design
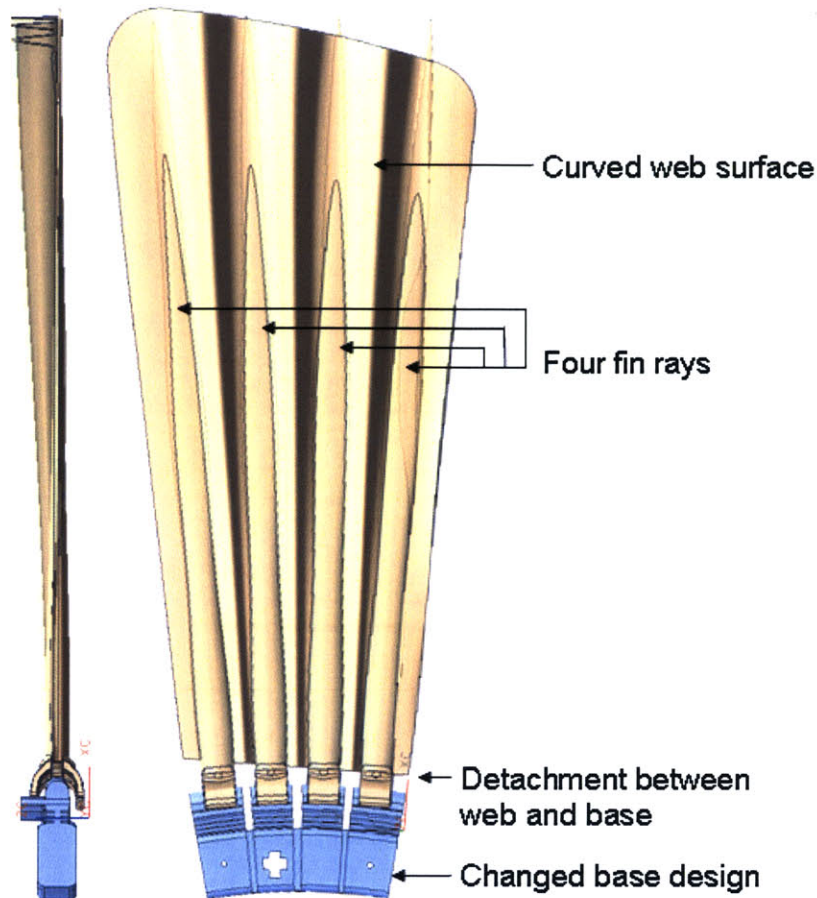
Figure 5-17. The fin design was modified with added features including a curved web, an extra fin ray, detachment between the web and the base, and a significantly changed base.

The interface between the web and the base was removed completely. Connecting these two elements in a fused joint was problematic in the first model and was actually superfluous. Since the tendons pull the rays down toward the base, there is no need for a solid attachment between them. Placement is achieved via a compression alignment and a slot through which the tendon passes in the base.

Some changes were made to the fin ray base structure that helped to better constrain them during actuation, increase the actuation of the spreading motion of the fin, and implement a bending moment by applying a force couple. Figure 5-18 shows the new details of the ray's base design. The new features include an added hole at a higher position on the ray, a slot along the bottom, and the eccentric placement of the two holes.

Figure 5-18. The ray base was modified with the addition of an extra hole, eccentric placement, and a slotted extension at the bottom.

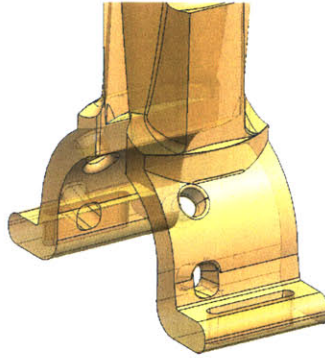Figure 5-19 shows the lines of force as they're act through the ray base to actuate spread, the vertical shift for bending the ray, as well as the rotational force for the sweeping motion. In Figure 5-19 (A) the tendon attachment at the eccentrically located position at the base creates a moment about the center line of the cantilever on which it rests. This actuates the spreading motion as the compliancy of the slotted cantilevers is exploited in order to achieve bending in the lateral plane of the rays. The two holes are stacked vertically and threaded in the manner shown in Figure 5-19 (B) in order to provide articulation of a force couple at the base of the fin. This way the vertical shift required to achieve bending is directly applied with a single actuator. The sweeping motion of the fin is actuated via tendon attachment as shown in Figure 5-19 (C) and was generally the same tendon used to achieve the spreading motion in Figure 5-19 (A). Because only two actuators were used per fin ray to achieve these three degrees of freedom, some coupling was necessary. The slot at the base of the ray enabled actuation of sweep without applying a spreading motion. This increased flexibility during actuation tests to explore the minimum actuator requirements. Any reduction in complexity is essential to the successful design of a biorobotic device. Tests are still being performed on whether the current reduction of more than half of the actuators per fin ray and less than half the total fin rays per fin are still under way.
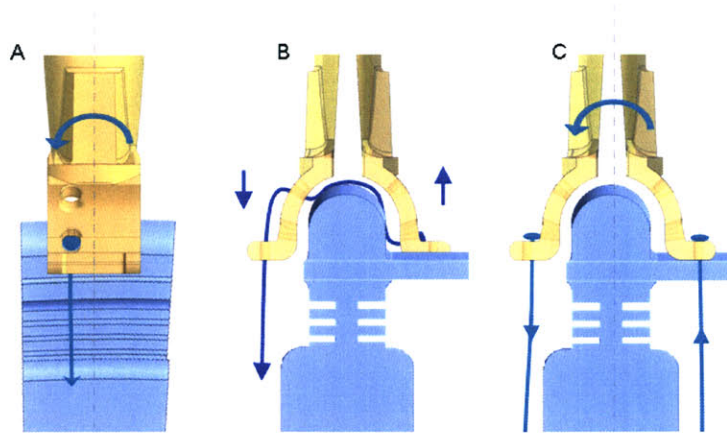
Figure 5-19. Tendon connections on the base of the ray are shown as they apply (A) spread, (B) bending motion, (C) and sweep.

The modified ray base design was tested in air in order to verify whether curl could be actuated with the modified tendon attachments. Figure 5-20 shows the results of this test. The fin rays showed significant bending with relatively little sweeping motion. This was a positive result not only because the curling motion had been properly constrained for actuation, but also because it was now possible to decouple the curling and sweeping motions.
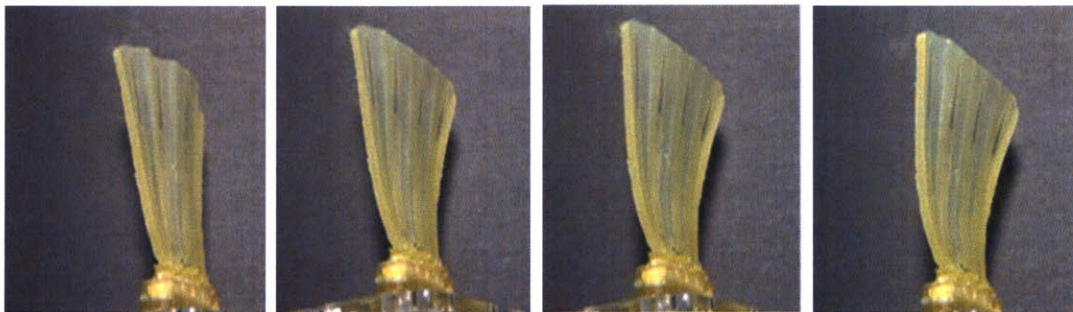
Figure 5-20. The new tendon attachments on the base of the fin rays were tested in air verifying that the new architecture properly constrained curling actuation.

Further design adjustments in the current fin design included changes in the geometry of the handle of the fin. Figure 5-21 shows the adjusted features which include:

- a keyed feature for clamping the base without interfering with cupping motion,

- grooves or slots in the base which increase the compliance of the base in cupping without compromising the structural stiffness in the vertical support of the rays,

- thicker cantilevers,

- horizontally oriented slots in the cantilevers,

- supports for the rays are only on one side of the base and are not bonded to the web.
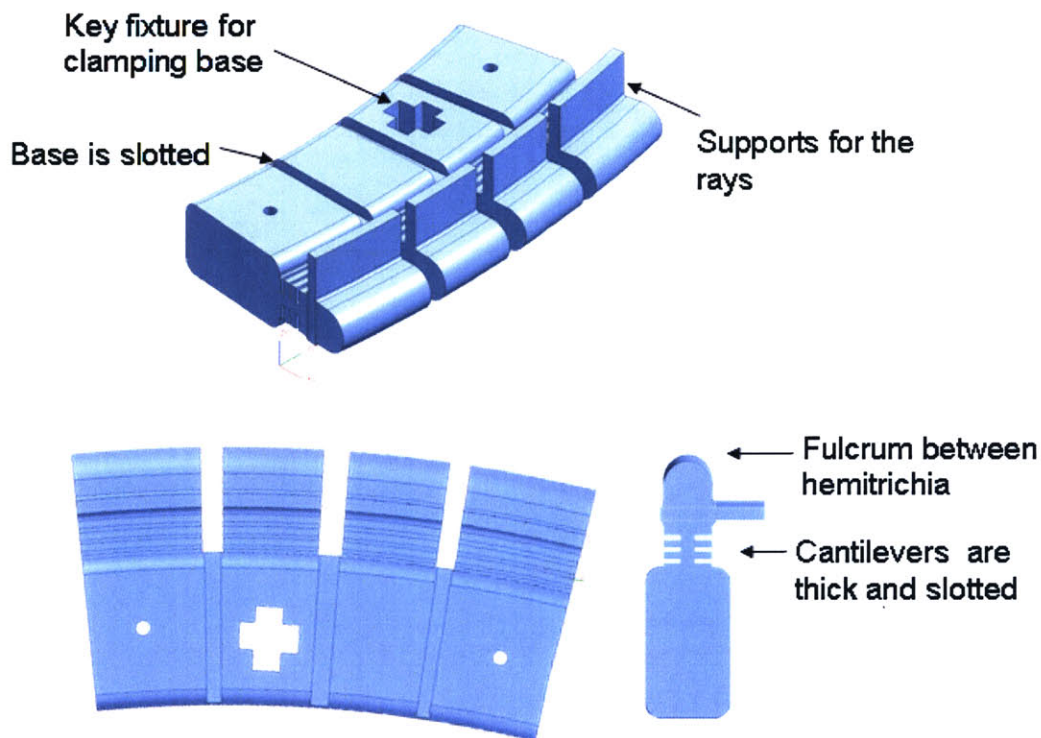
Figure 5-21. New features on the base of the fin include an adjusted support structure, a keyed hole for clamping, slots in the base for coupling, and cantilevers are thicker with added grooves.

The slots in the cantilevers increase compliance in rotation while increasing resistance to buckling. The relationship between the critical force on a beam, F_{cr}, is given by:

$$F_{cr} = \frac{EI\pi^2}{L^2}.$$

5-1

where the Young's modulus of the material used to make the column, E, and the moment of inertia, I, and the length of the cantilever, L, are related. Resistance to buckling is

inversely proportional to the square of the height of the beam. The slots in the column create a stack of short cantilevers that can withstand greater force before failing in the vertical direction without compromising the bending required for sweep actuation.

The second generation fin was taken to the flow tank at the Lauder Lab at Harvard. Immersed in a 0.5 to 0.55 TL/s flow rate a steady swimming, strong side, *and weak side* maneuver were actuated. Servo motors were used for this model as they are simple to use enabling rapid development time between design iterations and actuation control. Footage taken during the swimming maneuvers were freeze framed and included for the steady swimming and strong side maneuvers. Unfortunately the only footage of the weak side maneuver is a front view and difficult to interpret in a freeze frame, which is why these results are not included here.

Steady Swimming Maneuver

A steady swimming maneuver simply involves the simultaneous sweep actuation of all the fin rays with equal amplitudes and zero phase shift on each fin ray. Figure 5-22 shows the fin as it completes half a complete stroke cycle for a steady swimming maneuver at a flow speed set to 0.55 TL·s^{-1} and actuating at 0.5 Hz. The fin is clearly exerting a significant amount of force on the flow as can be seen in the large cone of water shedding from the surface of the fin ray. This was the fastest speed implemented in the flow tank.
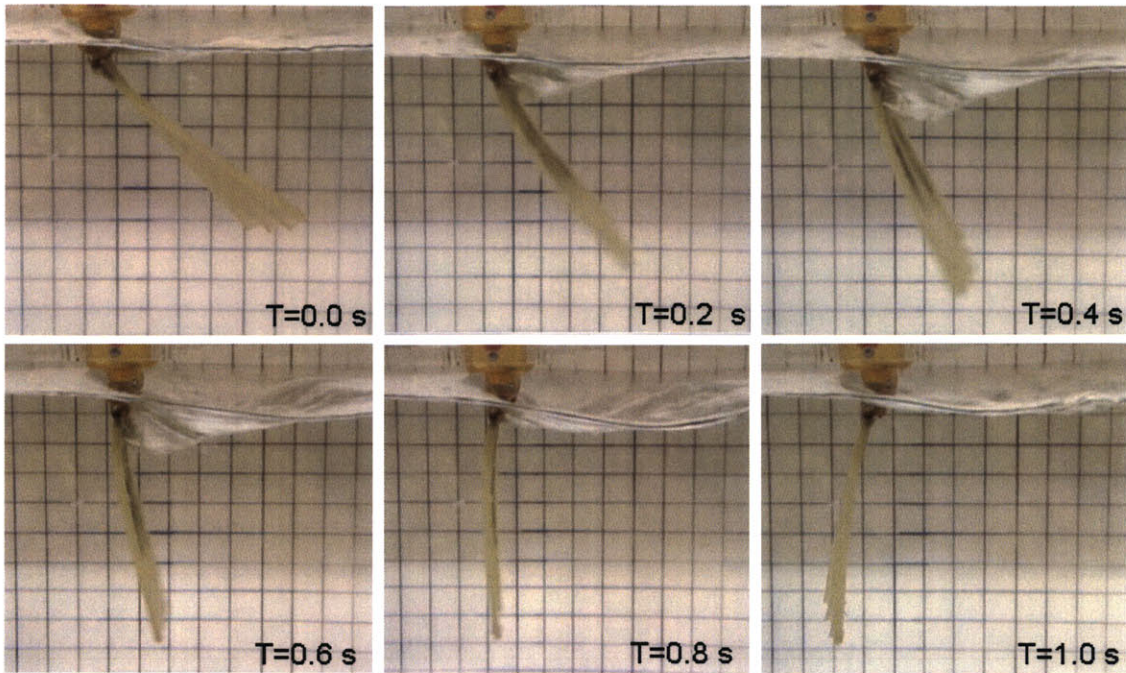
Figure 5-22. The fin was actuated to perform a steady swimming maneuver in a flow of 0.55 TL·s^{-1} at 0.5 Hz.

One very interesting result was discovered when the fin was actuated with and without the curl motion during a steady swimming maneuver at 0.5 TL·s^{-1} actuating at 1 Hz. Figure 5-23 shows the freeze frame for one complete cycle of the fin performing steady swimming without the curling motion. There is not vortex shedding apparent in this series. Referring to the tendon attachment configuration as it was shown in Figure 5-19, it is important to note that the fin is being controlled with only one motor when only the sweep motion is being actuated. Figure 5-24 also shows the results for one complete cycle and is radically different in the range of motion and the vortex shedding off the fin's surface. The increase in performance is partly due to an increase in power generated by the second set of motors, but the increase in stiffness on the fin also appears to have a significant effect on its performance.
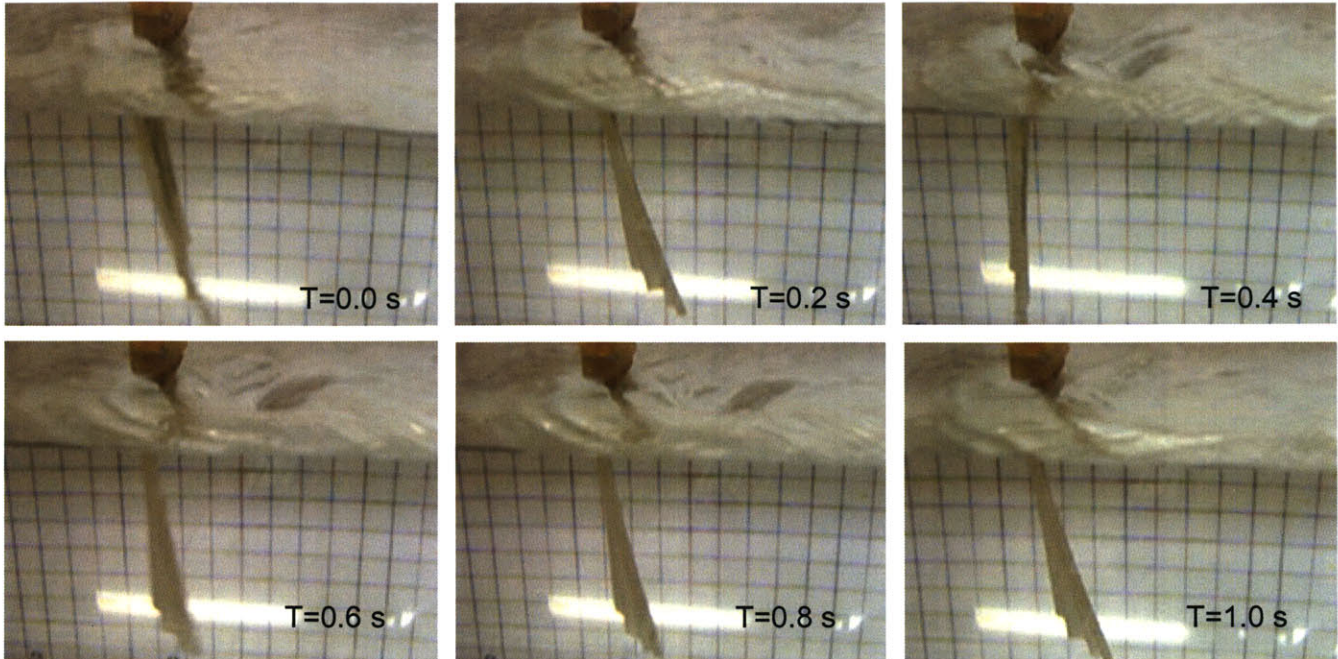
Figure 5-23. The fin is actuated at 1 Hz in a flow of 0.5 TL·s^{-1} with curl actuators off. The vortices being shed from the fin are almost non-existent there is also a limited range of motion.
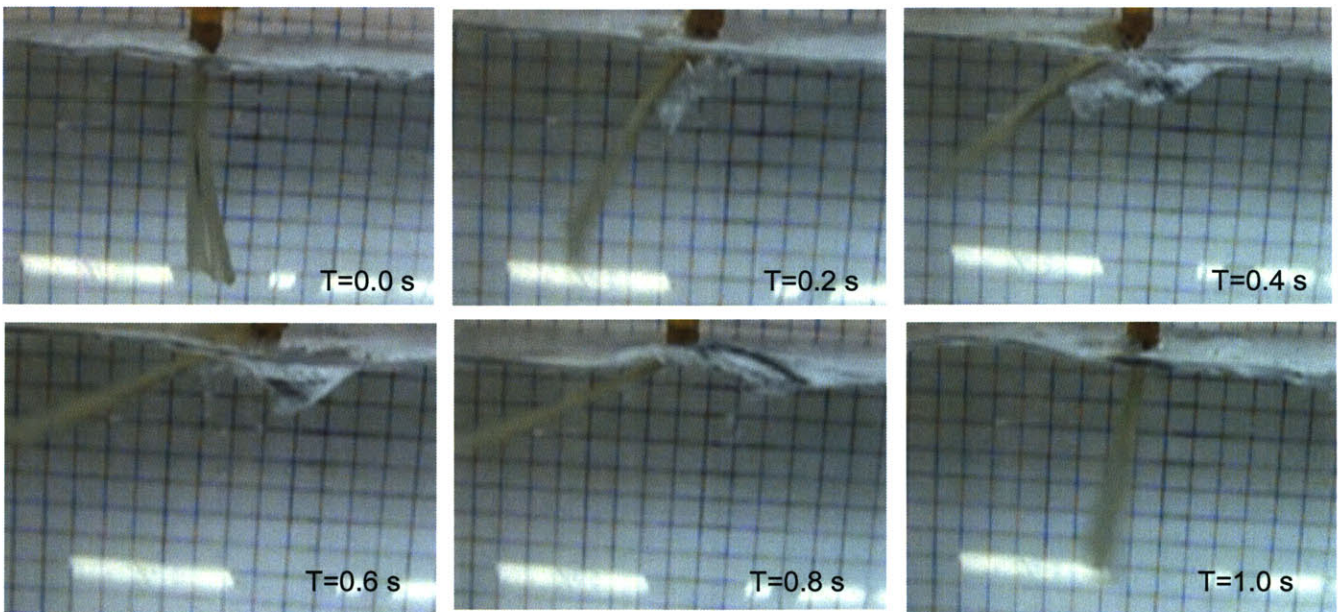
Figure 5-24. The fin is actuated at 1 Hz in a flow of 0.5 TL·s^{-1} with curl actuators on. Vortex shedding off the surface of the fin is dramatically increased as well as the range of motion.

Strong Side Maneuver

In Figure 5-25, the fin is shown as it completes a full cycle during a strong side swimming maneuver. A strong side maneuver is the reaction of the pectoral fin when executing an evasive maneuver in the direction of motion of the fish. The four rays are being actuated with a sine wave 30 degrees out of phase with 20 % smaller amplitude from the first to the fourth ray.
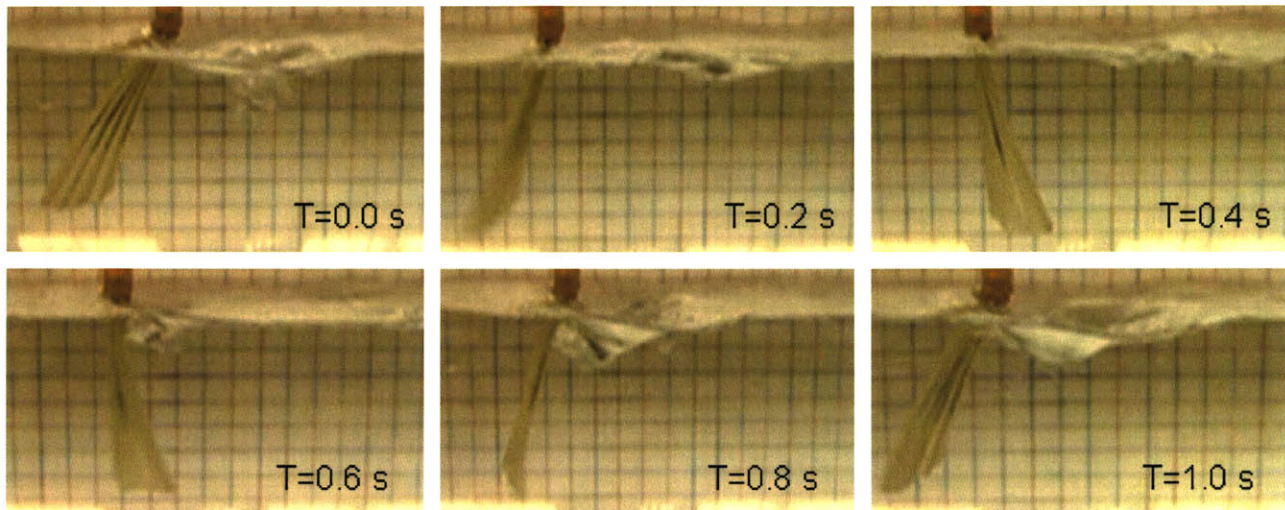
Figure 5-25. The fin under a strong maneuver command function; each fin is out of phase by 30 degrees and 20% smaller amplitude from the first to the fourth ray

5.4 Chapter References

1. Geerlink P., Videler J. The Relation Between Structure and Bending Properties of the Teleost Fin Rays. Netherlands Journal of Zoology. 1987; 37: 59-80.

2. Gibb, A. C., Jayne, B. C., Lauder, G. V. Kinematics of Pectoral Fin Locomotion in the Bluegill Sunfish Lepomis Macrochirus. Journal of Experimental Biology. 1994; 189: 133-161.

3. Lauder G. V., Drucker E. G., "Morphology and Exerimental Hydrodynamics of Fish Fin Control Surfaces", IEEE Journal of Oceanic Engineering. 2004; 29: 556-571.

4. McCutchen C. The Trout Tail Fin: a Self-Cambering Hydrofoil. Journal of Biomechanics. 1970; 3: 271-281.

5. Videler J. On the Interrelationships Between Morphology and Movement in the Tail of the Cichlid Fish Tilapia Nilotica. Nertherland Journal of Zoology. 1975; 25: 144-194.

6.0 Conclusion

The three main foci of this research initiative involved: 1) seeking improvements in actuation performance of the artificial muscle actuators that would be incorporated into the artificial pectoral fin, 2) developing the manufacturing techniques that would enable a more integrated fabrication approach to this design, and 3) the construction of a mechanical model which would provide a test-bed for verification of the kinematics of the biomimetic device.

6.1 Actuator Performance

The greatest increase in performance was seen in the films grown on different deposition materials. The film grown on a nickel tube yielded the highest average strains and outperformed the next best actuators by 126 to 300% over the tubular films synthesized on other materials and 28% over the next best flat film which was grown on platinum foil. However, the film grown on a flat foil of nickel produced mediocre results and was outperformed by the tubular film synthesized on nickel by 124%. The same lack of correlation between actuation performance and material was echoed in the dynamic tests performed on glassy carbon and platinum grown films as well. However, upon inspection of the morphologies of the films a strong similarity between the two top performing actuators became apparent. The tubular film grown on nickel and the flat film grown on platinum both possessed the finest pores at the highest density of dispersion over the electrode surface of the film. In fact the film grown on the nickel rod had the greatest number and smallest pores, which further suggests this correlation between performance and porosity. All films, both flat foils and rods, were treated with the same polishing and cleaning technique making it unclear what the major source of the different film characteristics was. Further experimentation with surface effects of the deposition electrode materials and their effect on films is necessary in order to locate the source of these effects in the film morphologies.

Experiments involving embedding materials either as electrodes along the length of the film or at the electrode sight produced both positive and negative results. The two most successful results from incorporating materials into the polymers during synthesis were the samples with the gold wires wound helically in a tube of polypyrrole and the gold wire embedded at the working electrode sight in a flat film. Unfortunately, these actuators were prone to earlier mechanical failure than their plain film counterparts. These actuators were more likely to be useful in high speed low stress applications.

6.2 Cofabrication

Several molding and casting techniques were explored within the scope of this work. The results of which led to the successful development of a pectoral fin cast from elastomer materials with only six parts: four fin rays, a web, and a base. The fin was constructed such that joints and fixtures were attained by varying material properties and geometry. Means of incorporating the conducting polymers into the fin while maintaining the manufacturing design approach, which avoids assembly, were also developed. Two basic strategies were implemented. The first involved attempts to synthesize the conducting polymers onto an elastomer structure of the fin; which was achieved by performing chemical oxidation phases onto the elastomer substrates followed by electrochemical synthesis. The second involved casting pre-synthesized conducting polymer films onto the elastomers. The casting technique was a far more successful method of integrating the polymer with the elastomer structure in terms of retaining active properties of the artificial muscle. However, in terms of reducing manufacturing cost there are potentially significant benefits to using the chemical oxidation techniques.

The results of the fabrication techniques indicated that a first generation cast fin is possible. There was solid adhesion between the conducting polymers and the elastomers and initial tests of the actuation performance of the combined materials showed an increase in strain output by as much as 1.33 to 10×. This increase was likely due to resonance but needs to be fully characterized in order to gain a legitimate correlation between performance and casting the materials together.

Figure 6-1 shows a conceptual model which represents ideas of the next phase of future work possible based on the casting the polymers onto an elastomer fin structure. The black sheathes represent strips of the polymer that have been cast onto the amber colored urethane fin. Because the urethane is stable in the electrolyte solution in which the polymers are actuated, this model could be submersed and operated directly.
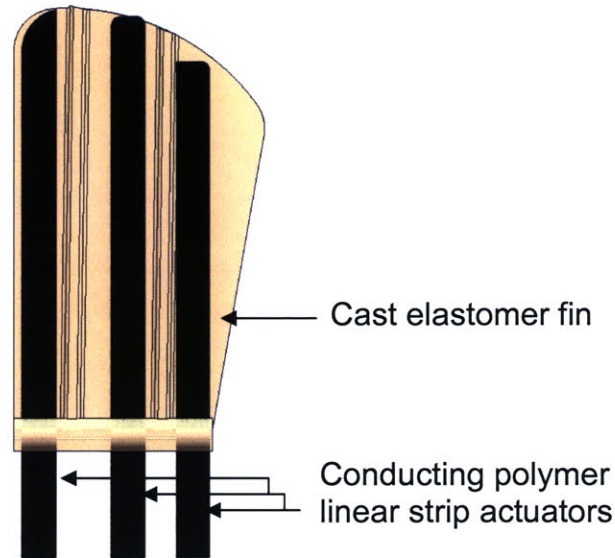
Figure 6-1. A conceptual design for a first generation active co-fabricated design; no part assembly is required as polymers would be cast directly into the fin.

6.3 Mechanical Model

A compliant mechanism based model of the pectoral fin of a fish was developed and actuated to perform a few basic swimming maneuvers. The current design of the fin produced life-like motion as confirmed by the biology team at Harvard. However, several notable flaws still exist at the mechanical level. In the snapshots of the fin executing swimming motions in a flow tank revealed limitations in the range of motion attainable. The full range needed to fulfill the kinematic requirements as indicated in the data accumulated from the biological findings are on the order of 120 degree sweep while the mechanical model was outputting 90 degrees on average. One simple way to improve this was to change the clamp which held the fin. A new design and configuration are shown in Figure 6-2 as future work which is continuing to be developed. In this next

model the clamp is designed to connect the fin to the motor array by compressing it through the keyed feature on the base of the fin. This constrains twisting or shifting of the fin without impeding cupping and spreading while allowing a greater range of motion in the sweep actuation mode.
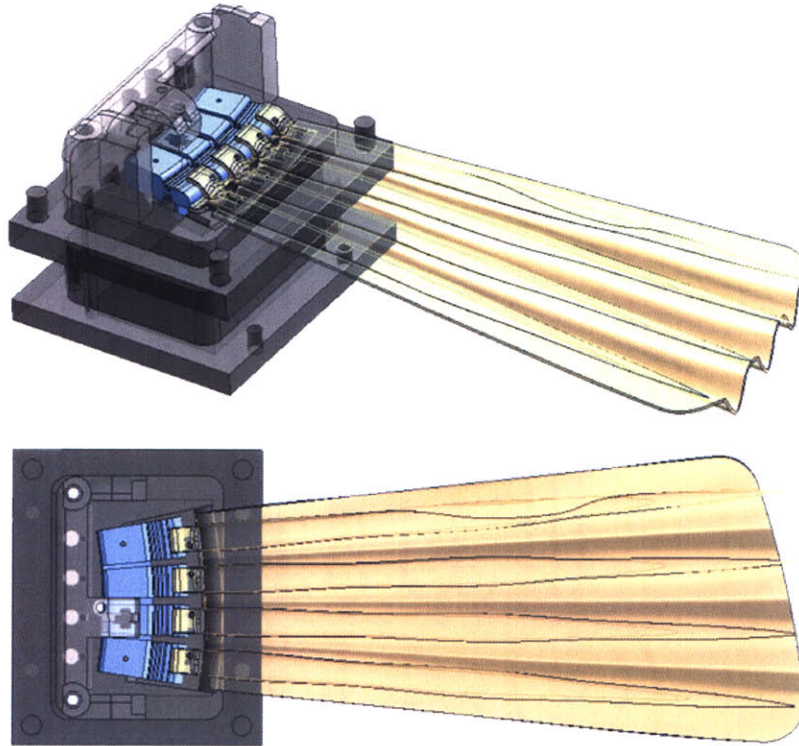
Figure 6-2. The clamp is designed to hold the fin in a horizontal plane compressing the base through the keyed feature on the base without constraining the cupping and spreading motions.

Figure 6-3 shows the fin with the new base as it will be implemented in the tank. Another important addition to this design is the inclusion of a plate that simulates the body of the fish. This will enhance the accuracy of the hydrodynamics of the mechanical fin model.
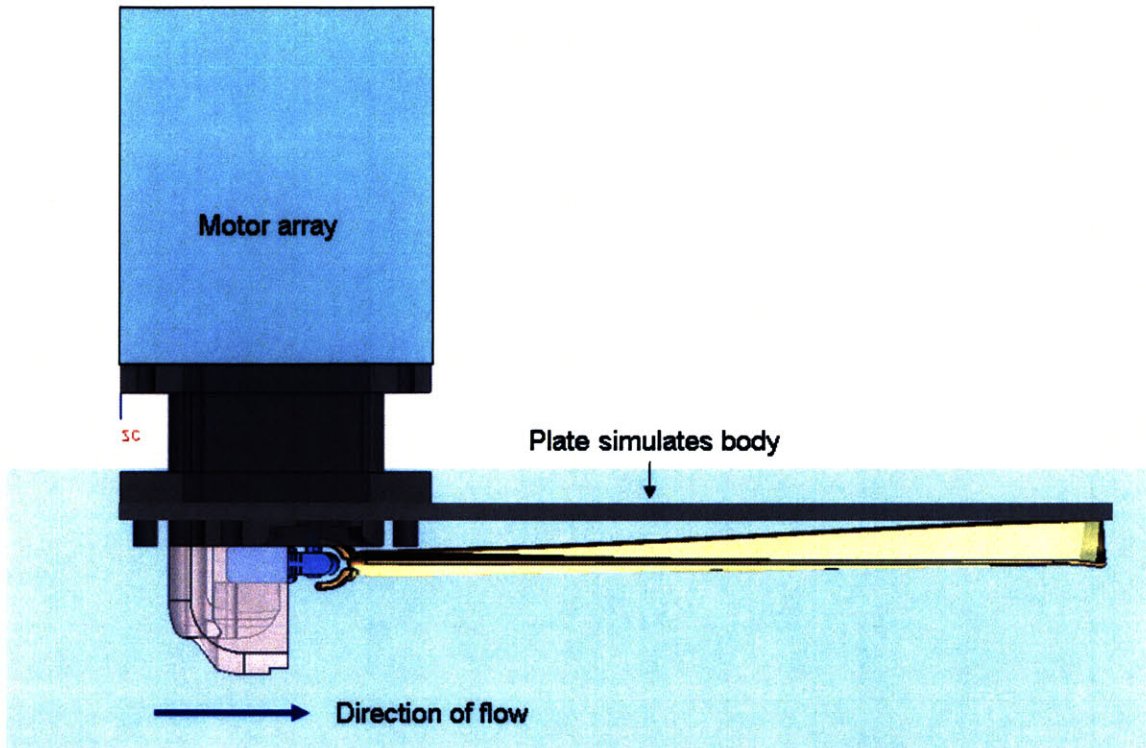
Figure 6-3. The clamp holds the fin in the flow tank with the addition of a plate that provides more realistic hydrodynamic conditions.

The overall goal is to iteratively re-incorporate the higher level functions of the fin. This is done in phases in order to avoid overcomplicating the design. The top priorities for future work with this model include the following adjustments:

- sensing ability for closed-loop control of the fin,
- force measurements on the tendons during swimming,
- the incorporation of conducting polymers as actuators,
- increased control over fin orientation,
- decoupling of spread actuation,
- greater leading edge control,
- bifurcation of fin rays.

While the fin is demonstrating a certain ability to swim; greater control over the surface area, attitude, and stiffness will continue to enhance the fin's performance. Of course, the ability to sense the forces on the fin allow closed-loop control for swimming purposes, sensing the forces on the tendons will aid in the process of integrating the conducting polymer actuators into future generation designs. The ultimate goal of this project is to

134

integrate the artificial muscle actuators which, although it will be challenging to do, will enable the production of a truly biomimetic fin.

Appendix A: Material Data Sheets

ACCURA®
SI 40 MATERIAL

for the SLA® Viper™, 3500, 5000 & 7000 systems

Accura SI 40 material is the first SL material to combine high temperature resistance with toughness.

High temperature applications without the brittleness.

Accura® SI 40 material is the first stereolithography (SL) material to mimic *Nylon 6:6,* allowing parts to be used in true under-the-hood applications, and those requiring elevated temperatures without the limitation of brittleness and breakage.
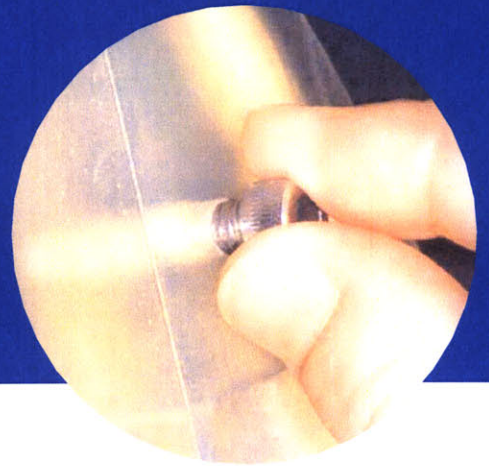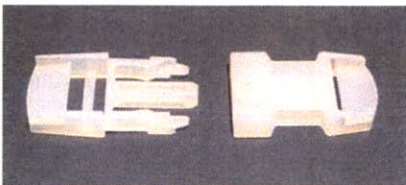
Excellent mechanical properties.

Offering an attractive mix of thermal resistance, stiffness, and elongation at break, Accura SI 40 material is an excellent choice for a large number of applications.

Outstanding part quality.

With optical clarity, smooth side walls, a near-mirror top surface, tack-free downface, parts built with the SI 40 material require minimal finishing. A thin cured line-width produces excellent feature resolution.
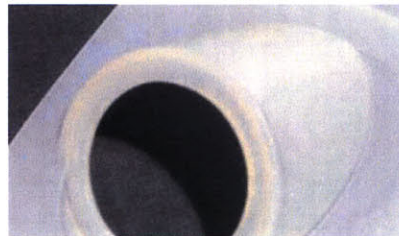
Long vat life.

The Accura SI 40 material maintains good recoating characteristics and low viscosity without the need to make adustments in the field by adding additional viscosity stabilizers, resulting in consistent, trouble-free part building.

High part yield.

The Accura SI 40 material builds green strength quickly with good layer-to-layer adhesion for excellent "first time" part building success. The Accura SI 40 material is also build chamber environment independent.

Accurate, mechanically stable parts.

The Accura SI 40 material is an accurate material with relatively low linear or differential shrinkage. Parts maintain their rigidity even when subjected to elevated humidity.

Build process you can depend on.

3D Systems' team of highly trained process engineers invests significant time to develop and optimize the build parameters with an emphasis on reliability, accuracy, part quality and throughput for each Accura SL material. This results in improved customer yields, reduced labor time and a better finished product.

Applications:

- High temperature applications
  - Under hood bolt-on testing
  - Wind tunnel testing
  - HVAC testing
- Prototyping and testing of rigid cases and enclosures
- Flow visualization
- Drilling and self-tapping
- Pressure tappings
- Snap fit assemblies
- RTV mold patterns

Accura SI 40 Material
for the SLA Viper, 3500, 5000 and 7000 systems

Typical Properties

Liquid Material

MEASUREMENT	CONDITION	SOLID STATE Nd:YVO$_4$
Appearance		Clear amber
Density	@ 25°C (77°F)	1.1 g/cm^3
Viscosity	@ 30°C (86°F)	485 cps
Penetration depth (Dp) [1]		6.6 mils *, 6.8 mils **
Critical exposure (Ec) [1]		21.7 mJ/cm^2 *, 20.1 mJ/cm^2 **
Tested build styles		EXACT™
		EXACT HR*
		FAST™
		ThinLayer™

[1] Dp and Ec values are not reliable indicators on throughput as throughput is affected by overhead time, layer thickness and part geometry.

* for the Viper SLA system

** for the SLA 7000 system

Post-Cured Material [2]

MEASUREMENT	CONDITION	90-MINUTE UV	90-MINUTE UV + THERMAL	90-MINUTE UV	90-MINUTE UV + THERMAL
		VIPER SLA SYSTEM		SLA 7000 SYSTEM	
Tensile Strength	ASTM D 638	57.2 - 58.7 MPa (8270 - 8490 PSI)	73.9 - 74.2 MPa (10690 - 10720 PSI)	61.5 - 61.7 MPa (8890 - 8920 PSI)	69.6 - 73.8 MPa (10050 - 10660 PSI)
Elongation at Break	ASTM D 638	4.8 - 5.1 %	4.8 - 5.1 %	4.9 - 5.1 %	4.7 - 6.4 %
Tensile Modulus	ASTM D 638	2628 - 3321 MPa (380 - 480 KSI)	2906 - 3321 MPa (420 - 480 KSI)	2840 - 3048 MPa (410 - 440 KSI)	2909 - 3186 MPa (420 - 460 KSI)
Flexural Strength	ASTM D 790	93.4 - 96.1 MPa (13500 - 13900 PSI)	116.2 - 118.3 MPa (16800 - 17100 PSI)	92.8 - 97 MPa (13400 - 14000 PSI)	106.7 - 110.1 MPa (15400 - 15900 PSI)
Flexural Modulus	ASTM D 790	2836 - 3044 MPa (410 - 440 KSI)	3113 - 3182 MPa (450 - 460 KSI)	2618 - 2756 MPa (380 - 400 KSI)	2840 - 2909 MPa (410 - 420 KSI)
Impact Strength Notched Izod	ASTM D 256	22.5 - 27.2 J/m (0.43 - 0.52 ft - lbs/in)	22.5 - 30.9 J/m (0.43 - 0.59 ft - lbs/in)	22.3 - 29.9 J/m (0.42 - 0.56 ft - lbs/in)	22.3 - 29.9 J/m (0.42 - 0.56 ft - lbs/in)
Heat Deflection Temperature	ASTM D 648 @ 66 PSI @ 264 PSI	51°C (123.8°F) 43°C (109.4°F)	101°C (213.8°F) 82°C (179.6°F)	54°C (129.2°F) 49°C (120.2°F)	114°C (237.2°F) 89°C (192.2°F)
Glass Transition, Tg	DMA, E"	65.6°C (150.1°F)	74.9°C (166.8°F)	62°C (143.6°F)	72°C (161.6°F)
Coefficient of Thermal Expansion	ASTM E 831-93 TMA (T<Tg) TMA (T>Tg)	99.6 x 10^{-6} m/m °C 185 x 10^{-6} m/m °C	60.8 x 10^{-6} m/m °C 167 x 10^{-6} m/m °C	73.5 x 10^{-6} m/m °C 188 x 10^{-6} m/m °C	67.1 x 10^{-6} m/m °C 189 x 10^{-6} m/m °C
Hardness, Shore D	ASTM D 2240	82	84	86	86

[2] Mechanical properties reported are determined after conditioning of the parts at 50%RH and 23°C for a period greater than 72 hours as specified by ASTM standards. Mechanical properties of parts without this conditioning may be different from values reported.

Softening Evergreen 10 Using *Everflex*^{tm} Flexibilizer

SMOOTH-ON SINCE 1895

Everflex^{tm} **Flexibilizer** is a softening agent that lowers the cured durometer of Smooth-On's **Evergreen 10**. The charts below indicates the effect of the flexibilizer has on cured Evergreen 10 after 24 hours when added as a percentage of the total mix.

Using Flexibilizer By Weight ... For best results, you should use an accurate scale to properly use Everflex™ with Evergreen 10. Everflex™ should be weighed and must be thoroughly mixed (at least one minute) with the appropriate amount of Part B before combining with Part A.

Softening Evergreen 10 with Everflex™

Normally, Evergreen 10 cures to an ultimate hardness of Shore A 10. Evergreen 10 can be made softer and more flexible by adding different percentages of Everflex™.

Part B	+	Parts By Weight Everflex™ (mix thoroughly)	+	Part A	=	Shore A* Hardness	Shore 00* Hardness
100		0		100	=	10	72
100		25		100	=	8	63
100		50		100	=	3	56
100		100		100	=	-	37
100		200		100	=	-	22

*Shore harness obtained after 24 hours

Using **Everflex™** by volume with Evergreen 10. . . **if you want to add Everflex™ by volume instead of by weight, you can do so by measuring out equal amounts of parts A, B and Everflex**^{tm}. **As indicated above, this will result in a cured Shore 00 hardness of 37. Or measure out 2 parts of Everflex**^{tm} **to 1 part each of A and B to achieve a Shore 00 hardness of 22.**

Toll-free technical help hotline: (800) 762-0744   Fax: (610) 252-6200

Or Visit Our Website: www.smooth-on.com

SMOOTH-ON
SINCE 1895

PMC™ 121 Series
Polyurethane Rubber Compounds

PRODUCT OVERVIEW

The PMC-121 Series urethane rubbers feature convenient one-to-one by volume mix ratios. **PMC-121/20** cures with negligible shrinkage to a very soft and pliable rubber, and is especially suited for making molds with deep undercuts and pronounced detail. **PMC-121/30 Dry and PMC-121/30 Wet** are exceptionally strong and abrasion resistant for soft urethane mold rubbers. Pick the one best suited for your application. The *dry* version does not exude an oil and can be used for casting waxes, Smooth-On liquid plastics, gypsum plasters and other materials. The *wet* version contains a built-in release agent to aid in demolding hard plasters and concrete. **PMC-121/40 Dry and PMC-121/40 Wet** are made with a new chemical system that gives improved performance, has lower viscosity and is beige in color. **PMC-121/50** is a "wet-only" mold rubber that is long lasting and durable when used in a variety of applications including reproduction of ornamental plaster, precast concrete and ceramic case molds.

PMC™ 121 Series mold rubbers are easy to mix and pour and are exceptionally strong. They are suited for a variety of applications including making molds to reproduce sculpture and architectural elements, as well as for making special effects, toys and prototypes. These rubbers will meet the stringent demands of production casting of wax, plasters, concrete, resins and epoxies. Vibrant colors can be achieved by adding So-Strong™ Color Tints, available from Smooth-On.

TECHNICAL OVERVIEW

	Shore A	Mix Ratio	Color	Spec. Vol.	Spec. Grav.	Mixed Viscosity	Tear (C) (pli)	Elong. At Break	Tensile Strength	Compr. Set
PMC-121/20	20	1:1 pbv	Cl. Amber	27.7	1.0 g/cc	1,000 cps	20 pli	>1,000%	>200 psi	33%
PMC-121/30*	30	1:1 pbv	Cl. Amber	27.7	1.04 g/cc	1,800 cps	82 pli	>1,000%	>400 psi	26%
PMC-121/40*	40	1:1 pbv	Beige	27.2	1.02 g/cc	1,500 cps	65 pli	>1,000%	450 psi	17%
PMC-121/50	50	1:1 pbv	Cl. Amber	26.7	1.04 g/cc	1,400 cps	85 pli	500%	350 psi	26%

~ **Pot Life:** 30 Minutes   ~ **Cure Time/Demold:** Overnight/16 hours   **Shrinkage:** Negligible

* Available "Dry," or "Wet," which exudes an oil for improved release to aid in demolding hard plasters and concrete.

Start By Preparing Your Model -

Preparation . . . Good ventilation (room size) is necessary. Room temperature should be at 72°F/23°C. Humidity should be low. Wear long sleeve garments and rubber gloves to minimize skin contact.

Some Materials Must Be Sealed . . . To prevent adhesion between the rubber and model surface, models made of porous materials (gypsum plasters, concrete, wood, stone, etc.) must be sealed prior to applying a release agent. SuperSeal (available from Smooth-On) is a fast drying sealer suitable for sealing porous surfaces without interfering with surface detail. Shellac is suitable for rough contours. Modeling clays that contain sulfur or water must be sealed with SuperSeal or shellac. Thermoplastics (polystyrene) must also be sealed with shellac or PVA. *In all cases*, the sealing agent should be applied and allowed to completely dry prior to applying a release agent.

Non-Porous Surfaces – metal, glass, hard plastics, sulfur free clays, etc. require only a release agent.

Applying A Release Agent . . . A release agent is necessary to facilitate demolding when casting into or over most surfaces. Use a release agent made specifically for mold making (Universal Mold Release available from Smooth-On). A liberal coat of release agent should be applied onto all surfaces that will contact the rubber. ~IMPORTANT: To ensure thorough coverage, lightly brush the release agent with a soft brush over all surfaces of the model. Follow with a light mist coating and let the release agent dry for 30 minutes. **If there is any question** about the effectiveness of a sealer/release agent combination, a small scale test should be made on an identical surface for trial.

Measuring & Mixing . . .

Liquid urethanes are **moisture sensitive** and will absorb atmospheric moisture. Mixing tools and containers should be clean and made of metal, glass or plastic. Materials should be stored and used in a warm environment (72° F / 23° C). **IMPORTANT:** Shelf life of product is drastically reduced after opening. Remaining product should be used as soon as possible. Immediately replacing the lids on both containers after dispensing product will prolong the shelf life of the unused product. **XTEND-IT Dry Gas Blanket** (available from Smooth-On) will significantly prolong the shelf life of unused liquid urethane products.

Important: Pre-Mix the Part B before using. After dispensing equal amounts of Parts A and B into mixing container, mix thoroughly for at least 3 minutes making sure that you scrape the sides and bottom of the mixing container several times.
If Mixing Large Quantities (16 lbs./7 kgs. or more) at one time, use a mechanical mixer (i.e. Squirrel Mixer or equal) for 3 minutes followed by careful hand mixing for one minute as directed above. Then, pour entire quantity into a new, clean mixing container and do it all over again.
Although this product is formulated to minimize air bubbles in your the cured rubber, vacuum degassing will further reduce entrapped air. A pressure casting technique using a pressure chamber can yield totally bubble free castings. Contact Smooth-On or your distributor for further information about vacuum degassing or pressure casting.

Pouring   *Curing*   *Performance*

For best results, pour your mixture in a single spot at the lowest point of the containment field. Let the rubber seek its level up and over the model. **A uniform flow will help minimize entrapped air.** The liquid rubber should level off at least 1/2" (1.3 cm) over the highest point of the model surface.

Curing . . . Allow rubber to cure overnight (at least 16 hours) at room temperature (77 F/25 C) before demolding. Cure time can be reduced with mild heat or by adding Smooth-On "Kick-It" Cure Accelerator. Do not cure rubber where temperature is less than 65 F /18 C.

Post Curing – After rubber has cured at room temperature, heating the rubber to 150° F (65° C) for 4 to 8 hours will increase physical properties and performance.

Using The Mold . . . If using as a mold material, a release agent should be applied to the mold before each casting. The type of release agent to use depends on the material being cast. The proper release agent for **wax, liquid rubber or thermosetting materials** (i.e. Smooth-On liquid plastics) is a spray release made specifically for mold making (available from Smooth-On or your distributor). Polyester (Fiberglass & Resin) requires use of a mold conditioner/release combination to protect the mold. Permalease SMC and Permalease 650 (from Smooth-On) are suitable for this application. Prior to casting **gypsum plaster materials**, sponge the mold with a soap solution for better plaster flow and easy release. **In & Out Water Based Release Concentrate** (available from Smooth-On) is recommended for releasing abrasive materials like **concrete.**

Performance & Storage - Fully cured rubber is tough, durable and will perform if properly used and stored. The physical life of the rubber depends on how you use it. Contact Smooth-On directly with questions about this material relative to your application.

Safety First!   *Safety First!*   *Safety First!*   *Safety First!*

The Material Safety Data Sheet (MSDS) for this or any Smooth-On product should be read prior to use and is available upon request from Smooth-On. All Smooth-On products are safe to use if directions are read and followed carefully.
Be careful. Part A is a TDI prepolymer. Vapors, which can be significant if material is heated or sprayed, cause lung damage and sensitization. Use only with adequate ventilation. Contact with skin and eyes may cause severe irritation. Flush eyes with water for 15 minutes and seek immediate medical attention. Remove from skin with waterless hand cleaner followed by soap and water   Prepolymers contain trace amounts of TDI which, if ingested, must be considered a potential carcinogen. Refer to MSDS .

Part B) is irritating to the eyes and skin. If contaminated, flush eyes with water for 15 minutes and seek immediate medical attention. Remove from skin with soap and water. When mixing with Part A follow precautions for handling isocyanates. **Important:** The information contained in this bulletin is considered accurate. However, no warranty is expressed or implied regarding the accuracy of the data, the results to be obtained from the use thereof, or that any such use will not infringe upon a patent. User shall determine the suitability of the product for the intended application and assume all risk and liability whatsoever in connection therewith.

For Technical Help: Tel. (800) 762-0744   Fax. (610) 252-6200 Website: www.smooth-on.com   01/02

Platinum Series
Addition Cure Silicone Rubber Compounds

SMOOTH-ON
SINCE 1895

PRODUCT OVERVIEW

Smooth-On Platinum Silicones *(platinum curative)* cure at room temperature with no shrinkage. With different hardness's products to choose from, they offer tremendous versatility and are suitable for making production molds of any configuration, large or small. These silicones exhibit good chemical, abrasion and heat resistance. Materials such as plasters, concrete, wax, low-melt metal alloys or resins (urethane, epoxy or polyester) can then be cast into these silicone rubbers without a release agent.

Smooth-Sil[tm] Platinum Silicones are used for rapid prototyping, wax casting (foundries and candle makers), architectural restoration and for casting concrete.

Dragon Skin[tm] is a 1A:1B by volume mix rubber that has tremendous elongation and will rebound to its original shape (good for repetitive motion applications). In addition to being a good mold making material, Dragon Skin is used to create creatures for movie effects (a separate technical bulletin is available for Dragon Skin[tm] from Smooth-On).

SORTA-Clear[tm] 40 is a premium water white translucent silicone rubber that is designed for extracting models via cutting (a separate technical bulletin is available for SORTA Clear[tm] from Smooth-On).

Accessories: A silicone "thinner" is available to lower the mixed viscosity of these products. THI-VEX[tm] thickener can be added to Smooth-Sil[tm] 920, 930, 940 & 950 thicken these silicones for brush-on applications.

TECHNICAL OVERVIEW

	Shore A	Mix Ratio Wt. or Vol.	Color	Pot Life	Demold Time	Specific Volume	Specific Gravity	Mixed Viscosity	Die B Tear Strength	Tensile Strength	Shrinkage
Dragon Skin™	10	1:1 pbw, pbv	Translucent	20 Min.	5 Hours	25.8	1.07	23,000 cps	102 pli	475 psi	Negligible
Dragon Skin Q™	10	1:1 pbw, pbv	Translucent	8 Min.	75 Min.	25.8	1.07	23,000 cps	102 pli	475 psi	Negligible
Smooth-Sil™ 910	10	100:10 pbw	Off-White	30 Min.	6 Hours	25.4	1.09	7,000 cps	40 pli	200 psi	Negligible
Smooth-Sil™ 920	20	1:1 pbw, pbv	Translucent	25 Min.	4 Hours	25.6	1.08	20,000 cps	120 pli	550 psi	Negligible
Smooth-Sil™ 930	30	100:10 pbw	Blue	45 Min.	24 Hours	24.0	1.15	40,000 cps	110 pli	575 psi	Negligible
Smooth-Sil™ 940	40	100:10 pbw	Pink	30 Min.	24 Hours	23.4	1.18	35,000 cps	100 pli	600 psi	Negligible
Smooth-Sil™ 950	50	100:10 pbw	Blue	45 Min.	24 Hours	22.3	1.24	35,000 cps	155 pli	725 psi	Negligible
SORTA Clear™ 40	40	100:10 pbw	Translucent	60 Min.	16 Hours	25.8	1.07	35,000 cps	120 pli	800 psi	Negligible

Preparation

Cure Inhibition – Store and use silicones at room temperature (72°F / 23°C). Addition cured silicone rubber may be inhibited by certain contaminants in or on the pattern to be molded (such as sulfur based clays, polyesters, certain wood surfaces) resulting in tackiness at the pattern interface or a total lack of cure throughout the mold. If compatibility between the rubber and the surface is a concern, a small scale test is recommended. Apply a small amount of rubber onto a non-critical area of the pattern. Inhibition has occurred if the rubber is gummy or uncured after the recommended cure time has passed.

Silicones will stick to some porous surfaces. Smooth-On's *SuperSeal*[tm] is an unobtrusive, low viscosity soap/wax blend that will not harm a model's surface and can be washed off with warm water. To prevent inhibition against sulfur-based clays, a "barrier coat" of clear acrylic spray to the model surface is usually effective. Allow to thoroughly dry.

Applying A Release Agent? Although not usually necessary, a release agent will make demolding easier when casting into or over most surfaces. Ease Release 200[tm] is a proven release agent for making molds with silicone rubber. Mann Ease Release[tm] products are available from Smooth-On or your Smooth-On distributor. **~IMPORTANT**: To ensure thorough coverage, lightly brush the release agent with a soft brush over all surfaces of the model. Follow with a light mist coating and let the release agent dry for 30 minutes.

If there is any question about the effectiveness of a sealer/release agent combination, a small-scale test should be made on an identical surface for trial. Also, you can **call Smooth-On for technical assistance at (800) 762-0744.**

Measuring & Mixing

Materials should be stored and used in a warm environment (72° F / 23° C). Store material where temperature does not exceed 75°F / 23°C. If using a material that is mixed by weight, you must use an accurate scale (gram scale) to weigh Parts A and B. Before you begin, pre-mix Part B (base) thoroughly. After dispensing required amounts of Parts A and B into mixing container, **mix thoroughly for 3 minutes** making sure that you **scrape the sides and bottom of the mixing container several times**. After mixing parts A and B, vacuum degassing is recommended to eliminate any entrapped air. Vacuum material for 2 -3 minutes (29 inches of mercury), making sure that you leave enough room in container for product volume expansion.

Pouring	*Curing*	*Mold Performance*

For best results, pour your mixture in a single spot at the lowest point of the containment field. Let the rubber seek its level up and over the model. **A uniform flow will help minimize entrapped air.** The liquid rubber should level off at least 1/2" (1.3 cm) over the highest point of the model surface.

Curing . . . Allow the mold to cure overnight (at least 16 hours) at room temperature (77°F/25°C) before demolding. Do not cure rubber where temperature is less than 65°F /18°C.

Post curing the mold will aid in quickly attaining maximum physical and performance properties. After curing at room temperature, expose the rubber to 80° C for 2 hours and 100° C for 2 hours. Allow mold to cool to room temperature before using. **Note:** Post curing SORTA Clear 40 will cause rubber to yellow.

Using The Mold . . . When first cast, silicone rubber molds exhibit natural release characteristics. Depending on what is being cast into the mold, mold lubricity may be depleted over time and parts will begin to stick. No release agent is necessary when casting wax or gypsum. Applying a release agent such as Universal Mold Release or Ease Release 200 (available from Smooth-On) prior to casting polyurethane, polyester and epoxy resins is recommended to prevent mold degradation. Contact Smooth-On for information on a powder coating technique that will yield a dry matte finish to cured castings.

Mold Performance & Storage. . . The physical life of the mold depends on how you use it (materials cast, frequency, etc.). Casting abrasive materials such as concrete can erode mold detail, while casting non-abrasive materials (wax) will not affect mold detail. Before storing, the mold should be cleaned with a soap solution and wiped fully dry. Two part (or more) molds should be assembled. Molds should be stored on a level surface in a cool, dry environment.

Thickening With Thi-Vex[tm] *Thickening Agent* . . . Adding 0.5% - 1% Thi-vex[tm] (% of the total weight of the mixture, A+B) will make rubber brushable for vertical surface application. Due to low viscosity, Thi-Vex[tm] will not work with SS910.

Safety First

Be careful. Use in a properly ventilated area ("room size" ventilation). Wear vinyl gloves only. Latex gloves will inhibit the cure of the rubber. Contact with skin and eyes may cause irritation. Flush eyes with soap and water for 15 minutes and seek immediate medical attention. Remove from skin with waterless hand cleaner followed by soap and water.

Important: The information contained in this bulletin is considered accurate. However, no warranty is expressed or implied regarding the accuracy of the data, the results to be obtained from the use thereof, or that any such use will not infringe upon a patent. User shall determine the suitability of the product for the intended application and assume all risk and liability whatsoever in connection therewith.

**Smooth-On offers a complete line of Liquid Rubber, Liquid Plastic and
Release Agent products for hundreds of industrial and art related applications.
Chances are there is a distributor in your area to offer local support.**

EVERGREEN™ Series

SMOOTH-ON

Isocyanate Free Liquid Urethane Rubbers

PRODUCT OVERVIEW

The EVERGREEN™ Series of liquid urethane rubbers represents a new direction in urethane rubber technology. These urethanes are isocyanate free and contain no free TDI, MDI, MOCA or MERCURY *(contains no suspected carcinogens)*. Each has a very low viscosity (no vacuuming necessary) for minimal bubble entrapment. They also feature a convenient one-to-one by volume mix ratios (except the 60A, which is 2A:1B by volume) and cure with negligible shrinkage. **Compared to other urethanes, this rubber exhibits superior release characteristics when casting polyester, urethane and other types of resins.**
Shore Hardness Range: 10A, 20A, 30A, 40A, 50A & 60A .
Soft ———————————→ Medium

Do Not Cast Wax – Evergreen rubbers will leave the surface of wax castings tacky.
The EVERGREEN™ Urethanes are suitable for a variety of applications and can be used to cast urethane, polyester or epoxy resins, gypsum plasters and concrete. Also good for industrial parts, special effects, etc.

TECHNICAL OVERVIEW

	Shore A	Mix Ratio By Volume	Color	Spec. Vol.	Spec. Grav.	Viscosity	Tear(pli)	Elong/Break	Tensile	Compr. Set
Evergreen 10	10	1A:1B	Off-White	27.4	1.01	600 cps	>25 pli	>1,000 %	200 psi	15.40%
Evergreen 20	20	1A:1B	Blue	27.1	1.024	1,000 cps	>30 pli	>650 %	250 psi	10.80%
Evergreen 30	30	1A:1B	Op. Yellow	27.1	1.024	800 cps	>50 pli	>600%	450 psi	13.60%
Evergreen 40	40	1A:1B	Red	26.7	1.036	1,000 cps	>70 pli	>500%	500 psi	18%
Evergreen 50	50	1A:1B	Off-White	26.9	1.03	1,400 cps	>100 pli	>450%	500 psi	23.80%
Evergreen 60	60	2A:1B	Tr. Yellow	26.5	1.046	2,000 cps	>100 pli	>500%	650 psi	35.40%

~Pot Life: 30 Minutes   **~Cure Time/Demold:** 16 Hours   **Shrinkage:** Negligible

Start By Preparing Your Model -

Some Materials Must Be Sealed . . . To prevent adhesion between the rubber and model surface, models made of porous materials (gypsum plasters, concrete, wood, stone, etc.) must be sealed prior to applying a release agent. **SuperSeal™**(available from Smooth-On) will have minimal effect on surface detail and texture. **Modeling clays** that contain sulfur (Roma Plastalina) or moisture must also be sealed. **SuperSeal™**, spray shellac or PVA are suitable sealing agents. Sulfur-free and non-water based clays require release agent only. *In all cases*, the sealing agent should be applied and allowed to completely dry prior to applying a release agent.

Applying A Release Agent . . . Although Evergreen exhibits good release properties, a release agent is recommended to facilitate demolding when casting into or over most surfaces. Use a release agent made specifically for mold making (**Universal Mold Release™** or **Ease Release 200™** available from Smooth-On or your Smooth-On distributor). A liberal coat of release agent should be applied onto all surfaces that will contact the rubber. **~IMPORTANT:** To ensure thorough coverage, lightly brush the release agent with a soft brush over all surfaces of the model. Follow with a light mist coating and let the release agent dry for 30 minutes. **If there is any question** about the effectiveness of a sealer/release agent combination, a small-scale test should be made on an identical surface for trial.

Measuring & Mixing . . .

Liquid urethanes are **moisture sensitive** and will absorb atmospheric moisture. Mixing tools and containers should be clean and made of metal, glass or plastic. Materials should be stored and used in a warm environment (72° F / 23° C). **IMPORTANT:** Shelf life of product is drastically reduced after opening. Remaining product should be used as soon as possible. Immediately replacing the lids on both containers after dispensing product will prolong the shelf life of the unused product. **XTEND-IT Dry Gas Blanket** (available from Smooth-On) will significantly prolong the shelf life of unused liquid urethane products.

Important: Pre-Mix the Part B before using. After dispensing equal amounts of Parts A and B into mixing container, mix thoroughly for at least 3 minutes making sure that you scrape the sides and bottom of the mixing container several times. **If Mixing Large Quantities** (16 lbs./7 kgs. or more) at one time, use a mechanical mixer (i.e. Squirrel Mixer or equal) for 3 minutes followed by careful hand mixing for one minute as directed above. Then, pour entire quantity into a new, clean mixing container and do it all over again.

Although this product is formulated to minimize air bubbles in your cured mold, vacuum degassing will further reduce entrapped air. A pressure casting technique using a pressure chamber can yield totally bubble free castings. Contact Smooth-On or your distributor for further information about vacuum degassing or pressure casting.

Pouring   Curing   Mold Performance

For best results, pour your mixture in a single spot at the lowest point of the containment field. Let the rubber seek its level up and over the model. **A uniform flow will help minimize entrapped air.** The liquid rubber should level off at least 1/2" (1.3 cm) over the highest point of the model surface.

Curing . . . Allow the mold to cure overnight (at least 16 hours) at room temperature (77°F/25°C) before demolding. Do not cure rubber where temperature is less than 65°F /18°C. Post curing the rubber in an oven at 150°F / 65°C for 4 - 6 hours will improve physical properties of the rubber.

Using The Mold . . . If using as a mold material, a release agent should be applied to the mold before each casting. The type of release agent to use depends on the material being cast. The proper release agent for **liquid rubber, urethane resins** (i.e. Smooth-On liquid plastics), **polyester or epoxy resin** is Universal Mold Release™ (available from Smooth-On or your distributor). Prior to casting **gypsum plaster materials**, sponge the mold with a soap solution for better plaster flow and easy release. **In & Out Water Based Release Concentrate** (available from Smooth-On) is recommended for releasing abrasive materials like **concrete.**

Mold Performance & Storage - The physical life of the mold depends on how you use it (materials cast, frequency, etc.). Casting abrasive materials such as concrete will eventually erode mold detail, while casting non-abrasive materials (wax) will not affect mold detail. Before storing, the mold should be cleaned with a soap solution and wiped fully dry. Two part (or more) molds should be assembled. Molds should be stored on a level surface in a cool, dry environment. Do not stack molds, expose them to moisture or UV light.

For Technical Help: Tel. (800) 762-0744   Tel. (610) 252-5800   Fax. (610) 252-6200
Visit Us On The Web: <u>www.smooth-on.com</u>   01/02